On the Role of Antennas in the Achievable Resolution and Accuracy from Near-Field Microwave Tomography

by

Nozhan Bayat

A Thesis submitted to the Faculty of Graduate Studies of
The University of Manitoba
in partial fulfilment of the requirements of the degree of

Master of Science

Department of Electrical and Computer Engineering
University of Manitoba
Winnipeg, Manitoba, Canada

Abstract

This thesis studies the role of antennas in the achievable resolution and accuracy from near-field microwave tomography (MWT). Near-field MWT is an emerging imaging modality in which the object being imaged is successively irradiated by several antennas, located close to the object, in the microwave frequency range. The scattered fields emanating from the object are then processed to form quantitative images from the dielectric properties of the object.

This thesis starts with proposing a mathematical framework to study the achievable resolution from MWT. Within this framework, the effect of the near-field distribution of the utilized antennas on the achievable image resolution will be studied. Specifically, it will be shown that the use a focused near-field distribution to irradiate the object can enhance the achievable resolution. Within the same framework, the effects of the frequency of operation, multiple frequencies of operation, signal-to-noise ratio of the measured data, and the number of antenna elements on the achievable resolution and accuracy will be studied.

After establishing the importance of the antenna's incident field distribution, this thesis continues with investigating two different methods to achieve a focused near-field distribution. The first method, which attempts to synthesize focused beams from existing omnidirectional antenna elements, will be shown to be not successful using the method employed in this thesis. The second method is based on modifying an existing antenna element so as to make its near-field distribution more focused. Through different experiments and simulations, it will be shown that the second method can make the near-field distribution of the antenna more focused while maintaining multiple frequencies of operation for the antenna, and keeping its physical size reasonably small.

Contributions

This thesis reports on the following contributions. After each contribution, the published or submitted papers that correspond to that contribution will be listed.

- A mathematical framework was proposed to study the achievable resolution from microwave tomography. This framework does not rely on simplified scattering approximations. The effects of several antenna-related parameters on the achievable resolution and accuracy were investigated using this framework.
  - **Nozhan Bayat** and Puyan Mojabi, "A Mathematical Framework to Analyze the Achievable Resolution From Microwave Tomography," submitted, 2014.
- It was shown that the use of focused near-field distributions to irradiate the object being imaged can enhance the achievable resolution.
  - **Nozhan Bayat** and Puyan Mojabi, "The Effect of Antenna Incident Field Distribution on Microwave Tomography Reconstruction," *Progress In Electromagnetics Research*, vol. 145, 153-161, 2014.
  - **Nozhan Bayat** and Puyan Mojabi, "On the Effect of Antenna Illumination Patterns on the Accuracy and Resolution of Microwave Tomography," *IEEE International Symposium on Antennas and Propagation and USNC-URSI Radio Science Meeting*, Orlando, Florida, July 2013.
- Use of synthesized focused beams in microwave tomography was investigated.
  - **Nozhan Bayat**, Puyan Mojabi, and Joe LoVetri "Use of Synthesized Fields in Microwave Tomography Inversion," *International Symposium on Antenna Technology and Applied Electromagnetics*, Victoria, British Columbia, Canada, July 2014.

- An antenna design, fabrication, and measurements were presented so as to make the near-field distribution of an existing antenna more focused.
  - **Nozhan Bayat** and Puyan Mojabi, "Small Wide-band Antenna with more Focused Incident Field for increasing the Accuracy and Resolution of Microwave Tomography," *IEEE International Symposium on Antennas and Propagation and USNC-URSI Radio Science Meeting*, Memphis, Tennessee, USA, July 2014.

Finally, it should be noted that the utilized inversion algorithms in this thesis were previously developed by Puyan Mojabi. These algorithms were used by the author of this thesis throughout this research.

Acronyms and Symbols

Herein, two tables are presented. The first table lists some of the important acronyms used in this thesis, and the second lists some of the important symbols.

Acronym	**Description**
MWT	Microwave tomography.
OI	Object of interest.
TM	Transverse magnetic.
MR-GNI	Multiplicative regularized Gauss-Newton inversion.
SVD	Singular value decomposition.
2D	Two-dimensional.
3D	Three-dimensional.
SNR	Signal-to-noise ratio.
PNFR	Planar near-field range.
VNA	Vector network analyzer.

Symbol	Description
$\hat{x}$, $\hat{y}$, $\hat{z}$	Unit vectors along x, y and z directions.
j	Imaginary unit ($j^2 = -1$).
$\mathcal{D}$	Imaging domain.
$\mathcal{S}$	Measurement domain.
$\boldsymbol{p}$	Position vector in the measurement domain $\mathcal{S}$.
$\boldsymbol{q}$	Position vector in the imaging domain $\mathcal{D}$.
$\boldsymbol{r}$ and $\boldsymbol{r}'$	General position vectors.
$g(.,.)$	Green's function of the background medium.
k_b	Wavenumber of the background medium.
λ	Wavelength of the operation in the background medium.
E^{inc}	Incident electric field (electric field in the absence of the object of interest).
E	Total electric field (electric field in the presence of the object of interest).
E^{scat}	Scattered electric field ($E^{\text{scat}} \triangleq E - E^{\text{inc}}$).
E^{meas}	Measured scattered electric field on the measurement domain $\mathcal{S}$.
$(.)^H$	Hermitian operator (complex conjugate transpose).
$\vert\vert x\vert\vert$	L_2 norm of the vector x, defined as $\vert\vert x\vert\vert \triangleq \sqrt{x^H x}$.
Re	Real-part operator.
Im	Imaginary-part operator.
$\chi(\boldsymbol{q})$	dielectric contrast of the object of interest at location $\boldsymbol{q}$.
$\epsilon_r(\boldsymbol{q})$	Relative complex permittivity of the object of interest at location $\boldsymbol{q}$.
ϵ_b	Relative complex permittivity of the background medium.
S_{11}	Voltage reflection coefficient at the input port (of the antenna).

Acknowledgments

First, I would like to thank my academic advisor, Dr. Puyan Mojabi, for all of his support, encouragement, and time during my MSc studies.

I would also like to express my appreciation to my MSc committee, Dr. Gregory Bridges and Dr. Jonathan Regehr, for their efforts in the evaluation and improvement of this work.

I would also like to thank Mr. Brad Tabachnick, Mr. James Dietrich, Mr. Zoran Trajkoski, and Mr. Dwayne Chrusch for their help in fabrication and measurements.

Finally, I extend my gratitude to Natural Sciences and Engineering Research Council of Canada, the University of Manitoba Research Grant Program, and the University of Manitoba GETS Program for their financial support.

To my parents and my brother Navid

Contents

List of Tables

List of Figures

1

Introduction

This chapter starts with providing an overview on microwave tomography (MWT). It will then discuss the current state of the art in MWT. The scope and novelties of this thesis will then follow. Finally, the outline of this thesis will be presented.

1.1 Microwave tomography

Microwave tomography is an imaging technique which is mathematically formulated as an electromagnetic inverse problem. In general, an inverse problem deals with characterizing an object of interest (OI) by performing some measurements outside the OI. In other words, an inverse problem attempts to infer the internal properties of the OI from external measurements. In MWT, the internal property to be found is the dielectric profile of the OI, and the external data are electromagnetic field measurements performed at the microwave frequency range. That is, in MWT, the dielectric profile of the OI is to be found from microwave measurements collected outside the OI. We note that the term “profile” is used here to indicate that the dielectric property of the OI can have spatial variations. That is, the OI’s dielectric property is a function of spatial coordinates.

To collect microwave measurements in MWT, the OI is successively illuminated by a number of antennas, often placed around the OI. When the incident field of the irradiating antenna element interacts with the OI, scattered electromagnetic fields will arise. These scattered fields carry information about the internal dielectric properties of the OI that can later be used to reconstruct these properties. These scattered fields will then be captured by some receiving antennas located outside the OI. Once the scattered fields due to all the irradiating antennas are collected and calibrated, they will be given to an appropriate processing algorithm so as to reconstruct the dielectric profile of the OI. This processing algorithm, which effectively solves the associated electromagnetic inverse scattering problem, is usually referred to as a nonlinear inversion algorithm, or simply an inversion algorithm or reconstruction algorithm [4]. In fact, the information about the dielectric profile of the OI has been encoded in the measured scattered fields. It is then the responsibility of the utilized nonlinear inversion algorithm to decode this information by processing the measured scattered data.

MWT is a quantitative imaging modality; i.e., it finds the quantitative values associated with the dielectric profile of the OI. Specifically, it finds the relative complex permittivity values corresponding to different parts of the OI. The real part of this relative complex permittivity value represents the relative permittivity profile of the OI, and its imaginary part is proportional to the conductivity profile of the OI. Therefore, for a given OI, MWT creates two quantitative images: real-part and imaginary-part of the OI’s relative complex permittivity. Thus, MWT differs from microwave radar-based imaging techniques (e.g., see [5]) in the sense that microwave radar-based imaging techniques creates a qualitative image from the OI whereas MWT forms quantitative images. In other words, MWT provides more information about the OI as compared to microwave radar-based imaging methods. MWT owes this advantage mainly to its use of advanced inversion algorithms.

MWT has several potential applications, e.g., biomedical diagnosis [4, 6], non-destructive evaluation [7, 8], and through-wall imaging [9]. Specifically, MWT as a biomedical imaging tool is of particular interest due to its potential applications for breast cancer screening [10–12], ischemia detection in different parts of the body [13], lung cancer detection [14], bone imaging [15], and brain imaging [16], etc. Semenov has recently provided a review on various potential biomedical applications of MWT [14]. In particular, the ability of MWT to provide quantitative images can be very useful for clinical applications; e.g., to find out the stage of an illness, to evaluate tumor progression/regression [17], etc. Moreover, due to the fact that MWT utilizes low-power non-ionizing radiation, as opposed to x-ray computed tomography (CT), and also due to the fact that it is not very expensive, as opposed to magnetic resonance imaging (MRI), it can be very useful for frequent large-scale screening applications.

1.2 Current state of the art in MWT

Although there are several potential biomedical and industrial applications for MWT, this imaging modality has not found its firm place as a clinical or an industrial imaging modality. This is mainly due to the fact that the current state-of-the-art achievable resolution and quantitative accuracy from MWT is not sufficient. To this end, several research groups have proposed different techniques to enhance the MWT achievable resolution and accuracy. Broadly speaking, all these techniques fall within one of the following two categories [18]:

1. Collecting more scattering information from the OI, and
2. Processing the collected scattering information in a better (in a more clever) way.

Below, some of the utilized techniques within these two categories that have been used to enhance the MWT resolution and accuracy are listed.

- Use of multiple-frequency scattering data sets [19],
- Use of more receiving antennas based on the modulated scattering technique [20],
- Use of different boundary conditions [21],
- Use of suitable data calibration techniques [22],
- Use of more advanced inversion and regularization techniques [23, 24],
- Reducing the so-called MWT modeling error [25],
- Use of *a priori* information in the utilized inversion algorithm [26],
- Use of appropriate Green's function [27], and
- Use of transverse magnetic and transverse electric data sets simultaneously [28].

Although some of the above techniques have been successfully used, the MWT research community still does not have solid understanding about the MWT achievable resolution limit and its quantitative accuracy for different measurement scenarios and for different OIs. For example, the role of the following parameters in the achievable resolution is not clearly understood: choice of the frequency(ies) of operation, signal-to-noise ratio of the measured data, incident field distribution of the illuminating antennas, number of transceivers and their spatial distribution, transmit/receive polarizations, the boundary condition(s) associated with the MWT system, choice of the background medium, etc. As will be discussed in chapter 4, in the author's opinion, this is mainly due to the lack of a mathematical framework using which the achievable resolution and accuracy from MWT can be systematically studied. If an appropriate mathematical framework existed for such analysis, it could be used to systematically perform the followings.

1. Design appropriate MWT systems tailored for different applications so as to meet their resolution and quantitative accuracy requirements.
2. Develop and invent new techniques so as to increase the achievable resolution limit and quantitative accuracy.

1.3 Novelties of this thesis

In response to the aforementioned need, this thesis first proposes a mathematical framework to analyze the achievable resolution from MWT. As will be seen, as opposed to several existing frameworks, the proposed framework in this thesis is not based on the Born or similar approximations; thus, it is more accurate than the existing frameworks. The core of this framework revolves around investigating the spatial frequency contents of the so-called right singular vectors and the number of the right singular vectors that can be used toward reconstruction of the unknown dielectric profile.

Based on this proposed framework, a novel method to achieve better resolution from MWT will be proposed. This method is based on using focused incident field distributions to irradiate the OI. The effect of several other parameters, governed by the antenna element used in a given MWT system, such as the frequency of operation, simultaneous use of different frequencies of operation, and the number of transceivers are also investigated based on this framework. Finally, based on the lessons learned from this framework, an antenna element for MWT applications is designed and fabricated by modifying an existing antenna element. This antenna is then tested using a planar near-field antenna range (PNFR).

1.4 Scope of this thesis

The above section described the novelties of this thesis. We now discuss the scope of this thesis in the following four subsections.

1.4.1 2D versus 3D

In general, four different forms of MWT have been presented in the literature:

1. Two-dimensional (2D) transverse magnetic (TM) MWT (e.g., see [11]),
2. 2D transverse electric (TE) MWT (e.g., see [29]) ,
3. Three-dimensional (3D) scalar MWT (e.g., see [30]), and
4. 3D vectorial MWT [31]

In 2D MWT, the data collection is often performed on a ring around the OI, and then the dielectric profile image from the cross section of the OI which is in the same plane as the measurement ring is formed. In 2D TM MWT, the irradiation of the OI is performed by the electric field component that is perpendicular to the imaging plane, whereas in 2D TE MWT, the illumination of the OI is performed by the electric field component that lies within the imaging plane. At the current state-of-the-art, it is not clear under what conditions 2D TM

MWT might outperform 2D TE MWT and vice versa. However, most successful experimental imaging results have been reported for 2D TM MWT. In 3D MWT systems, 3D images will be obtained from the OI, and the data collection is often performed on several rings around the OI. In 3D scalar MWT, it is assumed that one component of the vectorial electric field is dominant inside the OI, thus, numerically assuming the presence of only one electric field component inside the OI. However, in 3D vectorial MWT, it is assumed that the three vectorial components of the electric field are all present in the OI. In this thesis, we target 2D TM MWT as it is the most common form of MWT due to (1) ease of implementation, and (2) the better balance between the number of unknowns and known quantities in the associated mathematical problem. (We have elaborated more on this issue in Appendix A.)

1.4.2 Time domain versus frequency domain

To continue our discussion regarding the scope of this thesis, it should be noted that, in general, MWT systems can be implemented in the time-domain or in the frequency-domain (time-harmonic). In frequency-domain systems, the OI is illuminated by a sinusoidal wave having a fixed angular frequency ω, whereas in time-domain systems, the OI is illuminated by a pulse having a broad range of frequencies. In frequency-domain MWT systems, the OI can still be illuminated by sinusoidal waves having different angular frequencies, but this requires performing multiple experiments, each of which is concerned with one frequency. Most MWT systems are designed in the frequency-domain. This is mainly due to the fact that using frequency-domain systems, the resulting signal-to-noise ratio of the measured data will be higher. Thus, in this thesis, we consider frequency-domain MWT systems. Specifically, we assume a time-harmonic dependency of $\exp(-j\omega t)$ where $j^2 = -1$ and t denotes the time.

1.4.3 Dielectric profile versus magnetic profile

MWT systems can be used to reconstruct both the magnetic and dielectric properties of the OI. For example, in [32], an inversion algorithm to simultaneously reconstruct the dielectric and magnetic properties of the OI has been proposed. To the best of the author's knowledge, there are no experimental results available for the simultaneous reconstruction of dielectric and magnetic properties of the OI. In this thesis, it is assumed that the OI and the background medium in which the OI is immersed are non-magnetic. That is, their magnetic properties are the same as the magnetic property of free space.

1.4.4 Near field versus far field

Finally, the placement of the antenna elements in the MWT chamber can be in such a way that the antenna elements work in their near-field zones or in their far-field zones.[1] In most MWT systems, the antenna elements are placed close to the OI, thus, operating in their near-field zones. This results in (1) making the MWT system more compact, (2) having better signal-to-noise ratio in the measured data, and (3) having the chance to capture evanescent waves emanating from the OI. In this thesis, we consider the near-field MWT configuration.

[1] The far-field zone of an antenna starts from a distance away from the antenna, say r_{FF}, and then goes to infinity. To find r_{FF}, we often need to find the largest value between the following two quantities: $2D^2/\lambda$ and 10λ where D is the largest dimension of the antenna and λ is the wavelength in the medium. For small antennas, 10λ is the largest number, and therefore for small antennas, the far-field zone starts from 10λ. In other words, for small antennas, the near-field zone will cover distances that are smaller than 10λ from the antenna. (On the other hand, for large antennas, $2D^2/\lambda$ will be the dominant value.)

1.5 Outline of this thesis

The present chapter defined the scope of this thesis and briefly described its novelties. Chapter 2 presents the mathematical formulation of the MWT problem based on its integral equation formulation. The key part in Chapter 2 is the discussion on the flow of information from the imaging domain to the measurement domain.

Chapter 3 provides a mathematical framework to analyze the achievable resolution from MWT. This framework is built on the mathematical formulation presented in Chapter 2. To understand this framework better, the effect of signal-to-noise ratio of the measured data on the achievable resolution is investigated at the end of Chapter 3.

The effects of several antenna-related parameters on the MWT achievable resolution and accuracy are studied in Chapter 4 using the framework presented in the previous chapter. Most importantly, the use of focused near-field distributions to irradiate the object so as to enhance the resolution will be presented. In addition, the effects of the frequencies of operation (governed by the bandwidth of the antennas) and the number of transceivers (governed by the physical size of the antennas) on the achievable resolution and accuracy will be investigated.

Chapters 5 and 6 are concerned with the implementation of focused near-field distributions from two different viewpoints. Chapter 5 attempts to achieve this by the use of synthesized fields. It will be shown that the proposed synthesized-field method in this chapter is not successful. On the other hand, Chapter 6 attempts to create this focused near-field distribution by designing an antenna element. This antenna element, which was designed by modifying an existing antenna element, showed improved near-field focusing as compared to the original antenna. This observation was supported by simulation and experimental data. Finally, Chapter 7 concludes this thesis and provide some potential future works that can be pursued.

2

Formulation

In this chapter, two basic equations, namely, data and domain equations, that govern the wave interaction in the MWT problem are presented. Enabled by these two equations, we will then start discussing some important parameters that affect the achievable resolution and accuracy from MWT. In particular, we intuitively discuss the role of antennas in the MWT achievable resolution and accuracy. This intuitive understanding will later be supported by the proposed mathematical framework for the MWT resolution analysis, which is to be presented in the next two chapters, and also the MWT antenna design, which is to be presented in Chapter 6.

2.1 Definitions

Before starting with the data and domain equations, let's first define three different terms which will be used throughout this thesis; namely, incident, total, and scattered electric fields. The incident electric field, $\boldsymbol{E}^{\text{inc}}(\boldsymbol{r})$, is defined as the electric field at location $\boldsymbol{r}$ when the OI is not present in the MWT system. The total electric field, $\boldsymbol{E}(\boldsymbol{r})$, is defined as the electric field at location $\boldsymbol{r}$ when the OI is present in the MWT system. Finally, the scattered electric field, $\boldsymbol{E}^{\text{scat}}(\boldsymbol{r})$, is simply defined as the difference between the total and incident electric fields; i.e.,

$$\boldsymbol{E}^{\text{scat}}(\boldsymbol{r}) \triangleq \boldsymbol{E}(\boldsymbol{r}) - \boldsymbol{E}^{\text{inc}}(\boldsymbol{r}). \tag{2.1}$$

Therefore, to obtain the scattered electric field values, two sets of experiments need to be performed: one in the presence of the OI, and the other in the absence of the OI. Since, in this thesis, the electric field formulation is chosen for the MWT problem, we may refer to incident, total and scattered electric fields simply as incident, total, and scattered fields respectively (i.e., dropping the word "electric").

Also, as noted in Section 1.4, we consider the 2D TM MWT problem. Therefore, in this thesis, we assume that only one component of the electric field exists, and that component is perpendicular to the imaging domain. Therefore, we choose to drop the bold letters used in (2.1), and show them as $E^{\text{scat}}(\boldsymbol{r})$, $E(\boldsymbol{r})$, and $E^{\text{inc}}(\boldsymbol{r})$.

We also define two important geometrical domains: imaging domain and measurement domain. The imaging domain, denoted by $\mathcal{D}$, is the domain that encloses the OI. The measurement domain, denoted by $\mathcal{S}$, is the domain over which the antennas are placed. Due to the fact that MWT is a non-destructive imaging method, the measurement domain $\mathcal{S}$ is outside the imaging domain $\mathcal{D}$. Also, we use the location vector $\boldsymbol{p}$ to indicate that a given location is on the measurement domain; i.e., we assume $\boldsymbol{p} \in \mathcal{S}$. Also, we use $\boldsymbol{q}$ and $\boldsymbol{q}'$ to indicate that that a given location is in the imaging domain; i.e., $\boldsymbol{q} \in \mathcal{D}$ and $\boldsymbol{q}' \in \mathcal{D}$.

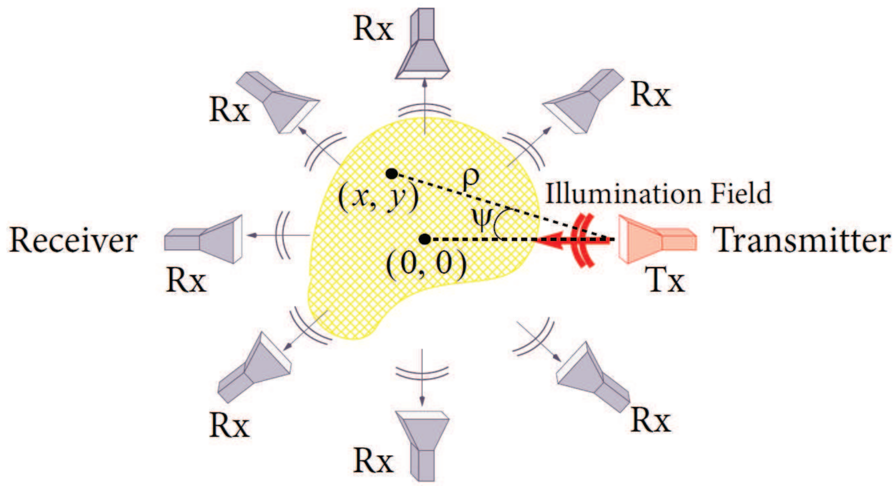

Fig. 2.1: Setup of the MWT problem. Tx and Rx represent the transmitting and receiving antennas respectively. The yellow object is the object of interest. The domain enclosing this object is the imaging domain $\mathcal{D}$. The circle over which the antennas are located is the measurement domain $\mathcal{S}$. These two domains are in the $x - y$ plane. The incident electric fields are assumed to be perpendicular to the imaging domain; i.e., in $\hat{z}$ direction. Once one antenna irradiate the OI (see the red-colored vector), the emanating scattered fields from the object (see the grey-colored vectors) are collected by the receiving antennas.

2.2 How MWT works

Now that we have presented our definitions, let's take a look at Figure 2.1 which shows the schematic of an MWT system. As can be seen, the OI is enclosed by a set of antennas. (The OI and the antennas are all immersed in a background medium, which can be for example air or a matching fluid[1], so as to couple electromagnetic energy more effectively into the OI.) Once a given antenna illuminates the OI, the rest of the antennas collect the resulting electric fields. This procedure continues until all the antennas illuminate the OI. This data collection procedure is performed twice: first in the absence of the OI, and then in the presence of the OI. Subtracting the fields measured in the absence of the OI from the fields measured in the presence of the OI will then result in the scattered field data. The dielectric profile of the OI is then to be reconstructed from this scattered field data set.

[1] For example, water or oil can be a matching fluid for biomedical applications.

2.3 Data equation

Let's start by considering the so-called data equation. This equation establishes a relation between the measured scattered data and the unknown OI's dielectric profile. That is, this equation relates our unknown quantity to the known quantity as [4]

$$\overbrace{E^{\text{scat}}(\boldsymbol{p})}^{\text{known measured data}} = k_b^2 \int_{\mathcal{D}} \overbrace{g(\boldsymbol{p}, \boldsymbol{q}) E(\boldsymbol{q})}^{\text{kernel}} \overbrace{\chi(\boldsymbol{q})}^{\text{unknown}} \, d\boldsymbol{q}. \tag{2.2}$$

where $\mathcal{D}$ denotes the imaging domain in which the OI is located, and k_b is the wavenumber in the background medium.[2] Also, $\chi(\boldsymbol{q})$ denotes the complex electric contrast of the OI defined as

$$\chi(\boldsymbol{q}) \triangleq \frac{\epsilon_r(\boldsymbol{q}) - \epsilon_b}{\epsilon_b}. \tag{2.3}$$

In the above definition, ϵ_b is the known relative complex permittivity of the background medium.[3] The unknown relative complex permittivity of the OI at location $\boldsymbol{q} \in \mathcal{D}$ is denoted by $\epsilon_r(\boldsymbol{q})$. The Green's function of the MWT system is also denoted by $g(\boldsymbol{p}, \boldsymbol{q})$. It should also be reminded that $E(\boldsymbol{q})$ is the total electric field inside the imaging domain. The measured scattered data at the receiving location $\boldsymbol{p}$ is denoted by $E^{\text{scat}}(\boldsymbol{p})$. Note that the receiving point $\boldsymbol{p}$ belongs to the measurement domain $\mathcal{S}$, which is outside the imaging domain $\mathcal{D}$. That being said, the data equation might be thought as the equation that maps the information within the imaging domain, $\mathcal{D}$, to the measurement domain, $\mathcal{S}$.

It should be noted that all of these permittivities, see (2.3), are complex-valued quantities in order to let us model lossy materials. As a result the complex permittivity of the OI at the

[2] Since the background medium is assumed to be nonmagnetic, the background wavenumber will be $k_b = \omega\sqrt{\mu_0\epsilon_0\epsilon_b}$ where μ_0 and ϵ_0 are the permeability and permittivity of air, and ϵ_b is the relative permittivity of the background medium.

[3] The background medium is assumed to be homogeneous; i.e., $\epsilon_b(\boldsymbol{q}) = \text{constant}$.

angular frequency of ω may then be written as

$$\epsilon_r(\boldsymbol{q}) = \epsilon'(\boldsymbol{q}) + j\epsilon''(\boldsymbol{q}) = \epsilon'(\boldsymbol{q}) + j\frac{\sigma(\boldsymbol{q})}{\omega\epsilon_0} \tag{2.4}$$

where $\epsilon'(\boldsymbol{q})$ and $\sigma(\boldsymbol{q})$ represent the relative permittivity and the conductivity of the OI at the angular frequency of ω respectively. As will be seen later on, the MWT images will be quantitative images of $\epsilon'(\boldsymbol{q})$ and $\epsilon''(\boldsymbol{q})$.

2.4 Flow of information

Now that we have briefly described one of the important MWT equations, let's take another look at (2.2) to see what parameters affect the flow of information from the dielectric contrast profile $\chi(\boldsymbol{q})$ to the measured scattered data $E^{\text{scat}}(\boldsymbol{p})$. As can be seen, two important parameters control the flow of information: Green's function of the background medium and the total electric field inside the imaging domain. (As noted in (2.2), the multiplication of these two functions is the kernel of the data equation.)

As it is well-known, the data equation is a Fredholm integral equation of the first kind [33]. This type of integral equations are known to be ill-posed [33]. The ill-posedness of this integral equation indicates that a small change in the measured scattered data can result in a huge change in the reconstructed contrast [34, 35]. In other words, the associated mathematical problem is not stable. The more ill-posed the MWT problem is, the less information will be transferred to the measurement domain.

An important property of this type of Fredholm integral equations is that the smoother the kernel is, the more ill-posed the problem will be [33]. That is, the smoother this kernel is, the less information from the imaging domain will be transferred to the measurement domain.

Therefore, one way to think about maximizing the flow of information from the OI to the measurement domain will be to decrease the degree of ill-posedness by making the kernel of (2.2) less smooth. As noted above, the Green's function of the background medium and the total field within the imaging domain contribute to the kernel of this integral equation. In what follows, we review the role of these two important parameters.

2.5 Green's function

The Green's function $g(\boldsymbol{p}, \boldsymbol{q})$ is the point-source response [36] of the MWT system when the OI is not present in the MWT system. That is, if a point source[4] is placed at location $\boldsymbol{q}$ in the MWT system in the absence of the OI, the field value at location $\boldsymbol{p}$ will be equal to $g(\boldsymbol{p}, \boldsymbol{q})$. In general, the Green's function is dependent on the geometry of the MWT system, its boundary condition, and the frequency of operation. That is, by changing any of these parameters, the Green's function of the MWT system will be changed; thus, the flow of information from the imaging domain to the measurement domain will be affected.

Almost all existing 2D TM MWT systems are designed in such a way that free space Green's function can be assumed as their Green's function. (The use of free-space Green's function indicates that if an electromagnetic wave interrogates the imaging domain, it will not be reflected back to the imaging domain upon leaving the imaging domain.) Therefore, in such systems, the Green's function will be assumed to be

$$\boldsymbol{g}(\boldsymbol{p}, \boldsymbol{q}) \;=\; \frac{1}{4j} H_0^2 \left(k_b \left| \boldsymbol{p} - \boldsymbol{q} \right| \right) \tag{2.5}$$

where $H_0^2\,(.)$ denotes the zeroth-order Hankel function of the second kind. We speculate that the main reason that most successful MWT systems are based on the use of free space

[4] In a two-dimensional configuration, a point source will be an infinite line source.

Green's function is that if other forms of Green's function (e.g., the Green's function of a metallic chamber) is used, the two-dimensional approximation is no longer sufficiently accurate. Therefore, three-dimensional inversion algorithms should be used. On the other hand, three-dimensional inversion algorithms require much more collected data to work properly. And, as described in Appendix A, it is usually very difficult to maintain a reasonable balance between the number of unknowns and the number of known quantities in three-dimensional MWT problems, as opposed to two-dimensional MWT problems. Another reason behind using free space Green's function is that the computational complexity of the utilized nonlinear inversion algorithm can be easily decreased due to the use of the fast Fourier transform. However, the use of appropriate Green's function is still a promising option, and some research groups try to enhance the resolution and accuracy of MWT by changing the Green's function of the background medium; e.g., see [21, 27]. In our research, we assume that the Green's function of the background medium is that of free space, mainly because we are targeting two-dimensional transverse magnetic microwave tomography.

2.6 Total electric field in the imaging domain

The discussion in this section will pave the way toward better understanding a novel method, to be presented in Chapter 4, to enhance the achievable resolution and accuracy from MWT. To this end, let's ask ourselves the following question: *how having control over the total electric field, $E(\boldsymbol{q})$, within the imaging domain may help us solve the MWT problem more accurately?* Before answering this question, let's recall the role of total electric field $E(\boldsymbol{q})$ in the data equation. As noted earlier, the total electric field $E(\boldsymbol{q})$ contributes to the kernel of the data equation integral. We also noted that the smoother this kernel is, the more ill-posed the MWT problem will be [33]. Therefore, if we can create a total electric field distribution inside the imaging domain that makes this kernel less smooth, the associated mathematical problem will be less ill-posed; thus, more accurate reconstruction can be achieved.

The main difficulty in creating a total electric field distribution to make the kernel of the data equation less smooth lies in the fact that the total electric field and the dielectric contrast of OI are dependent on each other. This can be better understood by looking at the so-called MWT domain equation [4]

$$E(\boldsymbol{q}) = E^{\text{inc}}(\boldsymbol{q}) + k_b^2 \int_{\mathcal{D}} g(\boldsymbol{q}, \boldsymbol{q'}) E(\boldsymbol{q'}) \chi(\boldsymbol{q'}) d\boldsymbol{q'}. \tag{2.6}$$

Note that as opposed to the data equation, which establishes a relation between the imaging domain and the measurement domain, the domain equation is only concerned about the imaging domain since $\boldsymbol{q}$ and $\boldsymbol{q'}$ are both in the imaging domain $\mathcal{D}$. Now, let's consider the tools that we have so as to control $E(\boldsymbol{q})$ in order to make the kernel less smooth. As can be seen in 2.6, for a given MWT configuration (i.e., a system with fixed known Green's function), $E(\boldsymbol{q})$ depends on both $\chi(\boldsymbol{q})$ and the incident field distribution $E^{\text{inc}}(\boldsymbol{q})$. Noting that $\chi(\boldsymbol{q})$ is, in fact, the unknown of the problem, it cannot be used to control the total electric field $E(\boldsymbol{q})$ within the imaging domain. For the same reason, we can never completely control the total electric field within the imaging domain. However, by changing the incident electric field $E^{\text{inc}}(\boldsymbol{q})$, we can affect and change $E(\boldsymbol{q})$ within the imaging domain to some extent, thus, affecting the achievable MWT image accuracy and resolution.

2.7 Role of the antenna element

Based on the above formulation, we can now intuitively discuss the role that the antenna elements can play in MWT achievable resolution and accuracy.

2.7.1 Near-field distribution

As described above, the achievable image accuracy and resolution from MWT can be affected by changing the incident field distribution within the imaging domain. In Chapter 4, this idea will be used to enhance the achievable resolution and accuracy. The incident field distribution is, in fact, the field distribution of the antenna element in the absence of the OI. That is, the incident field distribution is a property of the antenna element independent from the OI. Noting that antenna elements in most MWT systems operate in their near-field zones (as noted in Section 1.4), the near-field distribution of the utilized antenna element is, in fact, the incident field distribution in the MWT problem. Thus, the near-field distribution of the antenna will then contribute toward the achievable accuracy and resolution from MWT. We will elaborate on this idea further in Chapters 4 and 6. [5]

2.7.2 Size and the frequency(ies) of operation

As will be discussed in more details in Chapter 4, two other antenna parameters will also affect the achievable resolution and accuracy from MWT. These two parameters are the frequency of operation, or the frequencies of operation, and the antenna physical size. Herein, we discuss the effect of these two parameters in an intuitive way. To start our discussion regarding these two parameters, we note that an MWT nonlinear inversion algorithm often attempts to minimize the so-called data misfit cost functional. (Appendix B provides a brief description about this cost functional.) As noted in Appendix B, this data misfit cost functional depends on the number of transmitters, nTx, number of receivers per transmitter, nRx, and the number of frequencies of operation, nf. Therefore, intuitively, it can be easily understood that the more data points we can collect, the more successful reconstruction we

[5] This is in contrast to most published works in the area of MWT antenna design that consider the far-field pattern of the antenna element, as opposed to its near-field distribution.

can have. To collect more data points, we need to increase nTx and nRx which we collectively refer to as the number of transceivers. To increase the number of transceivers, the physical size of the antenna elements need to be small so that more antennas can be placed in the measurement domain. (We also note that the separation between the successive antenna elements cannot be very small as this results in mutual coupling between the antenna elements.) Also, it is beneficial to have multiple frequencies of operation for the antenna element so as to increase nf, thus, increasing the overall data points.

2.7.3 Signal to noise ratio

As will be seen in Chapter 3, the signal-to-noise ratio of the measured scattered data plays an important role on the achievable image resolution and accuracy. In the MWT problem, in addition to the measurement noise, several other parameters contribute to the overall noise of the data. For example, as can be seen in (2.6), the utilized inversion algorithm requires the knowledge of the incident field distribution within the imaging domain. However, in most existing MWT systems, an analytical form of the incident field is often assumed (e.g., incident field due to a line source). Any discrepancy between the actual antenna's incident field distribution inside the imaging domain with this assumed analytical distribution will then contribute to the overall noise of the system. As will be seen in Chapter 6, we will measure the actual incident field distribution of the antenna, which may later be used in the inversion algorithm so as to reduce the overall noise. Also, in 2D TM MWT, any reflections that come from the top and bottom of the imaging plane will contribute toward the overall noise of the measured data as the 2D inversion algorithm cannot take those reflections into account. As will be seen in Chapter 6, near-field measurements can be performed to compare this 2D modeling error for two different antennas. Finally, if free-space Green's function is used, the presence of the antenna and the mutual coupling between the antenna elements are not modeled within this Green's function. This will also contribute to the overall noise of the MWT data. Therefore, as can be seen, several antenna-related parameters affect the overall noise of the MWT problem.

3

Resolution Analysis Framework

As noted earlier, in order to make MWT a viable imaging technique, it is important to have solid understanding about its achievable resolution and accuracy limit for different measurement scenarios and different OIs. In this chapter, a mathematical framework using which such analysis on the achievable resolution can performed will be presented.[1] This understanding may then be used to design appropriate MWT systems tailored for different applications so as to meet their resolution requirements. As will be seen in this chapter, we first discuss why the nonlinearity of the MWT problem makes the analysis of the MWT achievable resolution difficult. We then describe how we will handle this nonlinearity so as to be able to develop our mathematical framework. The singular value decomposition of the operator mapping the dielectric properties of the OI to the measured scattered data is then briefly discussed. Based on this singular value decomposition as well as the collected measured data, two important criteria for performing resolution analysis will be discussed:

[1] This chapter is based on the following submitted work: N. Bayat and P. Mojabi, "A Mathematical Framework to Analyze the Achievable Resolution From Microwave Tomography," Submitted in 2014.

(1) spatial frequency components of the right singular vectors, and (2) the number of right singular vectors that can be used toward dielectric profile reconstruction. These two criteria will then serve as our mathematical framework for performing resolution analysis in the rest of this chapter as well as the next chapter which revolves around considering several numerical and experimental examples.

Before starting this chapter, let's have a brief overview of some of the important works that have been already done in the area of MWT resolution analysis. In an earlier work [37], a mathematical framework for studying the achievable resolution from linear inversion methods has been presented. The authors of [37] have then investigated why the choice of nonlinear inversion algorithms can result in enhanced resolution compared to the use of linear inversion methods. In contrast to [37], here, we attempt to provide its mathematical framework directly for nonlinear inversion algorithms. Also, a few other papers, e.g., [38, 39], have quantified the resolution achievable from an experimental MWT system for a few targets. In contrast to those papers, we do not aim to quantify the achievable resolution from a given experimental system, but attempt to provide a mathematical framework so that the achievable resolution limit from any MWT systems can be better studied. The core of this framework is borrowed from a mathematical framework that was recently used to solve the discretized linear Fredholm integral equation of the first kind [40]. Herein, this framework is adapted to the discretized nonlinear Fredholm integral equation of the first kind associated with the MWT problem.

3.1 Nonlinearity and Resolution

The nonlinearity of the associated MWT mathematical problem is the main difficulty toward creating a mathematical framework for analyzing the resolution achievable from MWT. In this section, we first elaborate on why this nonlinearity is the main obstacle toward performing MWT resolution analysis. We then propose our utilized method to handle this difficulty.

3.1.1 Nonlinearity

Let's again consider the so-called MWT data equation that maps the dielectric profile of the OI, located within the imaging domain $\mathcal{D}$, to the measured scattered data. This equation which was first shown in (2.2), is repeated here for convenience

$$E^{\text{scat}}(\boldsymbol{p}) = k_b^2 \int_{\mathcal{D}} g(\boldsymbol{p}, \boldsymbol{q}) E(\boldsymbol{q}) \chi(\boldsymbol{q}) d\boldsymbol{q}. \tag{3.1}$$

To analyze the achievable resolution from MWT, we need to analyze the operator that maps the unknown contrast profile, $\chi(\boldsymbol{q})$, to the measured scattered data $E^{\text{scat}}(\boldsymbol{p})$. As can be seen from (3.1), this operator depends on both the Green's function $g(\boldsymbol{p}, \boldsymbol{q})$ and the total field within the imaging domain $E(\boldsymbol{q})$. In other words, as pointed out in Section 2.4, the information flow from the imaging domain to the measurement domain is mainly controlled by these two functions. This is in contrast to linear ill-posed problems, e.g., deblurring problems, in which the information flow is merely controlled by the associated Green's function [41].

The main challenge in analyzing this operator is that the total field $E(\boldsymbol{q})$, which partially defines this operator, is itself a function of the unknown $\chi(\boldsymbol{q})$. This makes this operator dependent on the OI. (This is probably one of the reasons that different resolving abilities have been observed for the same experimental MWT system when imaging different OIs [38].) In fact, the total field $E(\boldsymbol{q})$ is nonlinearly related to $\chi(\boldsymbol{q})$ through the domain equation, which governs the wave interaction merely within the imaging domain. For the convenience in reading, the domain equation, which was first introduced in (2.6) is presented here:

$$E(\boldsymbol{q}) = E^{\text{inc}}(\boldsymbol{q}) + k_b^2 \int_{\mathcal{D}} g(\boldsymbol{q}, \boldsymbol{q\prime}) E(\boldsymbol{q\prime}) \chi(\boldsymbol{q\prime}) d\boldsymbol{q\prime} \tag{3.2}$$

where $\boldsymbol{q}$ and $\boldsymbol{q\prime}$ are both in $\mathcal{D}$. Based on the above discussion, it can be concluded that the measured data is nonlinearly related to the unknown contrast profile. (The physical reason behind this nonlinearity is the presence of multiple scattering events within the OI, which is of course dependent on the OI itself.) Therefore, the first step toward providing a mathematical framework to analyze the achievable resolution from MWT is to decide how to handle this nonlinearity in this analysis. This will be the topic of our next subsection.

3.1.2 How to handle the nonlinearity?

To analyze a nonlinear problem, we often linearize the associated mathematical problem. The main question to be answered will then be how to perform proper linearization. The most popular form of linearization is to use Born approximation in which the total field inside the imaging domain, $E(\boldsymbol{q})$, is assumed to be equal to the known incident field inside the imaging domain, $E^{\text{inc}}(\boldsymbol{q})$. This will make (3.1) a linear equation with respect to the unknown $\chi(\boldsymbol{q})$. However, this approximation is not appropriate in many situations, especially when the dielectric contrast of the OI is not sufficiently small. Specifically, the Born approximation will not take into account the multiple scattering events within the OI, thus, the resulting achievable resolution will suffer [37].

Herein, to linearize (3.1), we do not impose any significant approximations on $E(\boldsymbol{q})$. To this end, we use the following procedure.

1. The measured data $E^{\text{scat}}(\boldsymbol{p})$ is inverted using a nonlinear inversion algorithm. A non-

linear inversion algorithm effectively attempts to model multiple scattering events within the OI. Herein, the multiplicative regularized Gauss-Newton inversion (MR-GNI) algorithm [42, 43] is used as the nonlinear inversion algorithm. This inversion algorithm iteratively updates the total field $E(\boldsymbol{q})$ and the contrast profile $\chi(\boldsymbol{q})$. This state-of-the-art inversion algorithm is described in Appendix C.

2. The total field $E(\boldsymbol{q})$ at the last iteration of the MR-GNI algorithm is calculated. This calculated total field is denoted by $\bar{E}(\boldsymbol{q})$. For a given inversion algorithm, assuming that the regularization weight is chosen properly, this calculated total field will represent the most accurate estimate of the multiple scattering events within the OI that the inversion algorithm can recover.

3. This calculated total field will then be used in (3.1) to linearize the data equation with respect to $\chi(\boldsymbol{q})$. That is, the linearized equation will be

$$\overbrace{E^{\text{scat}}(\boldsymbol{p})}^{\text{known measured data}} = \overbrace{k_b^2 \int_{\mathcal{D}} g(\boldsymbol{p}, \boldsymbol{q}) \bar{E}(\boldsymbol{q})}^{\text{known linearized operator}} \overbrace{\chi(\boldsymbol{q})}^{\text{unknown}} \, d\boldsymbol{q} \tag{3.3}$$

We have now a linearized map between the unknown dielectric profile and the measured data. (It should be noted that this type of linearization has been previously used for image enhancement of MWT final reconstructions [44].) The mathematical treatment of this linearized mapping for resolution studies is the focus of the next section.

3.2 *Mathematical Framework for Resolution Analysis*

Now that we have arrived at the linearized data equation, given in (3.3), we need to analyze this linearized operator in conjunction with the measured data in order to understand how different parameters affect the achievable resolution. To this end, we discretize (3.3) as

$\boldsymbol{A}\chi = b$ where b is a complex vector of length m containing the measured data points[2], χ is a complex vector of length n containing the contrast values at each discretized cell of the imaging domain[3], and $\boldsymbol{A}$ is a $m \times n$ complex matrix, which is the discretized form of the integral equation operator in (3.3)[4]. As can be seen, the matrix $\boldsymbol{A}$ mainly depends on the Green's function of the background medium and the total field $\bar{E}$. Also, notice that without the linearization presented in Section 3.1.2, we were not able to reach to this linearized system of equations, $\boldsymbol{A}\chi = b$.

Herein, for the reasons that will be discussed in the next section, we use the singular value decomposition (SVD) of $\boldsymbol{A}$ to analyze the equation $\boldsymbol{A}\chi = b$. To this end, let's denote the SVD of $\boldsymbol{A}$ by $\boldsymbol{U\Sigma V}^H$ where the superscript H denotes the Hermitian (complex conjugate transpose) operator, $\boldsymbol{U}$ is an $m \times m$ orthonormal matrix consisting of left singular vectors of the matrix $\boldsymbol{A}$, and $\boldsymbol{V}$ is an $n \times n$ orthonormal matrix consisting of right singular vectors of the matrix $\boldsymbol{A}$. That is,[5]

$$\boldsymbol{U} = \begin{bmatrix} u_1 & u_2 & u_3 & \cdots & u_m \end{bmatrix} \quad \text{where} \quad u_i \in \mathbb{C}^m \tag{3.4}$$

$$\boldsymbol{V} = \begin{bmatrix} v_1 & v_2 & v_3 & \cdots & v_n \end{bmatrix} \quad \text{where} \quad v_i \in \mathbb{C}^n. \tag{3.5}$$

Also, $\boldsymbol{\Sigma}$ is an $m \times n$ rectangular diagonal matrix containing the singular values of the matrix $\boldsymbol{A}$, denoted by σ_i, on its diagonal entries. These singular values are non-negative real numbers of descending magnitude; i.e., $\sigma_i > \sigma_{i+1} \in \mathbb{R}^+$.[6] Using the SVD of the matrix $\boldsymbol{A}$,

[2] That is, the column vector b stores $E^{\text{scat}}(\boldsymbol{p})$.
[3] That is, the column vector χ is the discretized version of $\chi(\boldsymbol{q})$.
[4] That is, the matrix $\boldsymbol{A}$ is the discretized form of the linearized data equation operator.
[5] $\mathbb{C}$ denotes complex numbers.
[6] $\mathbb{R}^+$ denotes positive real numbers

the discretized contrast χ can be written as [33]

$$\chi = \sum_{i=1}^{\min(m,n)} \frac{u_i^H b}{\sigma_i} v_i. \tag{3.6}$$

The above equation indicates that the solution χ

1. lies within the space of right singular vectors v_i,
2. is the summation of the first $\min(m, n)$ right singular vectors, each of which has a weight of $u_i^H b/\sigma_i$.

In the next section, we will show how (3.6) can be used to perform MWT resolution analysis.

3.3 MWT Resolution Analysis

The core of our resolution analysis is based on considering (3.6). Specifically, the proposed MWT resolution analysis is based on analyzing (3.6) by considering

1. the spatial frequency contents of right singular vectors, and
2. the number of the right singular vectors that can be utilized for reconstruction.

In this section, we discuss how each of these two items contributes toward the achievable MWT resolution.

3.3.1 *Spatial frequency contents of right singular vectors*

The key idea behind using (3.6) for resolution analysis lies within the fact that that the right singular vectors v_i have properties similar to the Fourier series' basis functions. Specifically, right singular vectors v_i of small indices i have mainly low spatial frequency components [40]. As the index i increases, the corresponding v_is will then have higher spatial frequency contents [40]. This indicates that as the index i in (3.6) increases, the summation will try to incorporate more higher spatial frequencies into the solution χ. Therefore,

- to obtain a low-resolution MWT image, the use of a few v_is of small indices will be sufficient;
- to achieve a high-resolution image, v_is having larger indices should also be incorporated into the summation.
- the highest spatial frequency in the reconstructed contrast χ cannot be larger than the highest spatial frequency available in the right singular vectors v_is.

To use this idea in the rest of this thesis, we need to have a tool to evaluate the spatial frequency contents of the right singular vectors in different measurement scenarios. To this end, we use the power spectrum of the right singular vectors as used in [40]. This can be done by taking the Fourier transform of the vectors v_i and then finding their power spectra. Noting that the scope of this thesis is cross-section reconstruction in the xy plane, each v_i will therefore be a function of (x, y) where (x, y) is the location of the discretized cell within the imaging domain at which v_i is evaluated. Thus, we need to take the two-dimensional (2D) Fourier transform of the vectors $v_i(x, y)$. To this end, we perform the following procedure

- Each column vector v_i will be first reshaped into a matrix having the same size as the discretized 2D imaging domain.
- A 2D Fourier transform will then be taken from this matrix, which we refer to as $\tilde{v}_i(f_x, f_y) = \mathcal{F}\{v_i(x, y)\}$ where f_x and f_y are spatial frequency indices along the x and y directions. (The Fourier transform $\mathcal{F}$ is performed using the MATLAB function *fft2* in conjunction with the MATLAB function *fftshift* to bring the zero spatial frequency to the center of the spectrum.)
- the power spectrum of a given right singular vector, say v_i, will then be represented by $|\tilde{v}_i(f_x, f_y)|^2$.

We now have n different 2D power spectra. Herein, to be able to compare the spatial frequency contents of the power spectra of different v_is within the same plot, we choose to plot only one cut of $|\tilde{v}_i(f_x, f_y)|^2$ for each v_i. Specifically, we plot $|\tilde{v}_i(f_x, f_y = 0)|^2$ against different f_x and i indices.

As will be seen later, this plot is similar to a rotated “V” letter where the apex of the “V” represents the zero spatial frequency component. As the index i increases, the aperture of the “V” increases; thus, incorporating higher spatial frequency components. Therefore, based on this plot, we are able to study the spatial frequency components of the right singular vectors which directly affect the spatial frequency components of the reconstructed contrast.

3.3.2 Number of the utilized right singular vectors

To achieve a high resolution image, the reconstructed contrast should have high spatial frequency components. Therefore, based on the discussion presented in the previous subsection, it can be concluded that it is desirable to incorporate as many v_is as possible into the

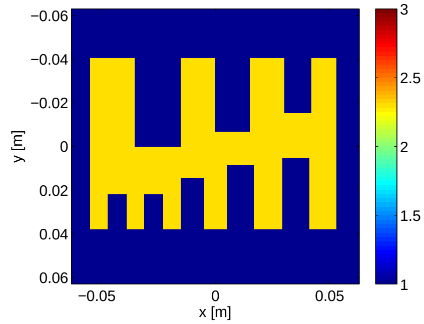

(a) True $Re(\epsilon_r)$

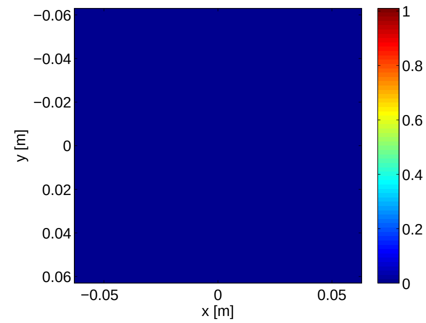

(b) True $Im(\epsilon_r)$

Fig. 3.1: Relative complex permittivity of the *E*-target.

reconstructed χ so as to be able to resolve small features within the OI. Therefore, we now need to address the number of right singular vectors that can be incorporated into the reconstructed contrast χ.

To start this discussion, let's consider (3.6). From this equation, it might be mistakenly concluded that we can always incorporate $\min(m, n)$ right singular vectors into the reconstructed contrast. However, as it is well-known, this is not the case due to the ill-posedness of the problem [33]. This can be explained by studying the behavior of the coefficients of the right singular vectors in (3.6); i.e., $u_i^H b/\sigma_i$. In such ill-posed problems, as the index i increases, the singular values σ_is (the denominators of the coefficients) tend to become smaller and smaller. Now, let's study the numerators of these coefficients. To this end, assume that the data vector b consists of a noiseless component, say b^{true}, and a noisy component, say e. (That is, $b = b^{\text{true}} + e$.) If we had access to b^{true}, the magnitude of $u_i^H b^{\text{true}}$ would also decrease with a rate at which for large i indices the magnitude of $u_i^H b^{\text{true}}$ would be always less than σ_i [45]. Therefore, although as i increases, σ_is become smaller and smaller, the coefficients $u_i^H b^{\text{true}}/\sigma_i$ would never blow up [45]. If b^{true} was available, we could always use $\min(m, n)$ right singular vectors to reconstruct χ. However, we would never have access to b^{true} mainly due to the presence of the measurement noise and modeling error. To understand this better, let's assume that the only source of noise in the measured data b is the numerical noise, say round-off error denoted by e. As discussed in [40], the magnitude of $u_i^H e$ will not decrease as i increases. It is, in fact, almost constant, often much larger than the smallest singular value. Due to the presence of e in the measured data b, the magnitude of $u_i^H b/\sigma_i$ will eventually blow up. This is usually referred to as the instability of the problem, and if not treated by the use of appropriate regularization techniques results in a non-physical solution. In practical situations, measurement noise and modeling error also contribute toward the overall noise of the data vector b. Therefore, due to the presence of this noise, the summation given in (3.6) needs to be terminated early. That is, the number of utilized right singular vectors will be less than $\min(m, n)$.

As pointed out in the previous subsection, it is critical to incorporate v_is with large i indices into the reconstructed contrast to achieve a high-resolution image. However, from the above discussion, we know that we cannot include all the v_is due to the instability of the associated mathematical problem. This will result in not using all the right singular vectors that are available. Based on what has been said above, this indicates that the final solution will suffer from not having some high spatial frequency components. Now, if those high spatial frequency components are needed to successfully reconstruct a feature in the OI, the reconstructed image will not show that feature. This will then limit the achievable resolution from MWT.

Now, we need a tool based on which we can determine how fast $u_i^H b/\sigma_i$ coefficients will blow up. This is important because the faster these coefficients blow up, the smaller number of v_is can be used toward contrast reconstruction. The tool we use here is simply based on plotting the magnitude of the coefficients $u_i^H b/\sigma_i$ versus the index i. As will be seen later, this simple plot, in conjunction with the power spectrum plot discussed in the previous subsection, enables us to compare different scenarios for MWT applications in terms of the

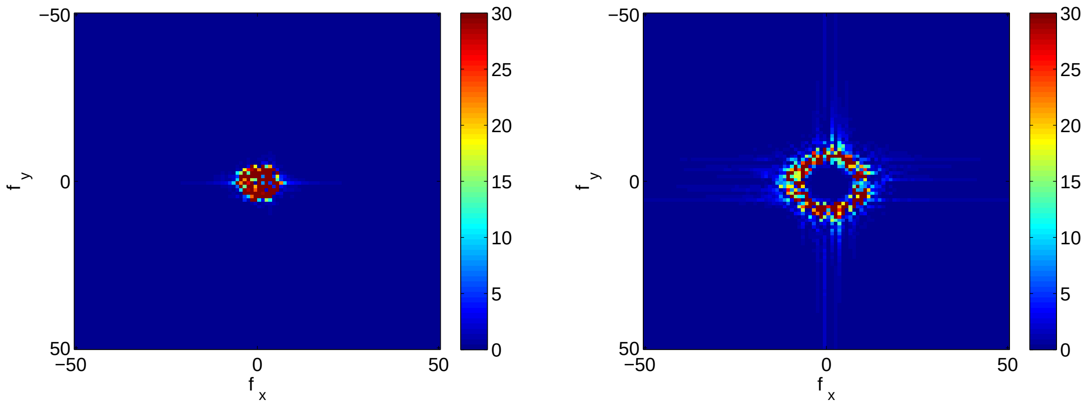

(a) Power Spectrum of v_{50} (b) Power Spectrum of v_{240}

Fig. 3.2: Power spectra of v_{50} and v_{240} when the noise level η is 0%, and $f = 5$ GHz.

achievable resolution.

3.4 Noise level versus the achievable resolution

In this section, we apply the above framework to the synthetic data sets in order to evaluate the effect of the noise level in an MWT imaging system. The synthetic data is collected from a target, which we refer to as the E-target (or, sometimes as Semenov's E-target.). This target, which is shown in Figure 3.1, has been previously used in other publications for resolution studies; e.g., in [38, 39]. Similar to [38], we assume that the E-target is lossless and has a relative permittivity of 2.3 within our frequency range of interest.

To generate the synthetic data set, we discretize the E-target into 150×150 cells within a 6.3×6.3 cm^2 domain. In all the examples concerning the inversion of this synthetic data set, the inversion domain is 7×7 cm^2 that is discretized into 100×100 cells.

Let's start by studying the role of noise in the achievable resolution at $f = 5$ GHz. In this section, we also assume that the number of transceivers are 16 equally spaced around a circle

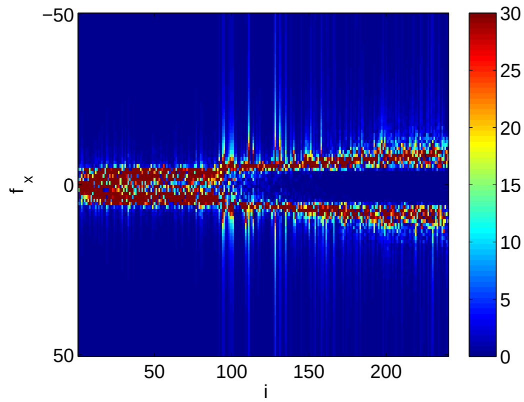

(a) $\eta = 0\%$

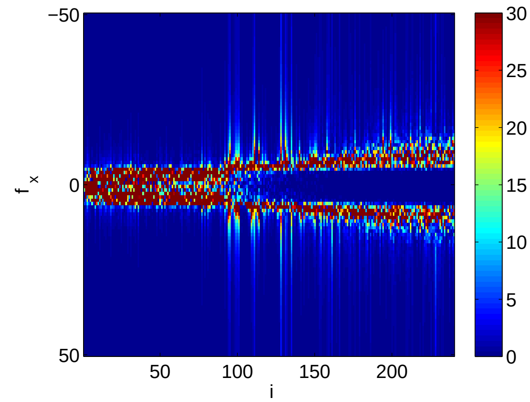

(b) $\eta = 3\%$

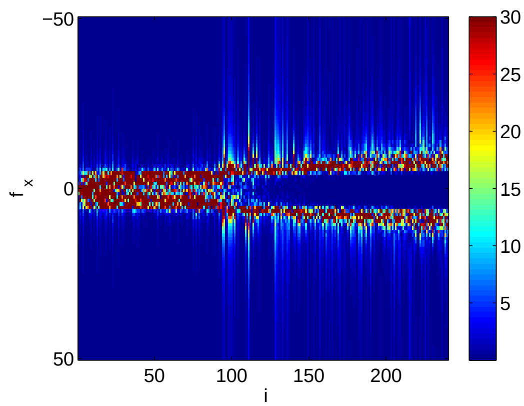

(c) $\eta = 10\%$

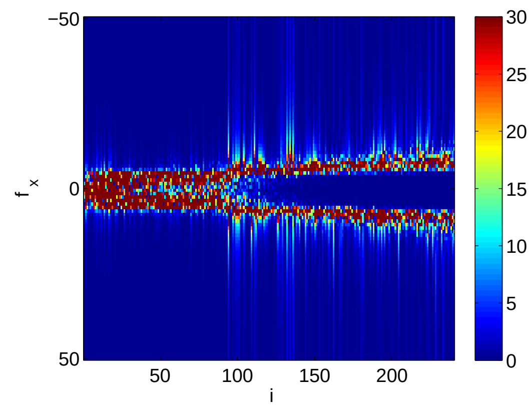

(d) $\eta = 20\%$

Fig. 3.3: Power spectrum plots: $|\tilde{v}_i(f_x, f_y = 0)|^2$ for i values and f_x indices at four different noise levels η. (Each column of the above images represents the power spectrum of a given v_i with respect to f_x.)

with the radius of 0.15 m; thus, having 16×15 scattering data points. (Unless otherwise stated, we assume that the transmitters are 2D line sources.) To study the effect of noise, we add synthetic noise to our data set based on the formula given in [46]. The addition of the noise based on this formula works as follows. Let's assume that the noiseless scattered field data at the receiving cites are stored in the vector $E^{\text{scat,noiseless}}$. Then, the noisy version of this vector, say $E^{\text{scat,noisy}}$ will be created as

$$E^{\text{scat,noisy}} = E^{\text{scat,noiseless}} + \max(E^{\text{scat,noiseless}}) \frac{\eta}{\sqrt{2}} (\vartheta_1 + j\vartheta_2) \tag{3.7}$$

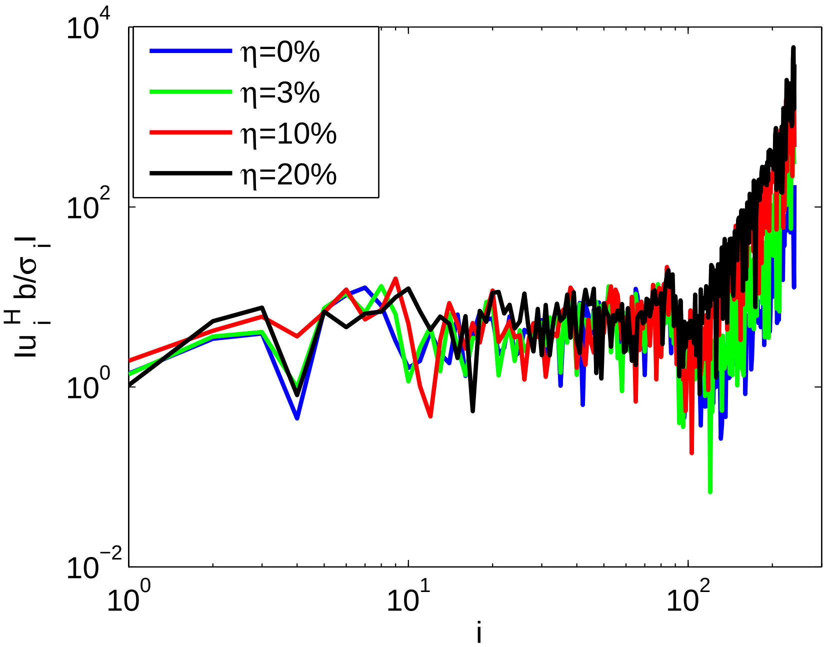

(a) $\frac{|u_i^H b|}{\sigma_i}$ versus i

Fig. 3.4: The variation of the magnitude of $u_i^H b/\sigma_i$ with respect to i when $f = 5$ GHz for four different noise levels η.

where ϑ_1 and ϑ_2 are two real vectors of appropriate size whose elements are uniformly distributed zero-mean random numbers between -1 and 1. The parameter η is then the noise level.

We now consider four different noise levels: $\eta = 0\%, 3\%, 10\%$, and 20%. Before starting our discussion on the effect of noise levels, it is instructive to plot the power spectrum $|\tilde{v}_i(f_x, f_y)|^2$ for two different i indices, $i = 50$ and $i = 240$, when $\eta = 0\%$. This has been shown in Figure 3.2. (Note that the zero spatial frequency is at the centre of this plot). As expected based on the discussion presented in Section 3.3.1, v_{240} exhibits more high spatial frequency contents than v_{50}. (It should be noted that the colorbars of these two plots, and also other plots regarding the Fourier transform has been truncated to a chosen maximum value to show the spatial frequency contents more clearly.) Now, let's take a look at one cut of this power spectrum that is created along the $f_y = 0$ axis. Herein, we focus on $|\tilde{v}_i(f_x, f_y = 0)|^2$. In Figure 3.3, we have plotted $|\tilde{v}_i(f_x, f_y = 0)|^2$ for $i = 1, \cdots, 240$ when the noise level takes 4 different values given above. (As can be seen, these plots look like a horizontal "V" letter as pointed out in Section 3.3.1.) The reason that we are plotting this power spectrum from $i = 1$ to $i = 240$ can be explained as follows. The number of discretized cells in this example is $n = 10^4$, and the number of measured data points is $m = 16 \times 15 = 240$. Based on (3.6), only $\min(m, n) = 240$ will matter in the reconstruction of the contrast profile. That's why the index i runs from 1 to 240 in Figure 3.3. As can be seen from each subfigure in Figure 3.3, as the index i increases, the spatial frequency contents of each right singular vector is generally increased as pointed out in Section 3.3.1. This can be seen by noting that as the index i increases, the "V" letter will flare out. Also, by comparing these four subfigures, it can be seen that the noise level of the measured data does not significantly affect the spatial frequency contents of the right singular vectors. This is, in fact, expected since v_is mainly depend on the Green's function of the background medium and the induced total field within the OI.

The above observation indicates that the right singular vectors corresponding to these four different data sets, which are distinguished by their noise levels, have similar spatial frequency contents. Therefore, if we were able to use all these right singular vectors in reconstructing the contrast profile, it would be expected that the achievable resolution by inverting these four different data sets will be similar. Now, the question to be answered is whether or not we can use all these spatial frequency contents in the reconstruction of χ. To answer this question we plot $|u_i^H b|/\sigma_i$, which are the coefficients of the summation (3.6). The plot of these coefficients versus the index i for the four different noise levels is shown in Figure 3.4 in the log-log format. As can be seen, as the noise level increases, these coefficients tend to blow up at smaller i indices. This indicates that as the noise level increases, less number of v_is can be incorporated into the reconstructed χ to avoid instability as described in

Section 3.3.2. Consequently, as the noise level increases, less high spatial frequency contents can be incorporated into the solution; thus, the achievable resolution will degrade as the noise level increases. The question that may arise here is why we observe blow-up even when the noise level is set to $\eta = 0\%$. This can be understood by noting that the numerical noise (e.g., round-off error) is always present in the scattered data when stored in the computer. That is, in any numerical implementations, we always have some noise in the data vector b. (That's why the use of regularization in inverting the data is needed even when $\eta = 0\%$.)

Now, let's take a look at the reconstruction of this target at these four different noise levels. (As noted in Section 3.1.2, we use the MR-GNI algorithm to invert the data sets.) The reconstructed permittivity profiles, denoted by $\epsilon_r^{\text{recons}}$, have been shown in the left column of Figure 3.5. (The reconstructed imaginary part of this lossless target is small; thus, it is not shown here.) As can be seen in the left column, as the noise level increases, the reconstruction accuracy will suffer. In this example, the three small fingers in the bottom left of the true object cannot be reconstructed at any of these noise levels. Therefore, the degradation of the image by the increased noise level is more visible in the quantitative accuracy of the reconstructed permittivity.

At this point, it is instructive to see what we could have reconstructed if we were able to use all the right singular vectors v_i in the reconstruction of the unknown profile. To this end, we minimize $||\epsilon_r^{\text{true}} - \alpha_i v_i||$ over the coefficients α_i for $i = 1, \cdots, \min(m, n)$ where ϵ_r^{true} is the true profile of the OI. Once α_is are obtained, we will have the direct expansion of our permittivity profile, denoted by $\epsilon_r^{\forall v_i}$, in terms of all the right singular vectors. That is,

$$\epsilon_r^{\forall v_i} = \sum_{i=1}^{\min(m,n)} \alpha_i v_i = \sum_{i=1}^{\min(m,n)} (v_i^H \epsilon_r^{\text{true}}) v_i. \tag{3.8}$$

The direct expansion of the reconstructed permittivity using (3.8) is shown in the right column of Figure 3.5 for different noise levels. As opposed to the reconstruction results shown in the left column of Figure 3.5, all the permittivity profiles shown in the right column have resolved the three small fingers in the left bottom of the OI. (Note that the discretization of ϵ_r^{true} used in the above equation is different than the one used to create the synthetic scattered data set so as to avoid the so-called inverse crime.)

The above observation is very important. It shows that in the example considered here, the noise level is the main reason for not being able to resolve the three small fingers in the OI. This is due to the fact that the presence of noise limits the number of v_is that can be used in the expansion of the unknown profile. In other words, the presence of noise limits the dimension of the space into which the unknown profile is projected.

We have now presented our mathematical framework for resolution analysis. Using this framework, we have shown the importance of the signal-to-noise ratio in the achievable resolution. In the next Chapter, we use this framework to investigate some important antenna parameters that affects the achievable resolution from MWT. Finally, as mentioned in Section 2.7.3, several parameters, in addition to the measurement noise, contribute to the overall noise of the system. In Chapter 6, two of such contributing factors that are related to the antenna element used in MWT will be discussed.

3.5 Quantitative accuracy

This chapter presented a mathematical framework for resolution analysis as it was based on the spatial frequencies of the right singular vectors. From our numerical experience with MWT nonlinear inversion algorithms, the better the achievable resolution is, the better the quantitative accuracy is. Based on this framework, this can be speculated as follows. Better resolution means incorporation of more right singular vectors in the reconstructed dielectric profile. Having the opportunity to reconstruct the dielectric profile using more right singular vectors can result in enhanced quantitative accuracy.

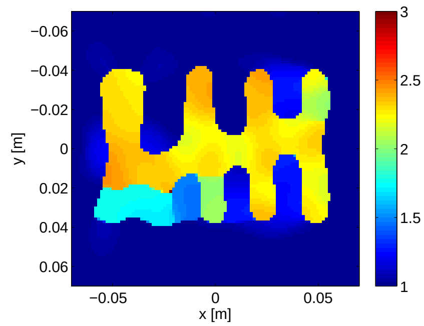

(a) $Re(\epsilon_r^{\text{recons}})$, $\eta = 0\%$

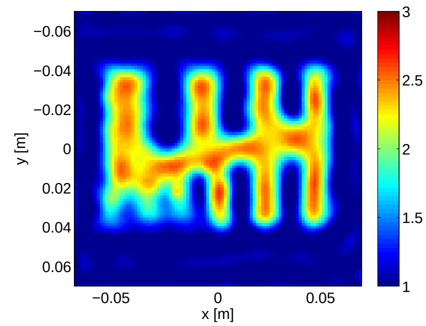

(b) $Re(\epsilon_r^{\forall v_i})$, $\eta = 0\%$

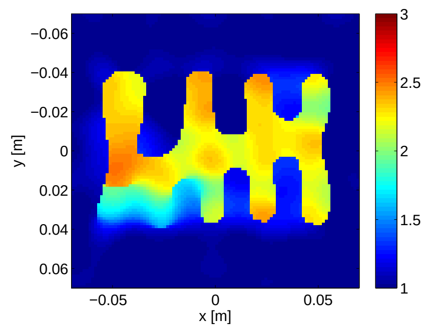

(c) $Re(\epsilon_r^{\text{recons}})$, $\eta = 3\%$

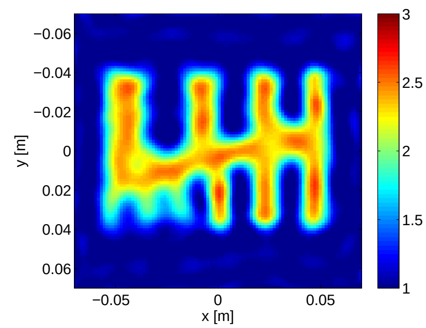

(d) $Re(\epsilon_r^{\forall v_i})$, $\eta = 3\%$

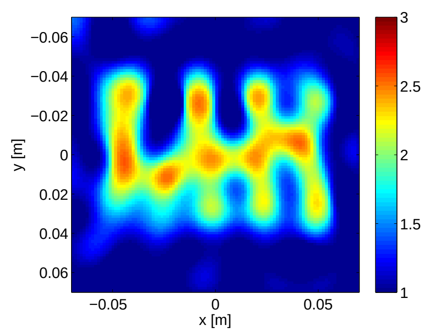

(e) $Re(\epsilon_r^{\text{recons}})$, $\eta = 10\%$

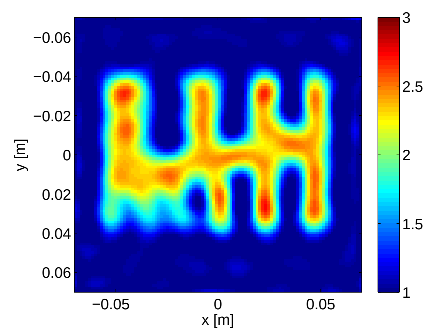

(f) $Re(\epsilon_r^{\forall v_i})$, $\eta = 10\%$

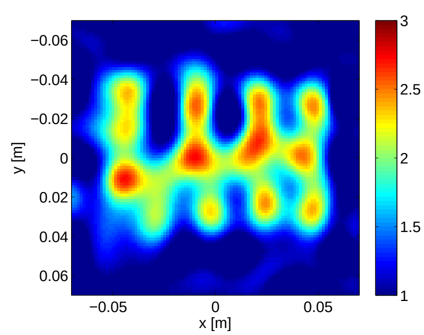

(g) $Re(\epsilon_r^{\text{recons}})$, $\eta = 20\%$

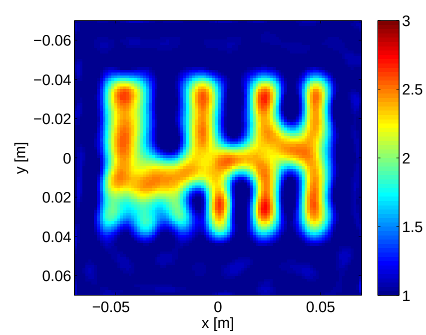

(h) $Re(\epsilon_r^{\forall v_i})$, $\eta = 20\%$

Fig. 3.5: Left column: The reconstructed permittivity, denoted by $\epsilon_r^{\text{recons}}$, of the E-target when irradiated by 16 antennas at 5 GHz at different noise levels η. Right column: Direct expansion of the true E-target permittivity profile, denoted by $\epsilon_r^{\forall v_i}$, using all the right singular vectors v_i when irradiated by 16 antennas at 5 GHz at different noise levels.

4

Antenna Specifications

In this chapter, some of the desired antenna specifications for MWT so as to achieve enhanced resolution will be discussed in more details using both synthetic and experimental data sets. The effect of these antenna specifications on the achievable resolution and accuracy from MWT will be evaluated by the mathematical framework that was proposed in Chapter 3.[1]

The role of the antenna incident field distribution in the achievable accuracy and resolution from MWT will be first evaluated. It will be shown that the use of a focused incident field distribution can enhance the image accuracy and resolution. This is a novel method for increasing the achievable resolution and accuracy. (How to achieve a focused incident field

[1] This chapter is based on the following three publications: (1) N. Bayat and P. Mojabi, "A Mathematical Framework to Analyze the Achievable Resolution From Microwave Tomography," Submitted in 2014, (2) N. Bayat and P. Mojabi, "The Effect of Antenna Incident Field Distribution on Microwave Tomography Reconstruction," *Progress In Electromagnetics Research*, vol. 145, 153-161, 2014, and (3) N. Bayat and P. Mojabi, "On the Effect of Antenna Illumination Patterns on the Accuracy and Resolution of Microwave Tomography," *IEEE International Symposium on Antennas and Propagation and USNC-URSI Radio Science Meeting*, Orlando, Florida, July 2013.

distribution will be the topic of Chapters 5 and 6.) We then study the effect of the frequency of operation as well as the simultaneous use of different frequencies of operation on the achievable image accuracy and resolution. The effect of increasing the sampling resolution (number of transceivers) in the MWT imaging system will also be evaluated. Based on these investigations, we justify the need to have an antenna element that has a focused near-field distribution while being small and multi-band (or, wide-band). We then discuss the implementation of such radiator in more details in Chapters 5 and 6.

4.1 Antenna incident field evaluation

In this section, we focus on the role of the antenna incident field distribution on the achievable image accuracy and resolution from MWT. This will be evaluated by the mathematical framework that has been presented in Chapter 3. As noted in Chapter 2, the achievable image accuracy can be affected by changing the incident field distribution within the imaging domain. Note that we use the term "incident field distribution" as opposed to "radiation pattern" since in most practical MWT systems, antenna elements work in their near-field zones. Therefore, the radiation pattern, which is a far-field quantity, is not appropriate to be used herein. Also, as opposed to far-field pattern which is independent of the distance from the antenna, the near fields of antennas vary with respect to the distance from the antenna. Therefore, the term "distribution" will be more appropriate to be used here than the term "pattern".

To start our discussion, let's present a numerical model for our 2D transverse magnetic (TM_z) problem that can represent a focused incident field distribution. To this end, we

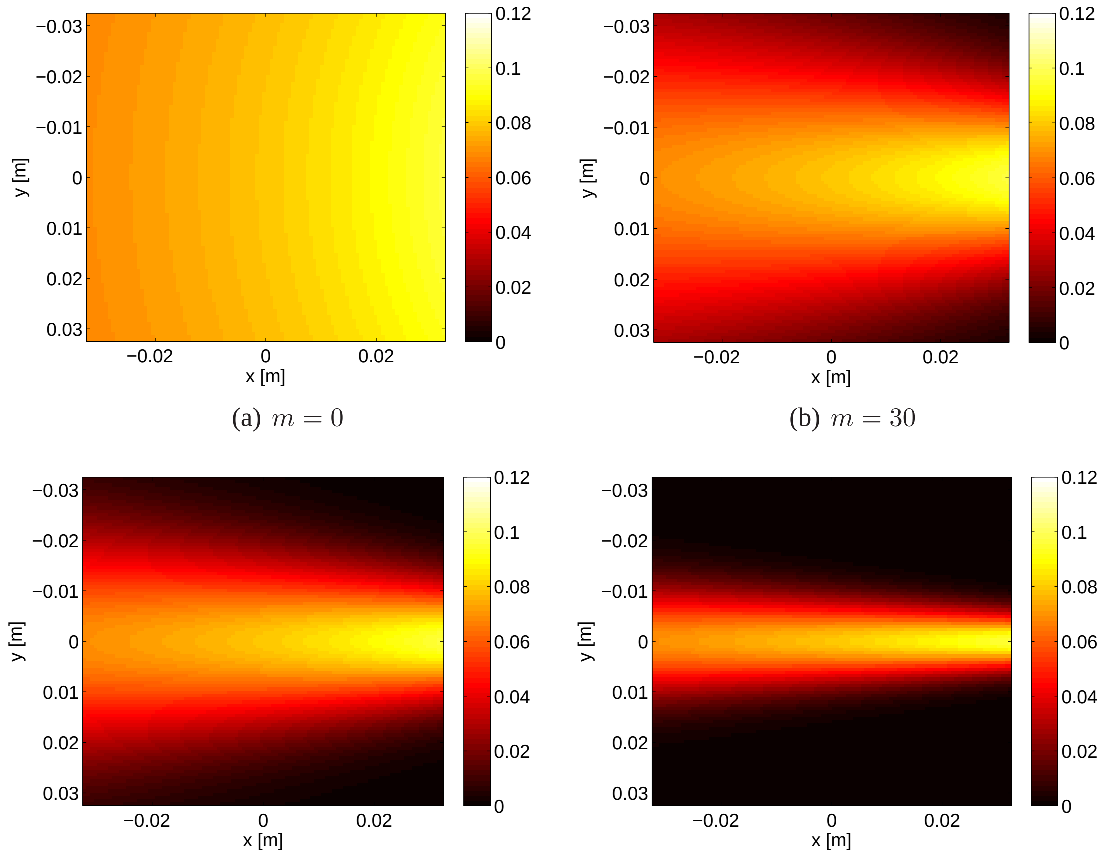

(a) $m = 0$

(b) $m = 30$

(c) $m = 70$

(d) $m = 300$

Fig. 4.1: Incident field distribution in the imaging domain $\mathcal{D}$; (a) $m = 0$, (b) $m = 30$, (c) $m = 70$, and (d) $m = 300$. The size of the imaging domain is 0.064×0.064 m^2, and the antenna is located at $(x, y) = (0.1, 0)$ m. The origin of the coordinate is located at the center of the imaging domain.

consider the following model for the incident field distribution [2]

$$\boldsymbol{E}^{\text{inc}}(x, y) = \hat{z} C H_0^2(k_b \rho) \cos^m \psi \tag{4.1}$$

where C is a constant, (x, y) is the observation point within the imaging domain, and $H_0^2(.)$ is the zeroth-order Hankel function of the second kind. The distance from the transmitting antenna to the observation point is denoted by ρ. The angle ψ is the angle between the antenna boresight axis and the line connecting the antenna to the observation point as shown in Figure 2.1. The non-negative variable m represents the focusing level of the incident field distribution: the larger m, the more focused the incident field distribution. Also, as can be seen in (4.1), $m = 0$ represents an omni-directional incident field distribution (i.e., the incident field due to a line source). We note that the term “focusing level” is different from the term “directivity”. This is due to the fact that the directivity of an antenna is a far-field property of an antenna. However, as noted above, most MWT antenna elements work in their near-field zones. Therefore, herein, we use the term “focusing level” of the incident field distribution, and not the “directivity”. To better understand the effect of the parameter m in our numerical incident field model, we have demonstrated the incident field distribution for four different different m values in Figure 4.1.

4.1.1 Use of focused incident field distribution

In our recent work [18], we have shown that the use of a focused incident field distribution to illuminate the OI can enhance the achievable resolution. In this subsection, we apply our proposed mathematical framework for resolution analysis to this idea so as to justify the use of a focused incident field distribution.

[2] A similar incident field model for calibration of the MWT data has been used in [47].

To start our discussion, we consider the OI shown in Figure 3.1. Let's assume that we use 32 transceivers to collect the scattering data set.[3] Herein, we consider single-frequency inversion at 5 GHz when the noise level is set to 3%. Therefore, the dielectric profile of the OI is to be reconstructed using 32×31 data points. The power spectrum plots for two different focusing levels, namely $m = 0$ and $m = 1000$, are shown in Figure 4.2. (Let's recall that $m = 0$ corresponds to having an omnidirectional illumination.) As can be seen the spatial frequency contents for these two cases are very similar. Now, let's take a look at the variation of the $|u_i^H b|/\sigma_i$ to understand how many right singular vectors can be used in contrast reconstruction in each case. This has been shown in Figure 4.3. As can be seen the coefficients $|u_i^H b|/\sigma_i$ blow up later when $m = 1000$ as compared to the case when $m = 0$. This indicates that with the increased focusing level, we are now able to utilize more right singular vectors to reconstruct the unknown contrast. This should now shows itself in the reconstructed permittivity using two different focusing levels, shown in Figure 4.4. As can be seen, the three small fingers in the bottom left of the profile is visible when $m = 1000$; but, it is not visible when $m = 0$. It is now instructive to see $\epsilon_r^{\forall v_i}$ for these two different focusing levels. ($\epsilon_r^{\forall v_i}$ has been discribed in Section 3.4.) This is shown in Figure 4.5. As expected, $\epsilon_r^{\forall v_i}$ for these two different focusing levels are very similar, and can resolve the three small fingers in the bottom left of the target. This is due to the fact that the spatial frequency contents for these two focusing levels, see Figure 4.2, are very similar, and we are using all the right singular vectors in forming $\epsilon_r^{\forall v_i}$.

From this example, it can be understood that the main reason behind achieving better reconstruction with the focused incident field distribution lies in the fact that we can use more right singular vectors for reconstructing the unknown profile. As noted above this is mainly due to the fact that $|u_i^H b|/\sigma_i$ coefficients tend to blow up later for the focused incident field

[3] Note that the use of 32 transceivers indicates that we have 32 antenna elements in the MWT system. When one transmits, the rest receive, thus, having 32×31 data points.

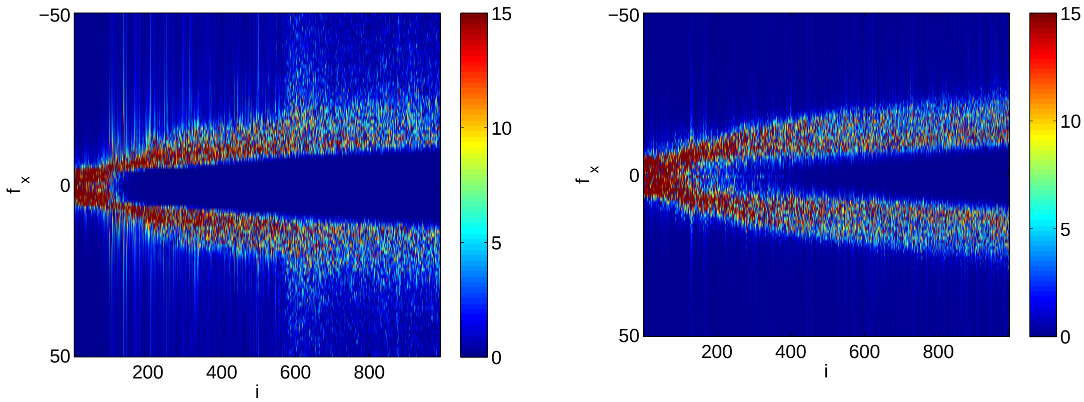

(a) $m = 0$ (b) $m = 1000$

Fig. 4.2: Power spectrum plots: $|\tilde{v}_i(f_x, f_y = 0)|^2$ for i values and f_x indices at 5 GHz when the number of transceivers is 32, and the noise level is $\eta = 3\%$ at two different incident field focusing levels. [Left] focusing level of $m = 0$ (omnidirectional illumination), and [Right] focusing level of $m = 1000$.

distribution.

To demonstrate the usefulness of the use of focused incident field distribution for MWT, we consider five more test cases. For each of these test cases, we collect several scattering data sets, each of which corresponds to utilizing an incident field distribution with a certain focusing level. (3% white noise is added to all data sets according to [46].) Each of these data sets will then be separately inverted. The utilized incident field distribution in the inversion algorithm will be the same incident field distribution that has been used to collect that scattering data set.

Let's now consider a standard resolution test case. We consider two lossless circular objects with the radius of 20.5 mm and the relative permittivity of $\epsilon_r = 4$ at the frequency of operation $f = 3$ GHz which are separated by 15 mm, as shown in Figure 4.6(a). In the first configuration, this target will be successively illuminated by 8 antennas equally distributed on a circle of radius 0.1 m. (Total number of data points will then be 8×7 data points; due to reciprocity, half of which will be redundant.) For this configuration, we collect three

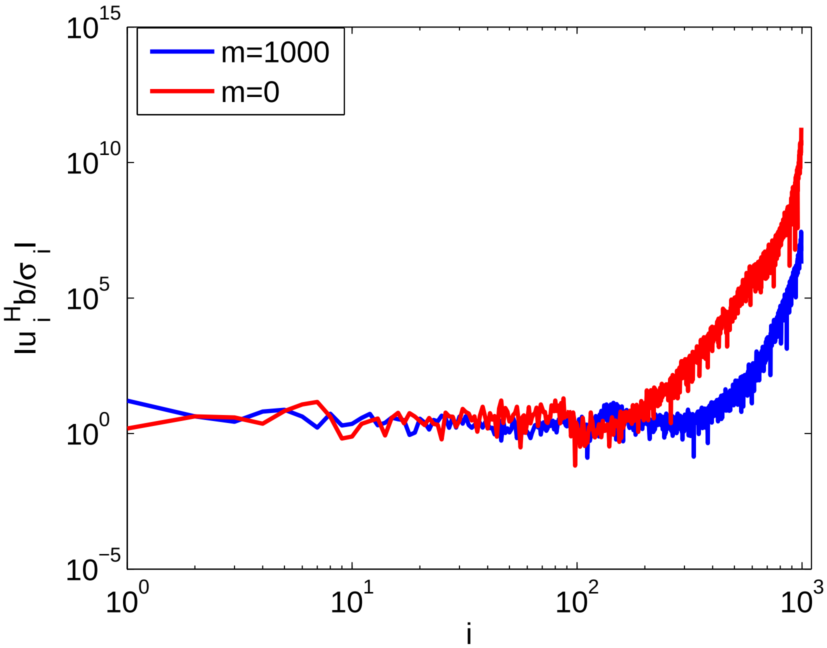

Fig. 4.3: The variation of the magnitude of $u_i^H b/\sigma_i$ at 5 GHz by 32 transceivers and at the noise level is 3% for two different scenarios: when the OI is illuminated by the incident field distribution having the focusing level of [Red] $m = 0$ (omnidirectional distribution), and [Blue] $m = 1000$.

different data sets, each of which corresponds to using a certain focusing level for the utilized incident field distribution; namely, $m = 0, 30, 70$. The inversion results for this configuration are shown in Figure 4.6(b)-(d). It can be seen that (*i*) these inversion results are different, and (*ii*) the reconstructed permittivity is more accurate and exhibit enhanced resolution when $m = 70$. In the second configuration, we repeat the previous experiment while having 24 antennas; thus, having 24×23 data points. The reconstruction results corresponding to the two extreme cases ($m = 0, 70$) are shown in Figure 4.7. This example clearly shows that the use of different incident field distributions can result in images with different accuracies.

As noted earlier, we associate this improved performance due to the use of more right singular vectors in the reconstruction of the unknown dielectric profile. It is also instructive to

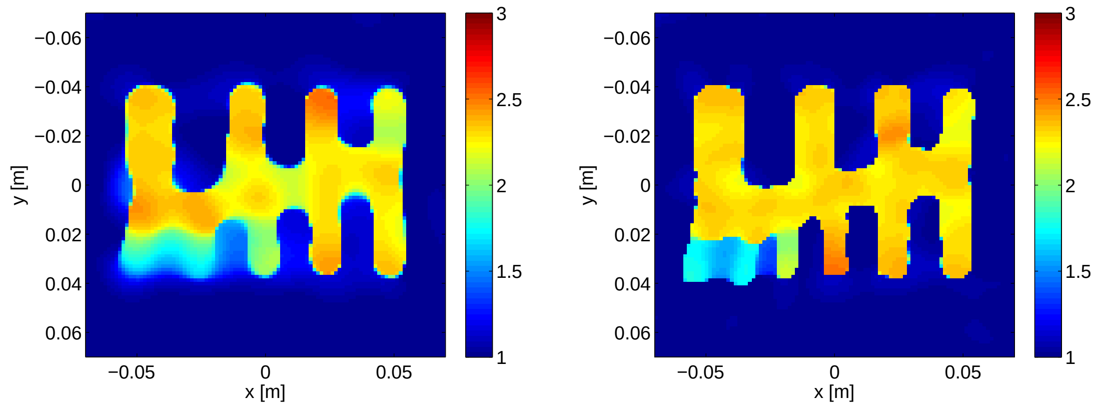

(a) $Re(\epsilon_r^{\text{recons}})$, $m = 0$

(b) $Re(\epsilon_r^{\text{recons}})$, $m = 1000$

Fig. 4.4: The reconstructed real-part of the permittivity, $Re(\epsilon_r^{\text{recons}})$, of the E-target when irradiated by 32 transceivers at 5 GHz, and the noise level of 3%: [Left] when the focusing level is $m = 0$, and [Right] when the focusing level is $m = 1000$.

compare the singular values of the Jacobian (sensitivity)[4] matrix for different values of m at the last iteration of the MR-GNI algorithm as shown in Figure 4.8: the singular values corresponding to $m = 70$ are larger than those corresponding to smaller m values. This indicates that the last iteration of the inversion algorithm deals with a less ill-posed problem when $m = 70$, thus, facilitating the flow of information from the imaging domain to the measurement domain.

We have also tried this example when the transmitters are located on a circle of radius 1 m (i.e., 10λ at the frequency of operation). In this configuration, the reconstruction results for these different m values were almost identical. Noting that the imaging domain in this configuration is located in the far-field zone of the transmitting antennas, these different m values do not significantly change the incident field distribution within the imaging domain; thus, resulting in no considerable changes in the reconstruction results.

[4] The Jacobian (sensitivity) matrix, often denoted by $\boldsymbol{J}$, represents the sensitivity of the scattered data with respect to the contrast value at different locations within the imaging domain. That is, the sensitivity matrix represents $\partial E^{\text{scat}}/\partial \chi$. The number of rows of this matrix is equal to the number of data points. The number of columns of this matrix is equal to the number of discretized cells within the imaging domain.

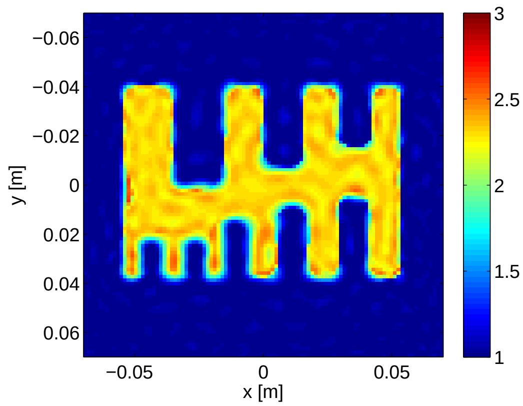

(a) $Re(\epsilon_r^{\forall i}), m = 0$

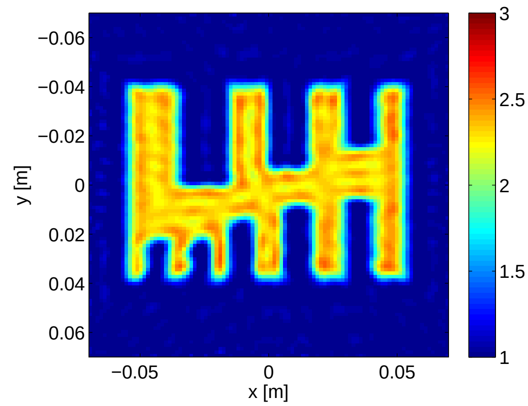

(b) $Re(\epsilon_r^{\forall i}), m = 1000$

Fig. 4.5: Direct expansion of the true E-target permittivity profile, $\epsilon_r^{\forall v_i}$, using all the right singular vectors v_i when irradiated by 32 antennas at 5 GHz and at the noise level of $\eta = 3\%$. [Left] when the focusing level is $m = 0$, and [Right] when the focusing level is $m = 1000$.

Now, let's again consider the Semenov's E-target, shown in Figure 3.1. For convenience, the real part of the permittivity of this target is also shown in Figure 4.9(a). This object, which is lossless and has a relative permittivity of 2.3, is illuminated by 16 antennas (thus, having 16×15 data points), located on a circle with the radius of 0.15 m with three different focusing levels: $m = 0$, 70, and 300. We then use the binary implementation of the MR-GNI algorithm [48] to invert these data sets. (A brief description about the binary MR-GNI algorithm is given in Appendix C.) As shown in Figure 4.12(b)-(c), the reconstruction results for $m = 0$ and $m = 70$ are not capable of reconstructing the three small fingers located at the bottom left part of the object. However, with $m = 300$, the inversion algorithm is capable of capturing these three fingers. The singular values of the Jacobian (sensitivity) matrix in the last iteration of the inversion algorithm for different m values are shown in Figure 4.11(a). As can be seen, the singular values corresponding to $m = 300$ decay more slowly as compared to those for $m = 0$ and 70. That is, the mathematical formulation corresponding to $m = 300$ is less ill-posed as compared to the mathematical formulations of $m = 0$ and 70.

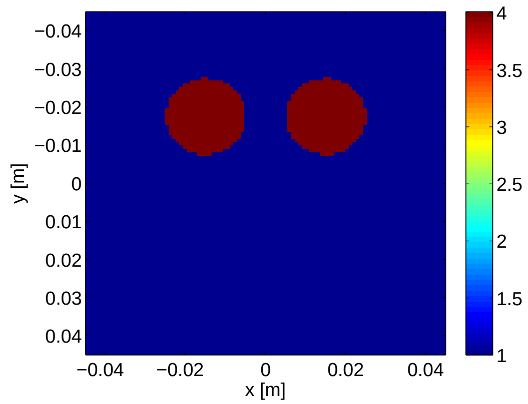

(a) True $Re(\epsilon_r)$

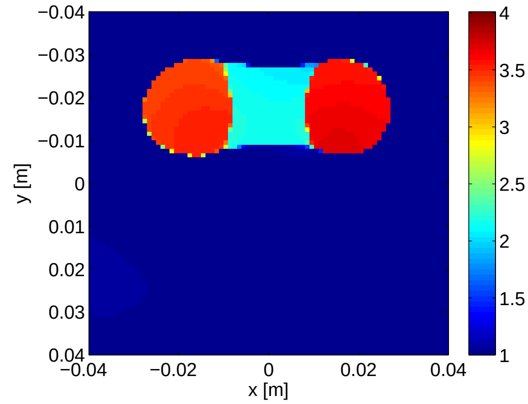

(b) $Re(\epsilon_r)$, $m = 0$

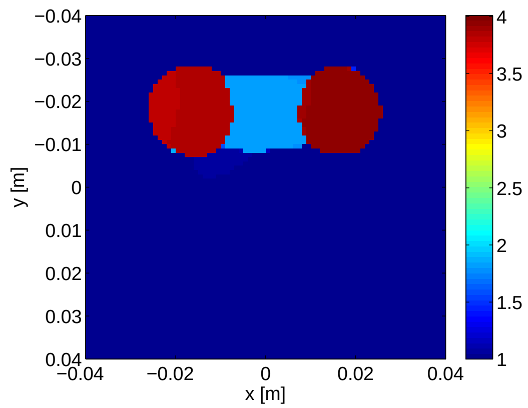

(c) $Re(\epsilon_r)$, $m = 30$

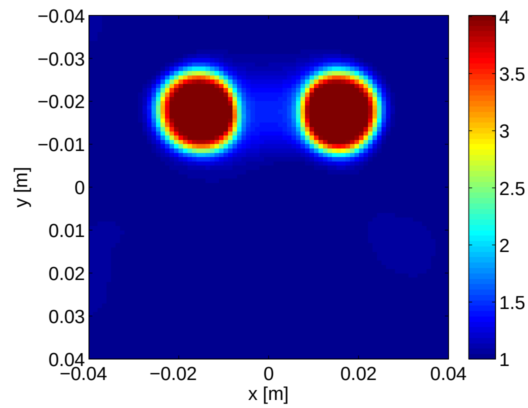

(d) $Re(\epsilon_r)$, $m = 70$

Fig. 4.6: Resolution test using 8 antennas: (a) true dielectric profile (The zero imaginary part of the permittivity is not shown.); (b)-(d) reconstructed dielectric profile using three different focusing levels (m) for the utilized incident field distribution. Reproduced courtesy of The Electromagnetics Academy.

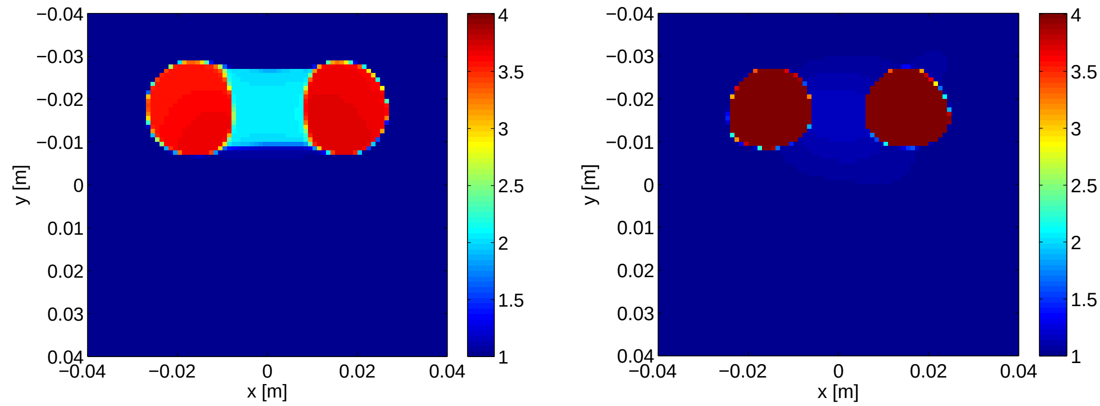

(a) $Re(\epsilon_r)$, $m = 0$ (b) $Re(\epsilon_r)$, $m = 70$

Fig. 4.7: Resolution test using 24 antennas: reconstructed dielectric profile using two different focusing levels for the utilized incident field distribution. Reproduced courtesy of The Electromagnetics Academy.

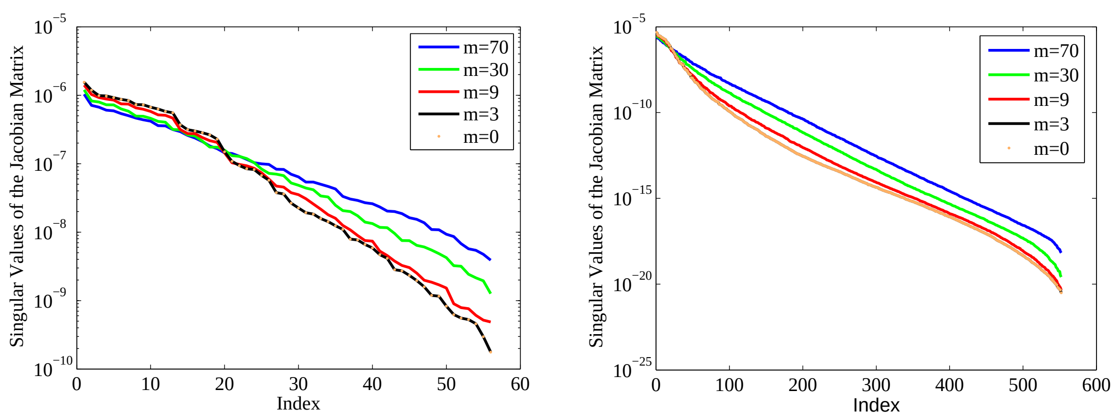

(a) 8 antennas (b) 24 antennas

Fig. 4.8: Resolution test using 8 and 24 antennas: singular values of the Jacobian matrix at the last MR-GNI iteration for different m values. Reproduced courtesy of The Electromagnetics Academy.

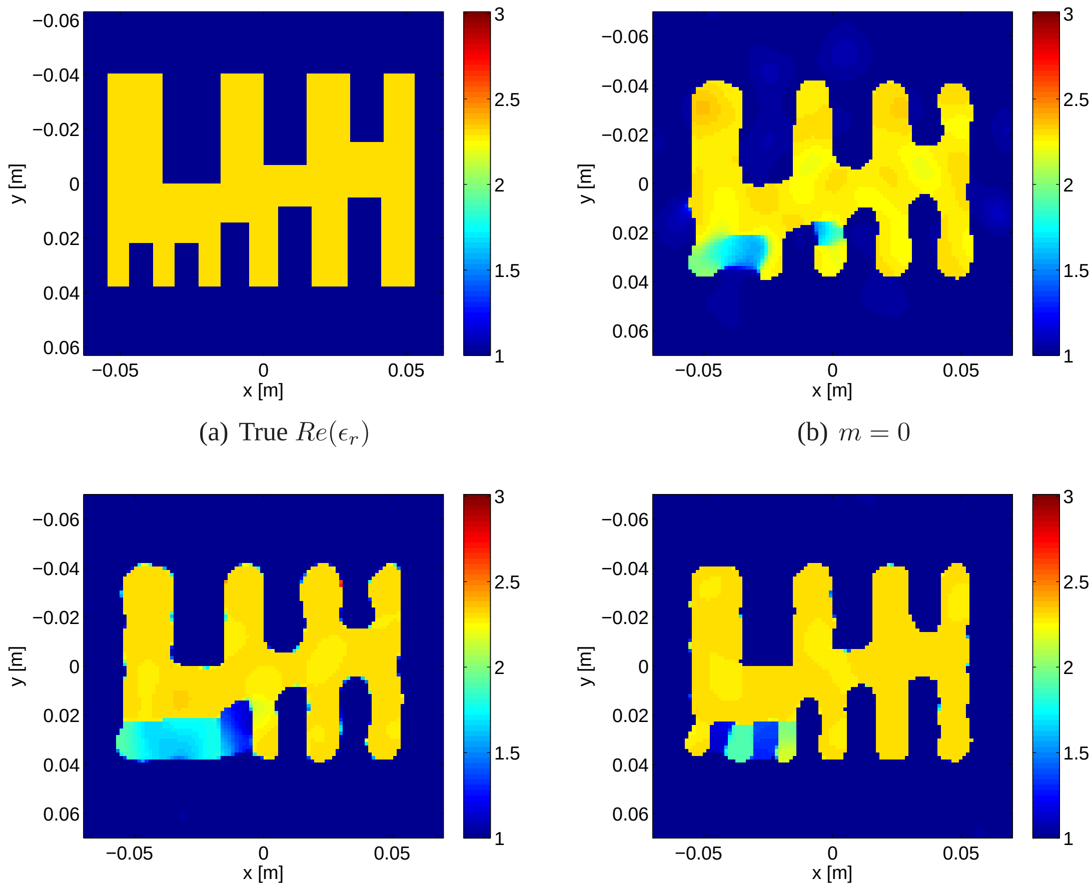

(a) True $Re(\epsilon_r)$

(b) $m = 0$

(c) $m = 70$

(d) $m = 300$

Fig. 4.9: Semenov's E-shape object using 16 antennas: (a) true dielectric profile; reconstructed dielectric profile using binary inversion when (b) $m = 0$, (c) $m = 70$, and (d) $m = 300$. Reproduced courtesy of The Electromagnetics Academy.

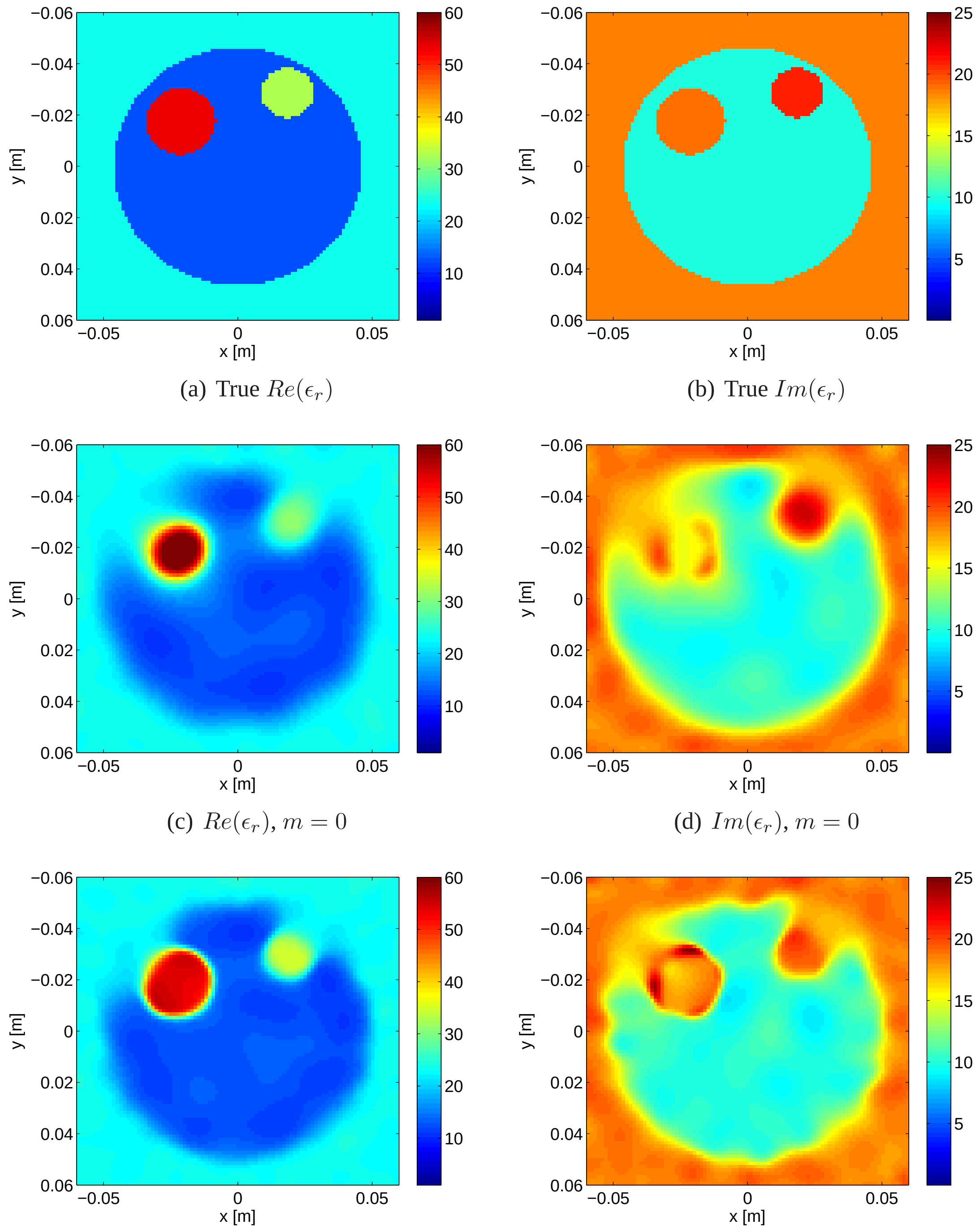

(a) True $Re(\epsilon_r)$ (b) True $Im(\epsilon_r)$

(c) $Re(\epsilon_r)$, $m = 0$ (d) $Im(\epsilon_r)$, $m = 0$

(e) $Re(\epsilon_r)$, $m = 70$ (f) $Im(\epsilon_r)$, $m = 70$

Fig. 4.10: Breast test case using 24 antennas: (a)-(b) true dielectric profile; reconstructed dielectric profile when (c)-(d) $m = 0$, and (e)-(f) $m = 70$. R reproduced courtesy of The Electromagnetics Academy.

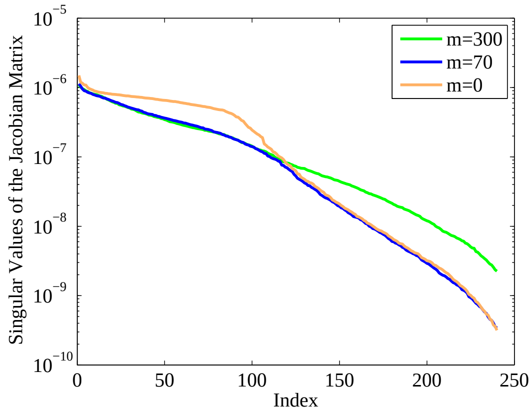

(a) E-shape object

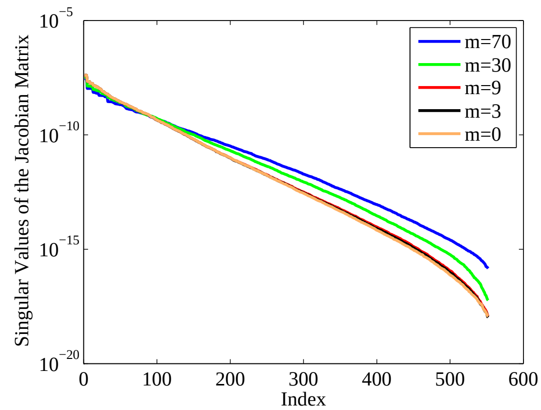

(b) Breast model

Fig. 4.11: Singular values of the Jacobian matrix at the last MR-GNI iteration for different m values for the E-shape object and breast model. Reproduced courtesy of The Electromagnetics Academy.

As the third test case, we use a breast model that has been previously used in [11], [21]. As shown in Figure 4.10(a)-(b), this model consists of three regions: fibroglandular (smallest circle), tumor (medium circle), and fatty (largest circle) tissues. The background medium is chosen to be $23.4 + j18.5$ at the frequency of operation, which is 1 GHz (similar to the background medium used for the breast cancer microwave imaging system at Dartmouth College [11]). This numerical model is illuminated by 24 antennas, which are located on a circle of radius 0.1 m. The inversion results for $m = 0, 70$ are shown in Figure 4.10(c)-(f). As can be seen, the reconstructed image when $m = 70$ is more accurate than the reconstructed image when $m = 0$. Specifically, the true tumor permittivity is $53.4 + j18.8$, whereas the reconstructed tumor permittivity at the center of inclusion is $63.4 + j15.4$ when $m = 0$, and is $53.7 + j17.7$ when $m = 70$. As shown in Figure 4.11(b), the singular values of the Jacobian matrix at the last MR-GNI iteration when $m = 70$ are larger than those when $m = 0$. We also attempted to reconstruct this profile using only 4 antennas; however, reconstruction was not successful for any m values that we tried. When using 4 antennas, we noticed that the singular values of the Jacobian (sensitivity) matrix at the last

MR-GNI iteration when $m = 0$ were larger than those when $m = 70$. This observation is not consistent with what we observed in earlier examples. This inconsistency might be justified as follows. If only 4 antennas with focused near-field distribution ($m = 70$) are used, we cannot sufficiently illuminate every part within the imaging domain, thus, losing sensitivity to some imaging areas. On the other hand, if 4 antennas with omnidirectional field distribution ($m = 0$) are used, it is more likely to illuminate everywhere within the imaging domain sufficiently, thus, enhancing the sensitivity compared to the use of few focused beams.

In the fourth test case, we consider two lossy concentric squares at the frequency of operation $f = 5$ GHz as shown in Figure 4.12(a)-(b). First, we illuminated this target by 8 antennas (thus, having 8×7 data points), located on a circle with the radius of 0.1 m with different focusing levels starting from $m = 0$ to 70. Using this number of antennas, we were not able to reconstruct this target using any focusing values. We then repeated the same numerical experiment using 32 antennas. In this case, as shown in Figure 4.12(c)-(f), the reconstruction results for $m = 0$ and $m = 70$ (and also, $m = 3, 9, 30$, which are not shown here) are almost identical. The singular values of the Jacobian matrix in the last iteration of the MR-GNI algorithm for different m values are shown in Figure 4.13. As can be seen, the singular values corresponding to $m = 70$ are still larger than those corresponding to $m = 0$. However, it seems that the number of significant singular values for $m = 0$ is sufficient to reconstruct this target successfully.

Finally, we present the reconstruction of the E-target by considering noiseless data sets. Using this example, we can prove that the improvements observed by the use of focused incident field distribution is not related to the way that the noise is added to the scattered data. To this end, we collect noiseless data set (setting $\eta = 0$) from this target with three different focusing levels for the utilized incident field; namely, $m = 0$, $m = 70$, and $m = 300$.

These data sets are then inverted using the binary MR-GNI algorithm. The true profile as well as the reconstructed profiles are shown in Figure 4.14. As can be seen, the inversion of noiseless data corresponding to $m = 300$ can reconstruct the three fingers of the object in its left bottom part. Comparing these inversion results, as shown in Figure 4.14, with the reconstruction of the same target but with noisy data as shown in Figure 4.9 shows that this improvement is due to the utilized incident field, not due to any possible unfair noise contribution.

4.2 Frequency of operation

In this section, we consider the effect of the frequency of operation on the achievable resolution. We note that the frequency(ies) of operation is (are) determined by the antenna element used in a given MWT system. Herein, we also consider the E-target, and assume that this OI is irradiated by 16 transceivers, and the scattered data has a noise level of $\eta = 3\%$. In this section, we only vary the frequency f at which the OI is irradiated. The frequency is changed from 500 MHz to 5 GHz. Let's first take a look at the power spectra $|\tilde{v}_i(f_x, f_y = 0)|^2$ that are shown in Figure 4.15. As can be seen in each of the subfigure, as the index i increases, the amount of high spatial frequency contents within v_i is generally increased in the form of a horizontal "V" letter. Now, let's consider how many of these right singular vectors can be used in the reconstruction of the unknown profile. This can be understood by plotting the coefficients $|u_i^H b|/\sigma_i$ versus the index i. As can be seen in Figure 4.16, as the frequency increases, these coefficients tend to blow up at a larger index i. That means as the frequency of operation increases, the reconstructed profile has the chance to lie within a space of v_is having a larger dimension, thus, having the chance to resolve more features.

The reconstruction results at these six different frequencies are shown in Figure 4.17. As can be seen as the frequency increases, we have better reconstruction. This is consistent with our observation regarding the ability to incorporate more right singular vectors into the expansion of the reconstructed contrast as the frequency of operation increases (see Figure 4.16.). Now, let's consider what we could have achieved if we were able to use all the right singular vectors at each of these frequencies of operation. That is, we'd like to address what $\epsilon_r^{\forall i}$ would be for each of these six frequencies of operation. This has been shown in Figure 4.18. As can be seen, for each frequency, $\epsilon_r^{\forall i}$ is better than its corresponding $\epsilon_r^{\text{recons}}$. This is, of course, due to the fact that the reconstructed permittivity profile, $\epsilon_r^{\text{recons}}$, cannot utilize all the right singular vectors in its expansion whereas we have used all the right singular vectors to create $\epsilon_r^{\forall v_i}$.

We now know that $\epsilon_r^{\text{recons}}$ degrades as the frequency of operation decreases since less right singular vectors can be used in reconstructing the permittivity as the frequency of operation decreases so as to avoid the instability issue. Use of less right singular vectors will then indicate that the reconstructed permittivity has less high spatial frequency components, thus, suffering from resolving small features. The question that may now arise is why $\epsilon_r^{\forall i}$ degrades as we decrease the frequency of operation. (Note that we use all the right singular vectors in creating $\epsilon_r^{\forall i}$.) Specifically, as can be seen in Figure 4.18, the three small fingers in the bottom left of the OI are only visible in $\epsilon_r^{\forall i}$ at 5 GHz, and not in the rest of frequencies. Currently, we are only able to speculate on the reason for such behavior. Our speculation is based on the point mentioned in [40] that revolves around the idea that as the singular values becomes smaller and smaller, (specifically, when they reach machine precision level) the calculation of their corresponding right singular vectors becomes less and less accurate. To understand this, let's take a look at the singular values corresponding to these six frequencies as shown in Figure 4.19. As can be seen, the singular values becomes more rapidly smaller as the frequency of operation decreases. In other words, the singular values corresponding to smaller frequencies of operation tend to go to the machine precision level more rapidly than those corresponding to higher frequencies of operation.Therefore, the accuracy of the high-order right singular vectors decreases as the frequency decreases. Consequently, as the frequency decreases, the profile $\epsilon_r^{\forall i}$ is projected into a space whose high spatial frequency basis vectors (i.e., v_is with large i indices) are less accurate as compared to those for higher frequencies of operation. Therefore, the resolution in lower frequencies will suffer even when we use all the right singular vectors in forming $\epsilon_r^{\forall i}$. Now, if we take another look at Figure 4.18, we will observe that all the six subfigures represent similar low-spatial variations. However, they are mainly the high spatial variations (the existence of the three small fingers) that are not resolved in the lower frequencies of operation. This indicates the absence of sufficiently accurate v_is with large i indices in the $\epsilon_r^{\forall i}$ when the frequency of operation is low.

Based on the above discussion, it can be concluded that the main reason behind achieving lower resolution with lower frequencies of operation is the noise level of the measured data. That is, for a fixed noise level, say $\eta = 3\%$, we can incorporate more right singular vectors in reconstructing the permittivity profile when working at a higher frequency of operation. Now, if it is assumed that there is no noise in the measured data, it might be speculated that the same resolution can be achieved with lower frequencies of operation. (This has also been indicated in [39].) It is also worthwhile to note that three factors contribute toward the overall noise in MWT: modeling error as defined in [21], measurement noise, and numerical noise. Therefore, even if we could achieve perfect modeling and noiseless measurements, we would still have numerical noise, which as discussed in the previous paragraph, will deteriorate low-frequency reconstruction more than high-frequency reconstruction. Due to the presence of the numerical noise, it is not therefore possible to investigate if we can achieve the same resolution with lower frequencies of operation even when we use a noiseless synthetic data set with no modeling error.

We have also tried reconstructing this OI at three other higher frequencies of operation:

6 GHz, 7 GHz and 8 GHz. But, the inversion algorithm was not capable of reconstructing the OI at any of these frequencies. We have also tried another state-of-the-art inversion algorithm; namely, multiplicative regularized contrast source inversion (MR-CSI) [4] to invert these three different high frequency data sets, and have also observed the same failure with this algorithm. We think that the reason for the failure of both of these two inversion algorithms is due to the fact that for a given measurement scenario, as the frequency of operation becomes larger than a threshold level, the utilized inversion algorithm might not be able to capture the increased nonlinearity of the associated MWT problem. In other words, it might not be able to model the presence of more multiple scattering events. For example, in this case, at the frequency of 8 GHz, the MR-GNI algorithm converges at the data misfit error of 53.31%. This indicates that the MR-GNI algorithm has been trapped in a wrong local minima. For the MR-GNI algorithm to handle this increased nonlinearity, it may require a better initial guess for the contrast profile than the zero contrast which has been used here.

4.2.1 Simultaneous multiple-frequency inversion

In the previous subsection, we investigated the effect of the frequency of operation in single-frequency MWT data inversion. In this subsection, we investigate how simultaneous multiple-frequency data inversion can improve the achievable MWT resolution. (Note that multiple-frequency inversion requires collection of a multiple-frequency data set. To collect a multiple-frequency data set, the utilized antenna element needs to be able to operate at multiple frequencies.) To this end, let's consider the simultaneous inversion of nine different data sets, each of which corresponds to one of the nine frequencies considered in the previous subsection ranging from 500 MHz to 8 GHz. (Similar to the above subsection, each of these nine data sets is collected using 16 transceivers at the noise level of 3%.) The power spectrum $|\tilde{v}_i(f_x, f_y = 0)|^2$ corresponding to the simultaneous multiple-frequency inversion is shown in Figure 4.20a. As can be seen, the “V” shape of this power spectrum is more flared out as compared to the power spectrum of the same example in single-frequency inversion as shown in Figure 4.15. This indicates that with this simultaneous frequency inversion, we can potentially resolve more features as we have the chance to incorporate higher spatial frequency contents into the reconstructed contrast. Also, it should be noted that for this example $m = 16 \times 15 \times 9 = 2160$ whereas n is still 10^4. Therefore, $\min(m, n) = 2160$; that’s why that the last index in this plot goes to 2160 according to (3.6). Now, we should see how many of these right singular vectors can be used in the reconstruction of the unknown contrast. This can be seen by plotting $|u_i^H b|/\sigma_i$ and finding the index at which these coefficients start to blow up. As can be seen in Figure 4.20b, these coefficients tend to blow up at a higher index as compared to the same scenario for single-frequency inversion; e.g., compare this with the single-frequency inversion at 5 GHz in Figure 4.20b. That means that we can use more right singular vectors for the reconstruction of the unknown profile in simultaneous frequency inversion as compared to 5 GHz inversion. Also, those right singular vectors corresponding to simultaneous inversion have higher spatial frequencies as compared to those for 5 GHz as their “V” shape power spectrum is more flared out. Therefore, the simultaneous frequency inversion should be more successful as compared to 5 GHz inversion. This can be seen by comparing the simultaneous frequency reconstruction, shown in Figure 4.21, with 5 GHz single-frequency inversion shown in Figure 4.17e. As can be seen, the simultaneous frequency inversion was capable of resolving the three small fingers in the bottom left of the OI.

4.3 Number of transceivers

In this section, we investigate the role of the number of transceivers in the achievable resolution within our proposed framework. In most the examples we have seen so far, the number of transceivers is chosen to be 16, thus, having $16 \times 15 = 240$ data points. We now consider two different scenarios with two different number of transceivers: 8 and 32. These line source transceivers are equally located on a circle of radius 0.15 m. Therefore, in these two scenarios, the number of measured data points will be $m = 8 \times 7 = 56$ and $m = 32 \times 31 = 992$ respectively. At each scenario, the data collection is performed at 9 different frequencies starting from 500 MHz and then going from 1 GHz to 8 GHz with the step of 1 GHz. (Similar to the previous section, 3% noise is added to the data sets.) Some sample power spectra corresponding to single-frequency inversion as well as simultaneous multiple-frequency inversion have been shown in Figure 4.22. As can be seen, the right singular vectors tend to cover a broader range of spatial frequencies as the number of transmitter increases. This can be seen by noting that the "V" shape power spectrum tend to flare out more when the number of transceivers is 32. Also, as expected, with the increase of the frequency of operation, the right singular vectors tend to cover a wider range of spatial frequencies. Finally, the right singular vectors corresponding to the simultaneous frequency inversion have the best spatial frequency coverage as compared to their corresponding single-frequency inversion. It should also be noted that 6 GHz, 7 GHz, and 8 GHz inversion for the scenario with 8 transceivers failed, but it was successful for the scenario with 32 transceivers. This is probably due to the fact that as the frequency of operation increases, the MWT problem becomes more nonlinear; thus, it requires more scattering information to converge to an appropriate reconstruction.

Now, let's take a look at the coefficients $|u_i^H b|/\sigma_i$ for these two scenarios including their corresponding simultaneous frequency inversion, which are shown in Figure 4.23. As noted in the previous paragraph, the single-frequency inversion at 6, 7, and 8 GHz failed when the number of transceivers is 8. Therefore, these cases have not been included in Figure 4.23(a). As can be seen, in general, when we increase the number of antennas, it is more likely to include more right singular vectors in the expansion of the unknown profile. This often results in enhanced reconstruction as can be seen in Figure 4.24. However, for some frequencies of operation, e.g., 500 MHz, the coefficients $|u_i^H b|/\sigma_i$ tend to blow up almost at the same index for these two scenarios; thus, the reconstruction will be almost similar as can also be seen in Figure 4.24(a) and (b). As expected from the coverage of the spatial frequencies, shown in Figure 4.22(h), and the number of right singular vectors that can be utilized for profile reconstruction, as shown in Figure 4.23(b), the simultaneous multiple-frequency inversion when the number of transceivers is 32 is capable of providing an almost perfect reconstruction, as shown in Figure 4.24(h).

4.4 Experimental Results

In this section, we consider one of the experimental data set collected by the Fresnel Institute [49]. This experimental data set is referred to as *FoamTwinDielTM* by the Institute Fresnel [49]. The target in this experimental data set consist of three dielectric circular cylinders. Two of these cylinders have a diameter of 31 mm, and a relative permittivity of 3 ± 0.3. The other cylinder has a diameter of 80 mm and a relative permittivity of 1.45 ± 0.15. This target is irradiated from 8 different angles, and the resulting scattering field is collected at 241 points at 9 different frequencies ranging from 2 GHz to 10 GHz with the step of 1 GHz. Note that the Fresnel Institute did not use co-resident antenna elements to collect this data set. In fact, they perform data collection at different location by physical movement of the antenna. That's why they were able to have 241 receiving points per transmitter. (For practical imaging applications, we are often interested in having co-resident antenna elements in the MWT chamber to perform fast data collection.)

Now, let's start by observing the power spectrum plots corresponding to single-frequency and multiple-frequency inversion of this data set, shown in Figure 4.25. In the first glance, we might think that these spectra are almost identical. However, if we look more carefully at these plots, we will see that these spectra consist of a “V”-shape structure and then a flat strip right after the “V”. As the frequency increases, the length of the “V” increases, and the length of the flat strip decreases. Also, in the case of multiple-frequency inversion, the length of the flat strip is almost zero. As pointed out in [40], the flat strip corresponds to right singular vectors whose corresponding singular values are extremely small. Therefore, the calculation of these right singular vectors and their power spectra might not be sufficiently accurate. Taking this point into account, we can see that as the frequency increases, the amount of reliable high spatial frequency contents increases. Specifically, when we deal with multiple-frequency inversion, see Figure 4.25(i), we have the potential to incorporate even more high spatial frequency contents into the reconstructed contrast. Now, let’s take a look at the variation of $|u_i^H b|/\sigma_i$ for four different single-frequency inversion cases, and the multiple-frequency inversion scenario. As also expected, these coefficients blow up later as the frequency of operation increases. Specifically, when we deal with multiple-frequency inversion, the blow-up of these coefficients has the slowest rate. That indicates that as the frequency of operation increases, and specially when we do multiple-frequency inversion, we can incorporate more right singular vectors into the reconstructed contrast. Now, let’s consider the reconstructed permittivity profile as shown in Figure 4.27. As also expected by the previous discussion on the power spectra and the $u_i^H b/\sigma_i$ coefficients as the frequency of operation increases, the reconstructed permittivity profile improves. We also note that single-frequency inversion at 9 GHz failed as shown in Figure 4.27(h). As pointed out previously, this is due to the fact that the initial guess for the MR-GNI algorithm, which is the zero contrast, is not appropriate to be used with this frequency of operation due to the increased nonlinearity of the MWT problem at this frequency. Also, as expected, the simultaneous multiple-frequency inversion provides the most accurate reconstruction.[5]

[5] It should be noted that, the 8 GHz reconstruction is very similar to multiple-frequency reconstruction. This is probably due to the fact that the number of incorporated right singular vectors in 8 GHz and their frequency contents were sufficient to capture the target.

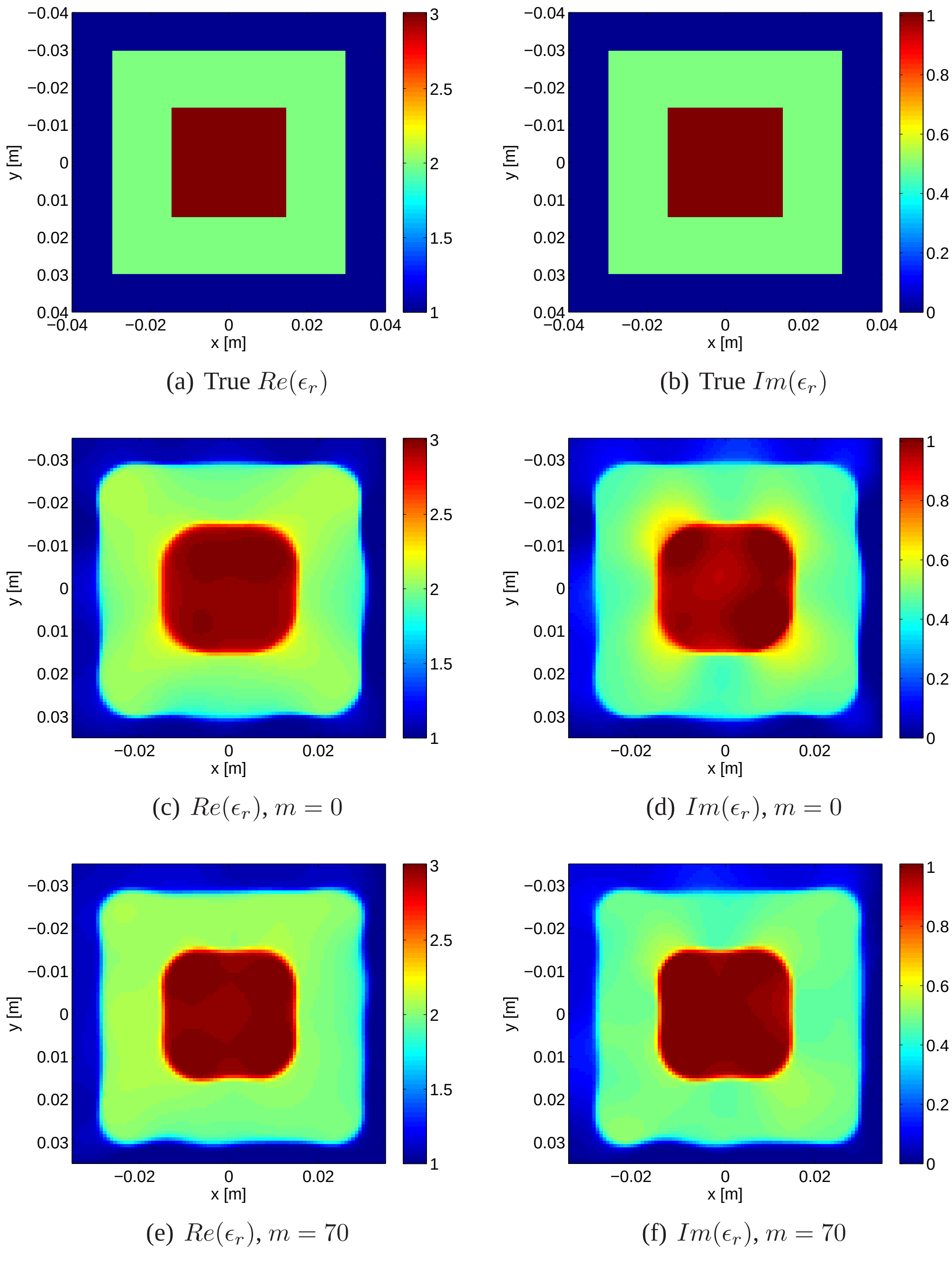

(a) True $Re(\epsilon_r)$ (b) True $Im(\epsilon_r)$

(c) $Re(\epsilon_r)$, $m = 0$ (d) $Im(\epsilon_r)$, $m = 0$

(e) $Re(\epsilon_r)$, $m = 70$ (f) $Im(\epsilon_r)$, $m = 70$

Fig. 4.12: Concentric squares test case using 32 antennas: (a)-(b) true dielectric profile; reconstructed dielectric profile when (c)-(d) $m = 0$, and (e)-(f) $m = 70$.

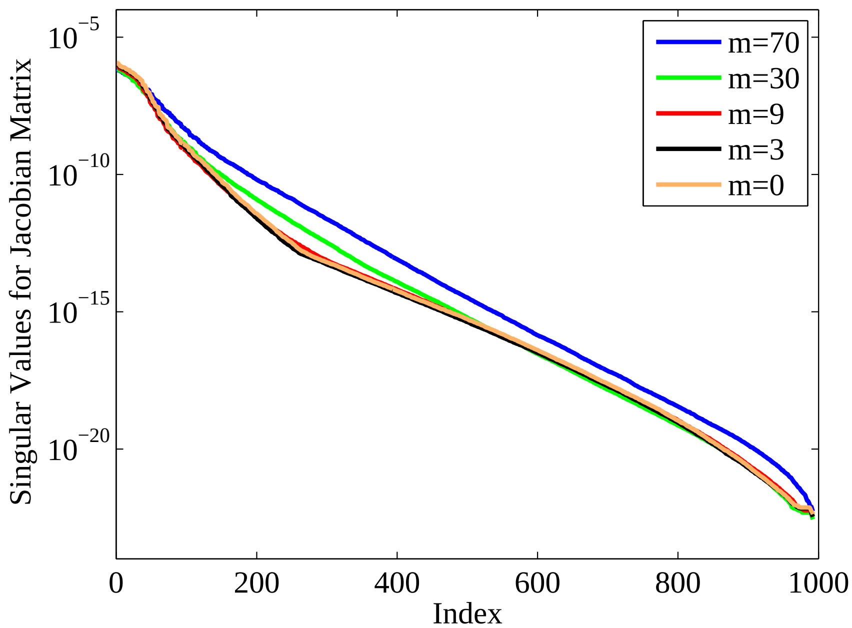

Fig. 4.13: Singular values of the Jacobian matrix at the last MR-GNI iteration for different m values for the concentric squares test case.

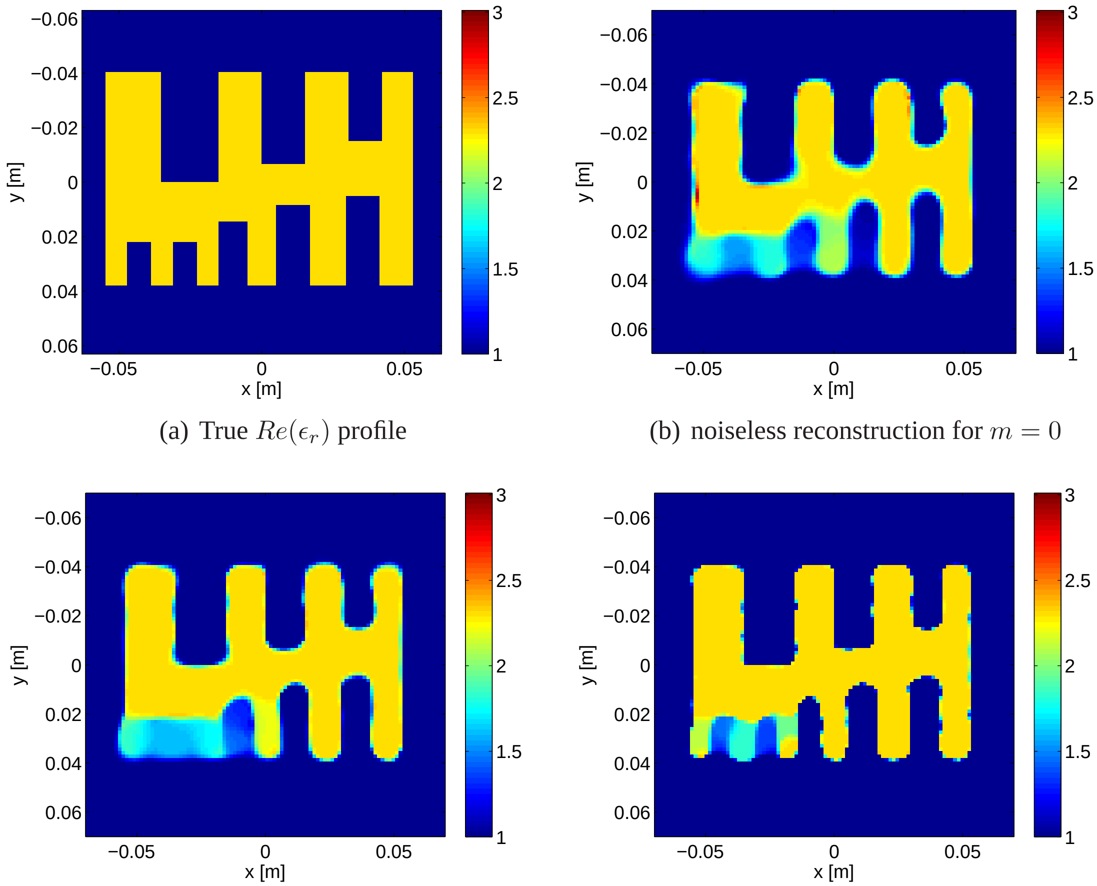

(a) True $Re(\epsilon_r)$ profile

(b) noiseless reconstruction for $m = 0$

(c) noiseless reconstruction for $m = 70$

(d) noiseless reconstruction for $m = 300$

Fig. 4.14: Inversion of the **noiseless** data sets for the lossless target; (a) True Profile $Re(\epsilon_r)$, (b) $m = 0$, (c) $m = 70$, and (d) $m = 300$.

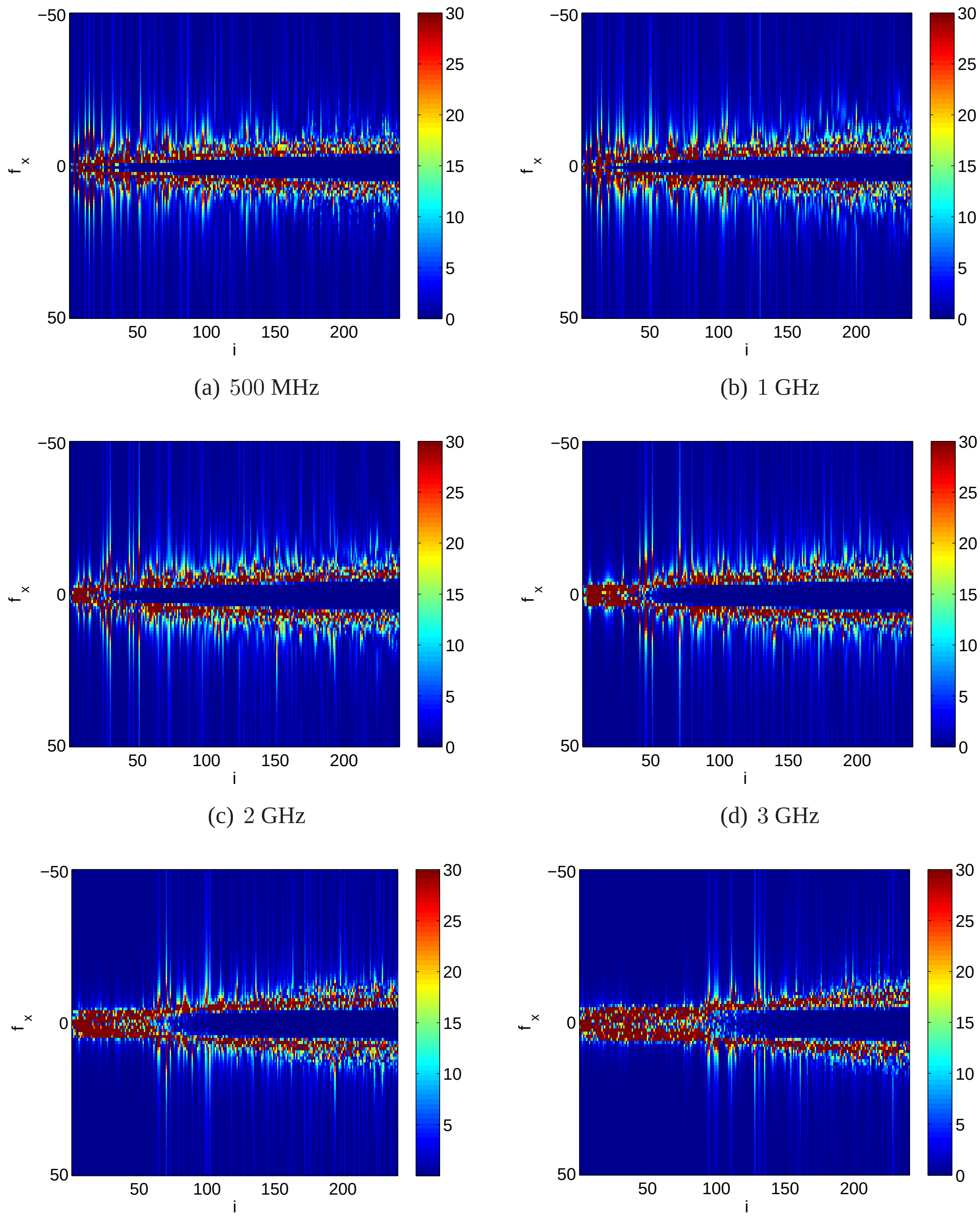

(a) 500 MHz (b) 1 GHz (c) 2 GHz (d) 3 GHz (e) 4 GHz (f) 5 GHz

Fig. 4.15: Power spectrum plots: $|\tilde{v}_i(f_x, f_y = 0)|^2$ for i values and f_x indices at six different frequencies of operation when the noise level is $\eta = 3\%$. (Each column of the above images represents the power spectrum of a given v_i with respect to f_x.)

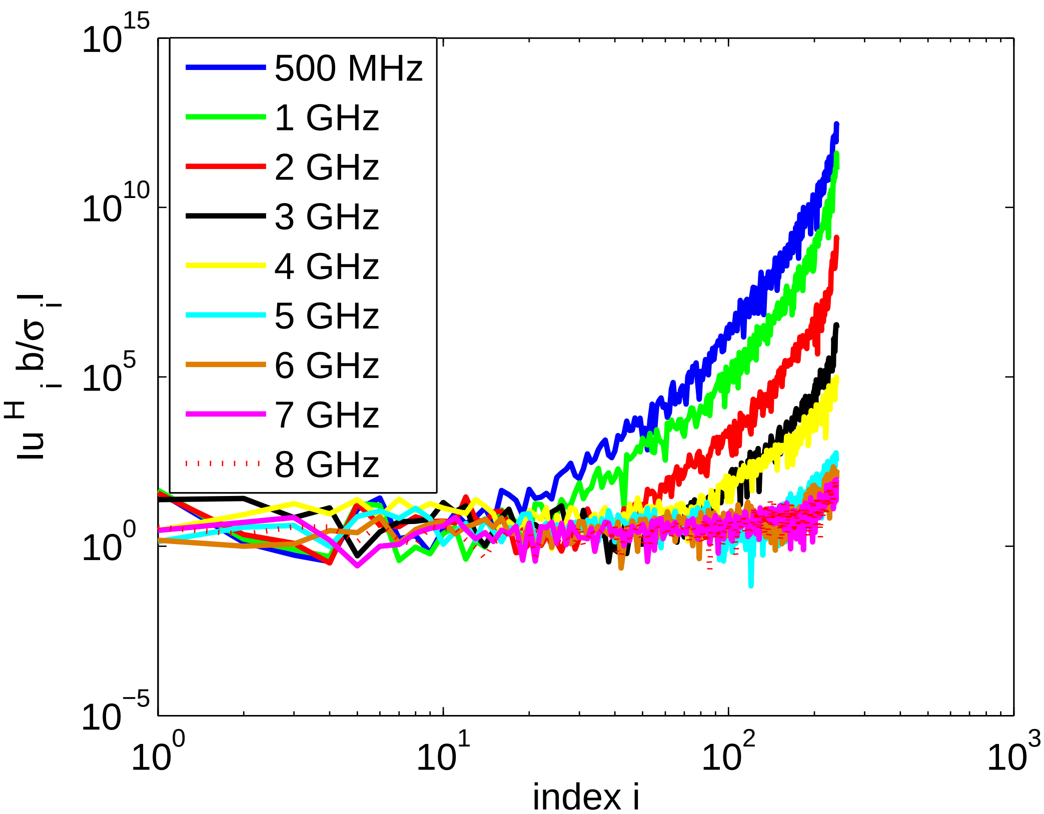

(a) $\frac{|u_i^H b|}{\sigma_i}$ versus i

Fig. 4.16: The variation of the magnitude of $u_i^H b/\sigma_i$ with respect to i at 9 different frequencies when the noise level is $\eta = 3\%$.

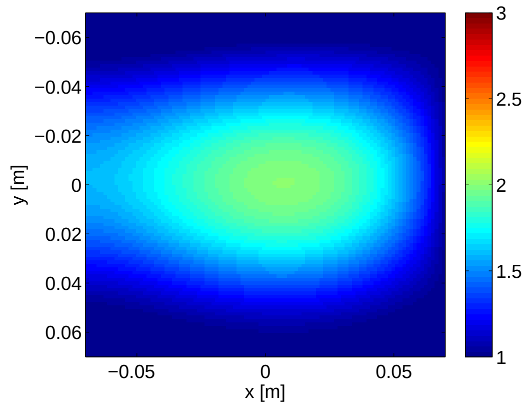

(a) $Re(\epsilon_r^{\text{recons}})$, 500 MHz

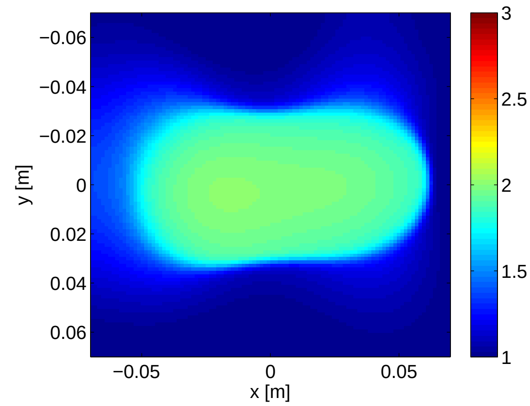

(b) $Re(\epsilon_r^{\text{recons}})$, 1 GHz

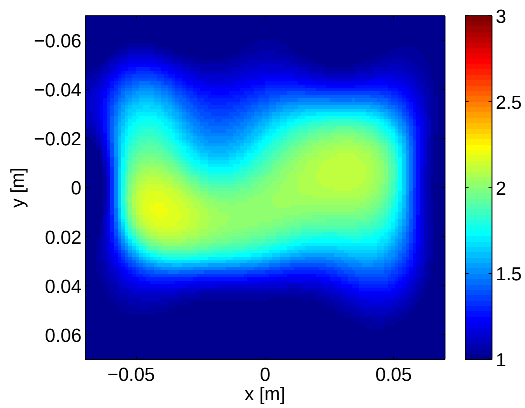

(c) $Re(\epsilon_r^{\text{recons}})$, 2 GHz

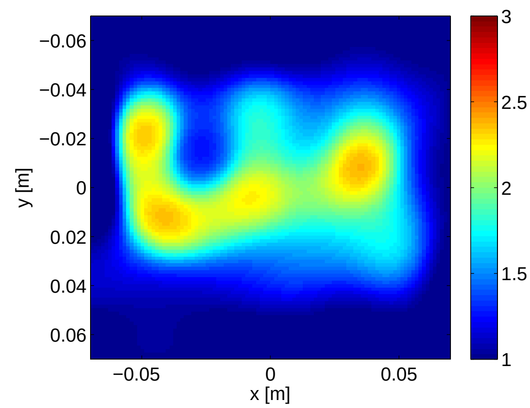

(d) $Re(\epsilon_r^{\text{recons}})$, 3 GHz

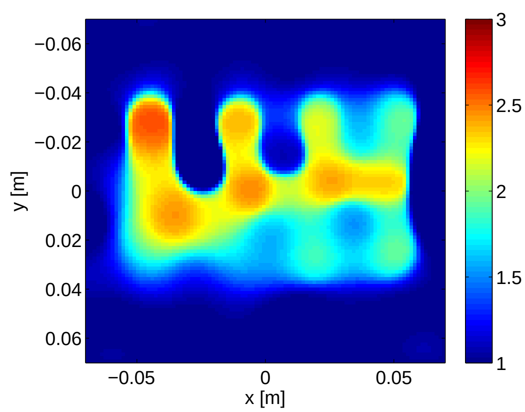

(e) $Re(\epsilon_r^{\text{recons}})$, 4 GHz

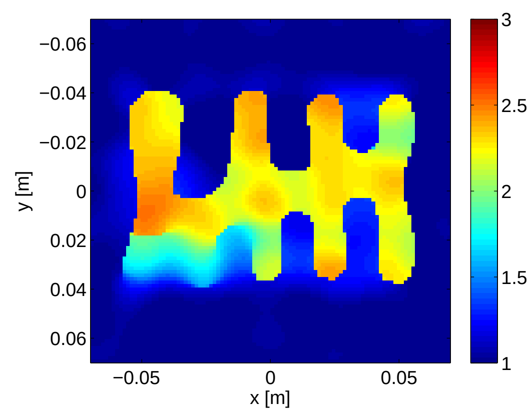

(f) $Re(\epsilon_r^{\text{recons}})$, 5 GHz

Fig. 4.17: The reconstructed permittivity, $\epsilon_r^{\text{recons}}$, of the E-target when irradiated by 16 antennas at six different frequencies of operation at the fixed noise levels of $\eta = 3\%$.

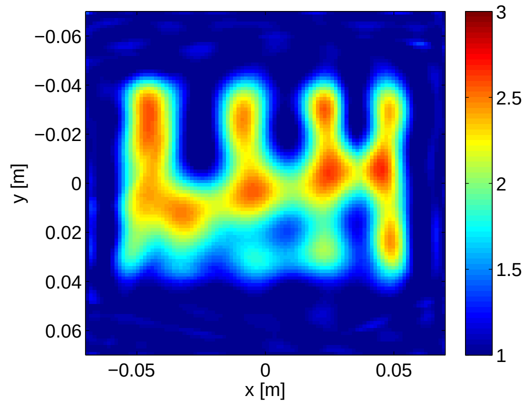

(a) $Re(\epsilon_r^{\forall i})$, 500 MHz

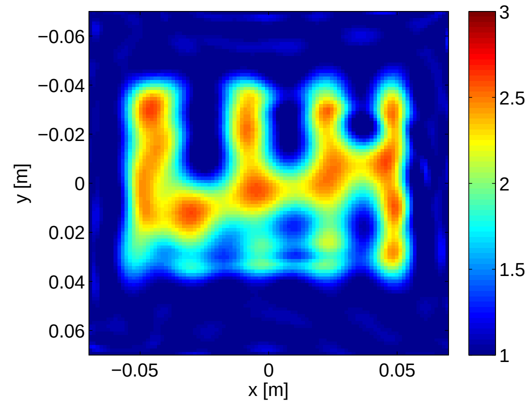

(b) $Re(\epsilon_r^{\forall i})$, 1 GHz

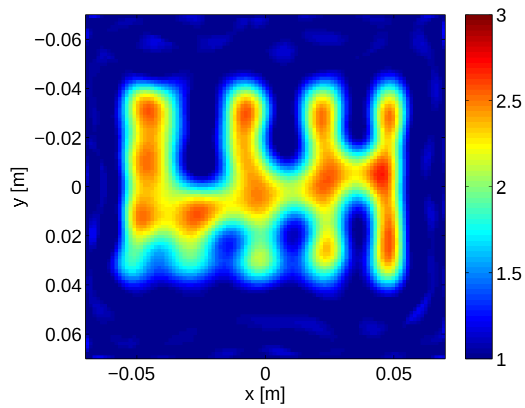

(c) $Re(\epsilon_r^{\forall i})$, 2 GHz

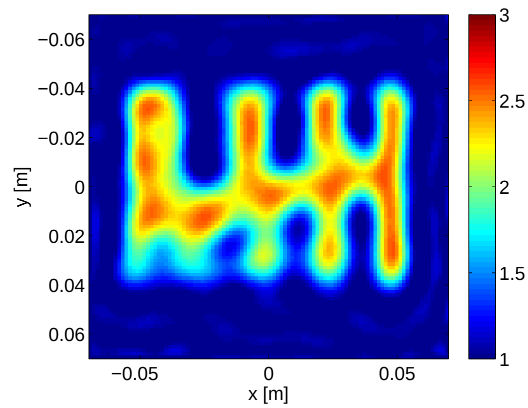

(d) $Re(\epsilon_r^{\forall i})$, 3 GHz

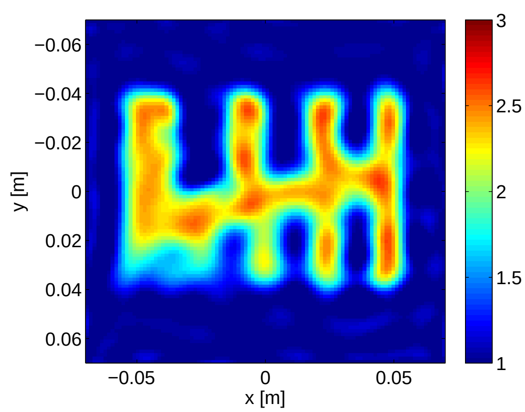

(e) $Re(\epsilon_r^{\forall i})$, 4 GHz

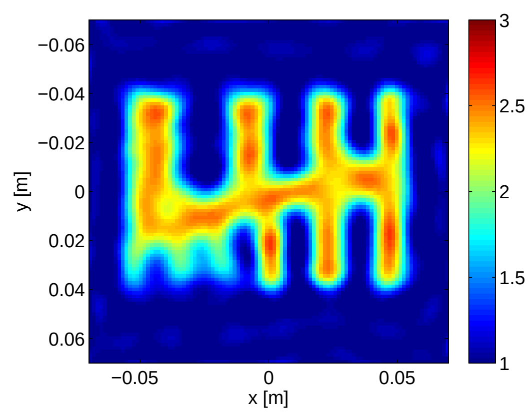

(f) $Re(\epsilon_r^{\forall i})$, 5 GHz

Fig. 4.18: Direct expansion of the true E-target permittivity profile, $\epsilon_r^{\forall v_i}$, using all the right singular vectors v_i when irradiated by 16 antennas at six different frequencies of operation at the fixed noise level of $\eta = 3\%$.

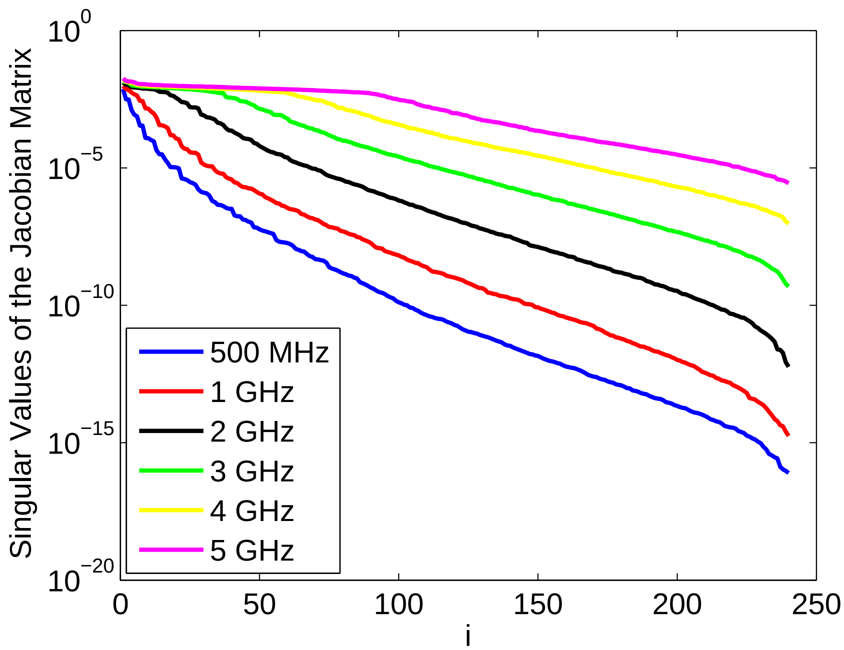

(a) Singular values

Fig. 4.19: Singular values corresponding to the E-target permittivity profile test case when irradiated by 16 transceivers at the noise level of $\eta = 3\%$ for six different frequencies of operation.

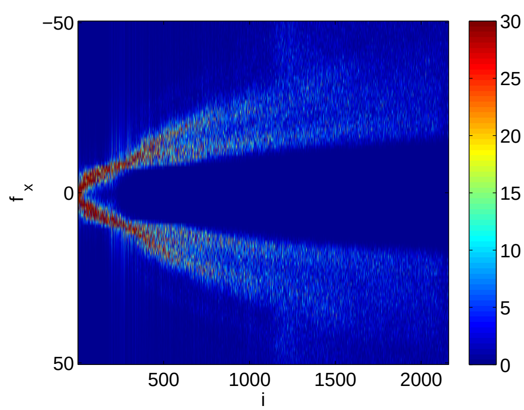

(a) Power spectrum plot

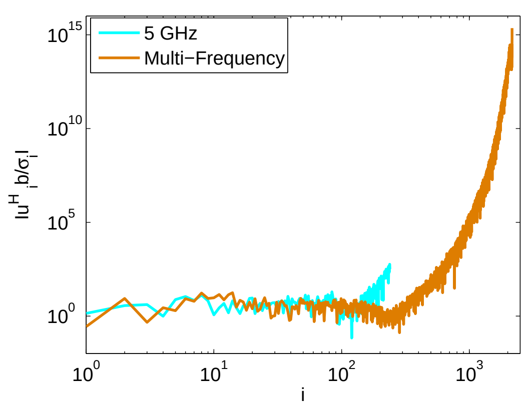

(b) $\frac{|u_i^H b|}{\sigma_i}$

Fig. 4.20: Simultaneous inversion of nine different frequencies of operation ranging from 500 MHz to 8 GHz when the noise level is $\eta = 3\%$. Left: Power spectrum plot, $|\tilde{v}_i(f_x, f_y = 0)|^2$, for different i values and f_x indices (Each column of the above images represents the power spectrum of a given v_i with respect to f_x.) Right: Magnitude of $u_i^H b/\sigma_i$ versus different i indices for two cases: simultaneous multiple-frequency inversion and single-frequency inversion at 5 GHz.

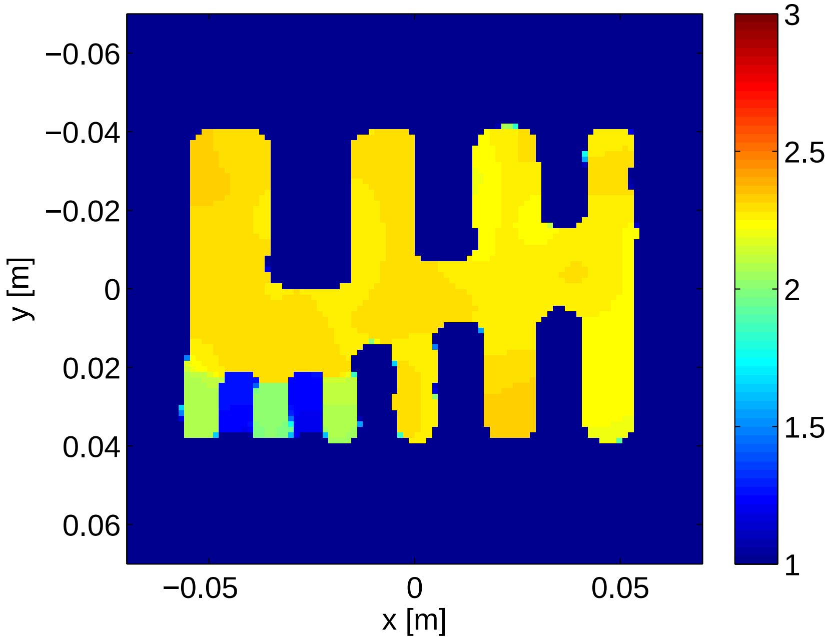

(a) $Re(\epsilon_r^{\text{recons}})$

Fig. 4.21: Simultaneous multiple-frequency inversion: The reconstructed permittivity, $\epsilon_r^{\text{recons}}$, of the E-target when irradiated by 16 antennas at nine different frequencies of operation at the fixed noise levels of $\eta = 3\%$.

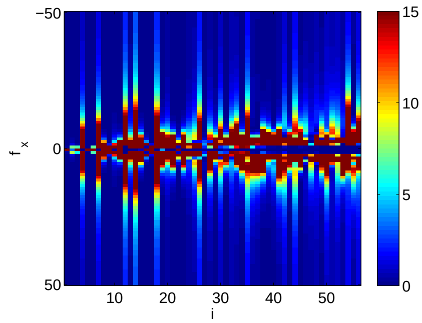

(a) 8 transceivers, 500 MHz

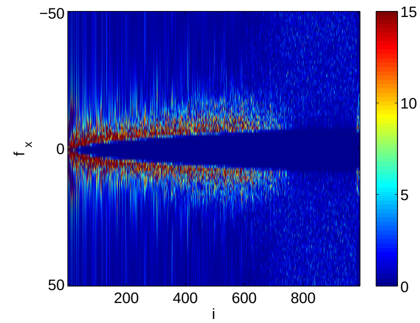

(b) 32 transceivers, 500 MHz

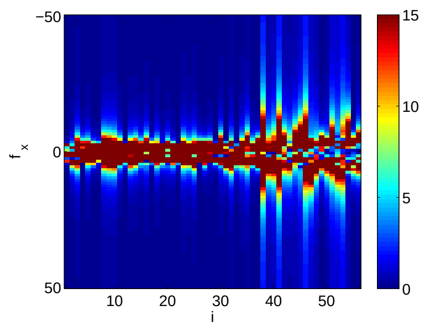

(c) 8 transceivers, 3 GHz

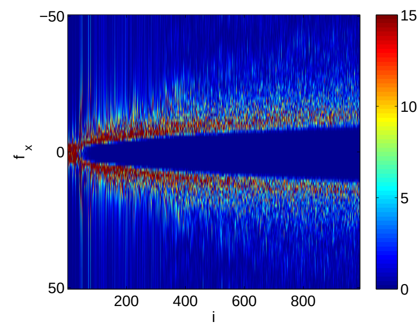

(d) 32 transceivers, 3 GHz

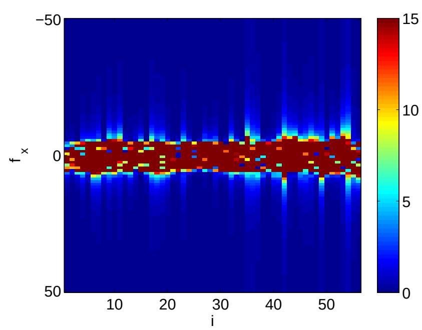

(e) 8 transceivers, 5 GHz

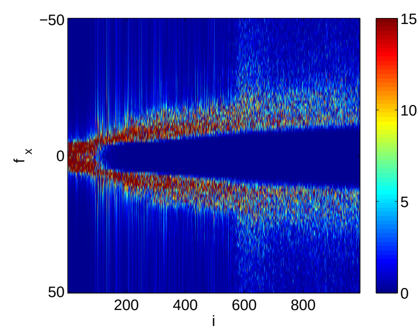

(f) 32 transceivers, 5 GHz

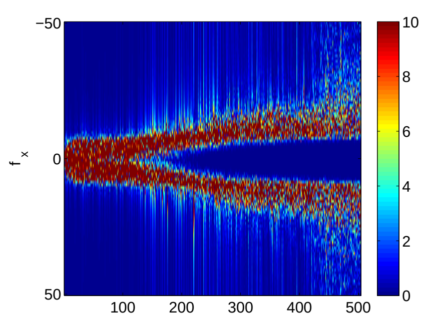

(g) 8 transceivers, multiple frequency

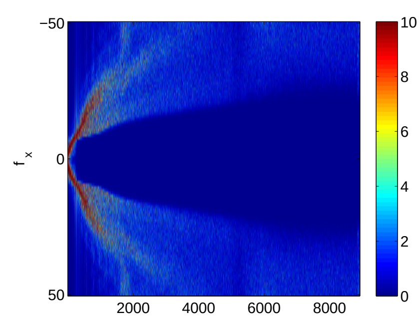

(h) 32 transceivers, multiple frequency

Fig. 4.22: Power spectrum plots: $|\tilde{v}_i(f_x, f_y = 0)|^2$ for i values and f_x indices for single-frequency and multiple-frequency inversion for two different number of transceivers: [Left]: 8 transceivers, and [right]: 32 transceivers. (Noise level is $\eta = 3\%$.)

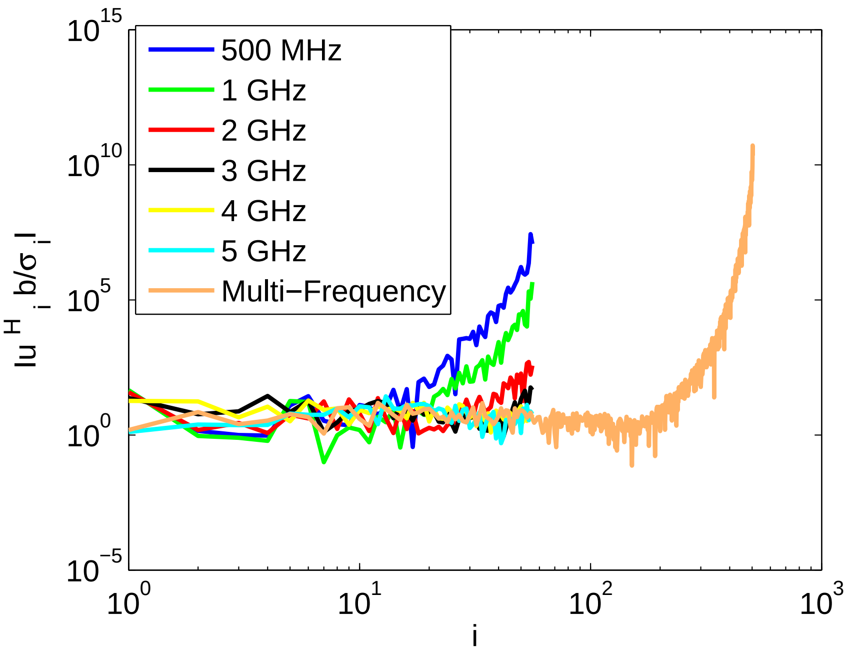

(a) 8 transceivers

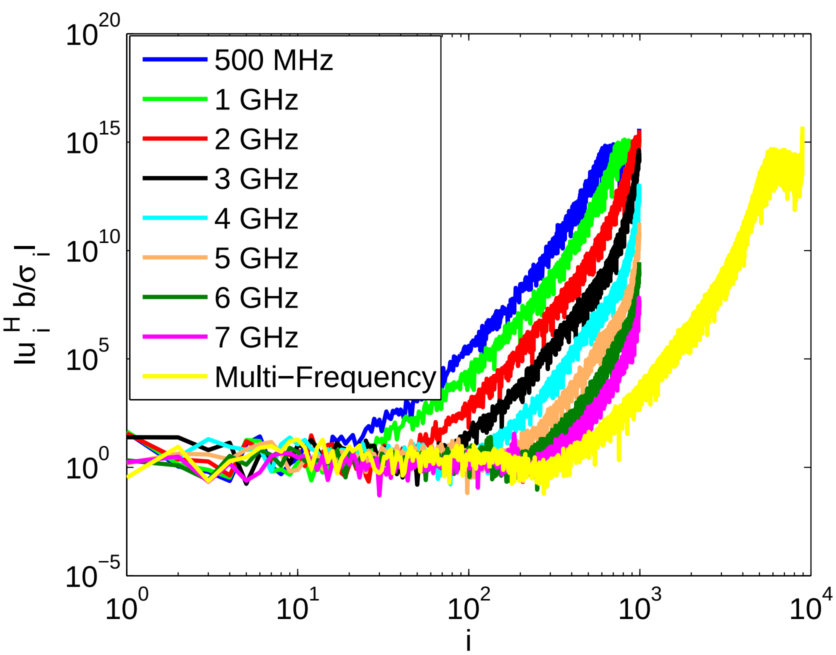

(b) 32 transceivers

Fig. 4.23: The variation of the magnitude of $u_i^H b/\sigma_i$ with respect to i at different single-frequency and multiple-frequency cases for two different scenarios: [Top] when the number of transceivers is 8, and [Bottom] when the number of transceivers is 32. (Noise level is $\eta = 3\%$.)

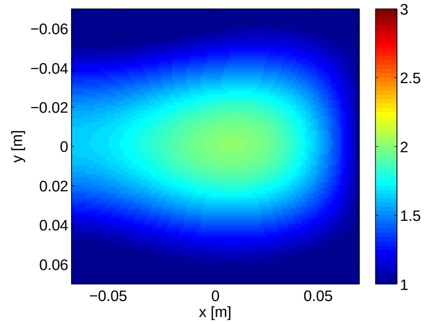

(a) 8 transceivers, 500 MHz

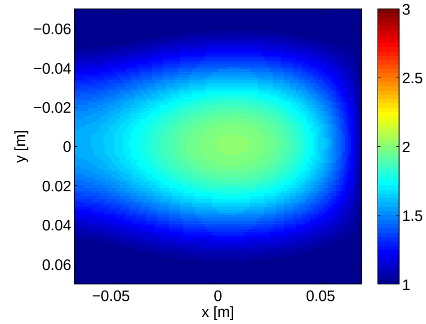

(b) 32 transceivers, 500 MHz

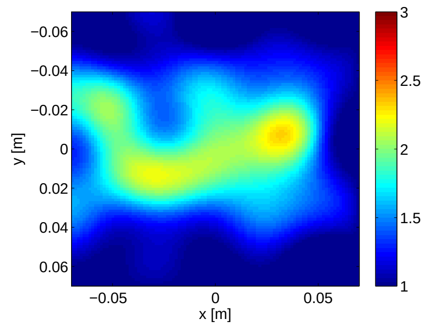

(c) 8 transceivers, 3 GHz

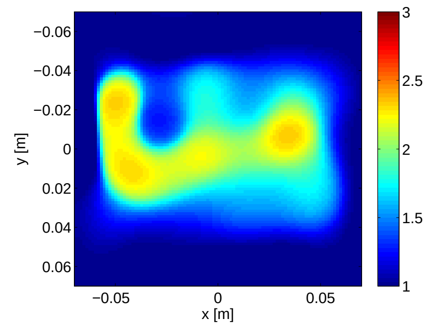

(d) 32 transceivers, 3 GHz

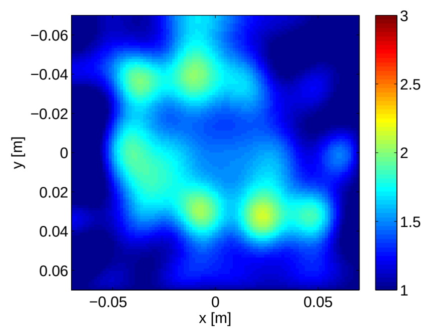

(e) 8 transceivers, 5 GHz

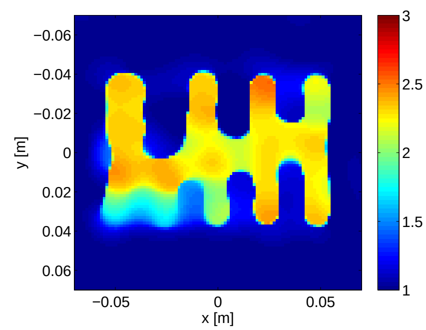

(f) 32 transceivers, 5 GHz

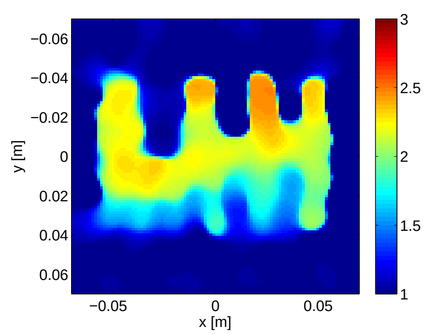

(g) 8 transceivers, multiple frequency

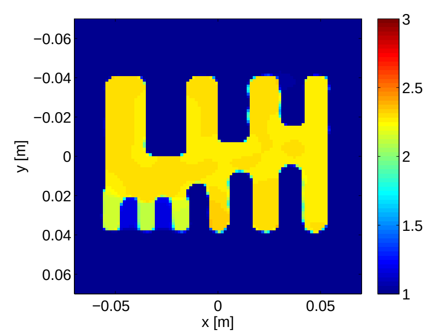

(h) 32 transceivers, multiple frequency

Fig. 4.24: The reconstructed real-part of the permittivity, $Re(\epsilon_r^{\text{recons}})$, of the E-target when irradiated by [Left] 8 transceivers and [Right] 32 transceivers in single-frequency and multiple-frequency inversion. (Noise level is set to $\eta = 3\%$.)

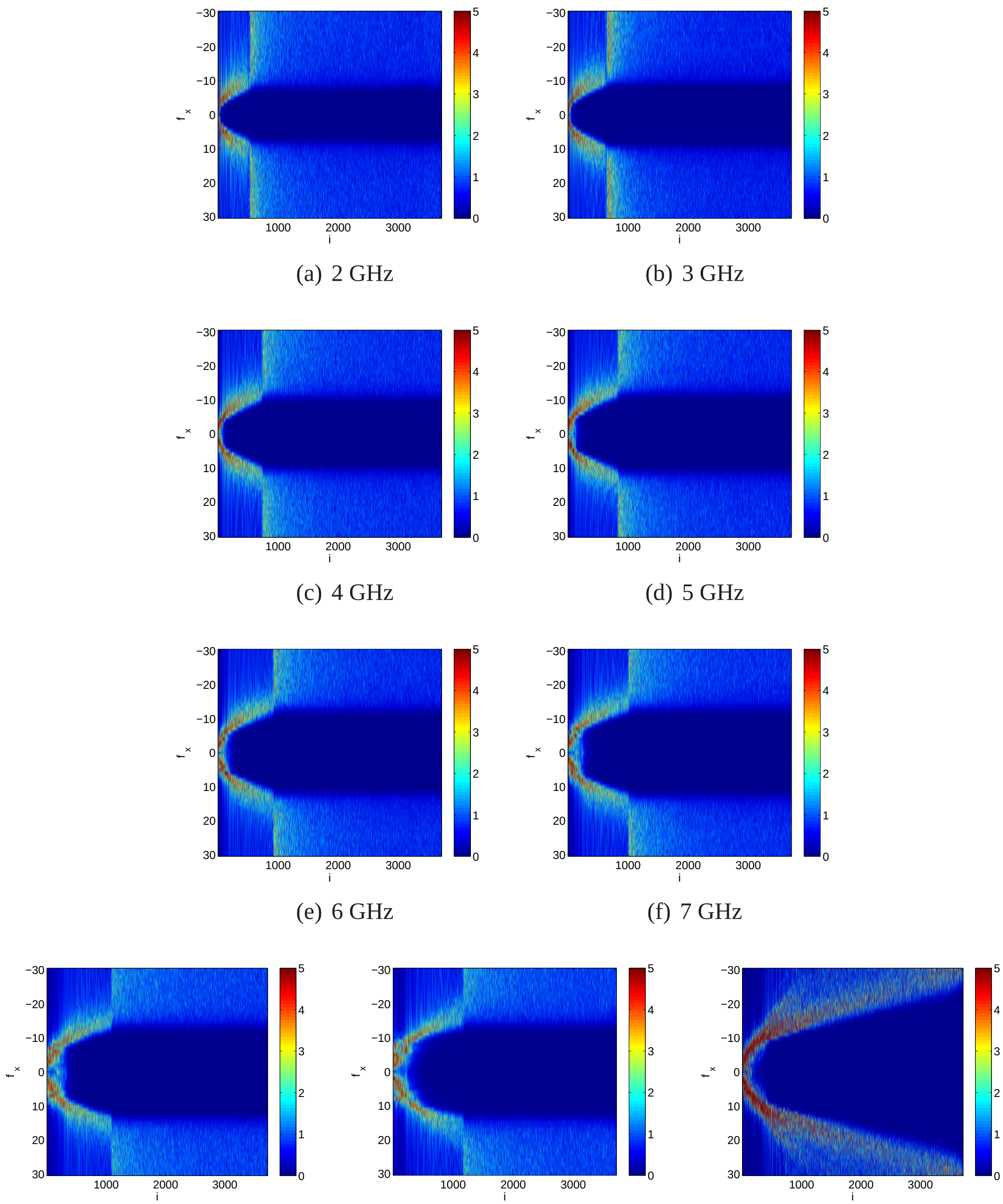

(a) 2 GHz (b) 3 GHz

(c) 4 GHz (d) 5 GHz

(e) 6 GHz (f) 7 GHz

(g) 8 GHz (h) 9 GHz (i) Multiple frequency

Fig. 4.25: Power spectrum plots for *FoamTwinDielTM* experimental data set: $|\tilde{v}_i(f_x, f_y = 0)|^2$ at 8 different single frequency inversion cases, and one multiple-frequency inversion scenario.

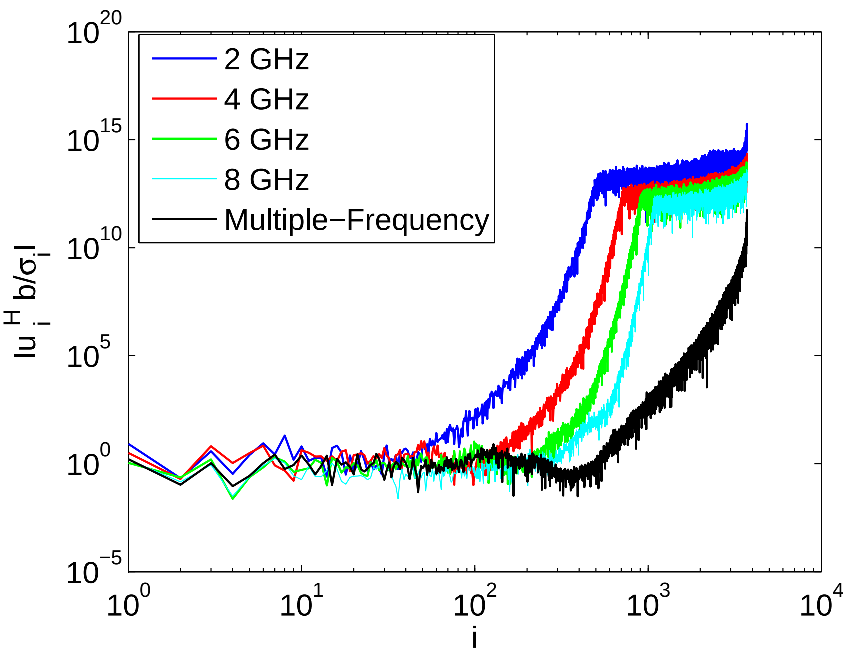

Fig. 4.26: Variation of the magnitude of $u_i^H b/\sigma_i$ for the *FoamTwnDielTM* experimental data set at four different single-frequency cases and one multiple-frequency inversion scenario.

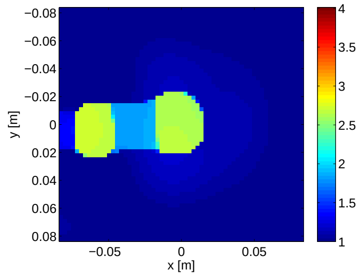

(a) $Re(\epsilon_r^{\text{recons}})\ 2\ GHz$

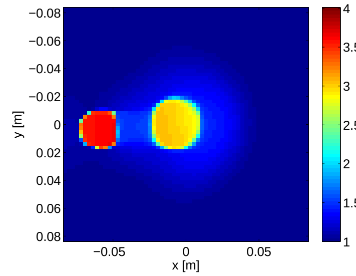

(b) $Re(\epsilon_r^{\text{recons}})\ 3\ GHz$

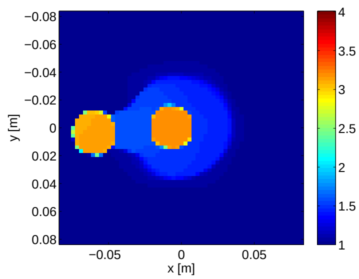

(c) $Re(\epsilon_r^{\text{recons}})\ 4\ GHz$

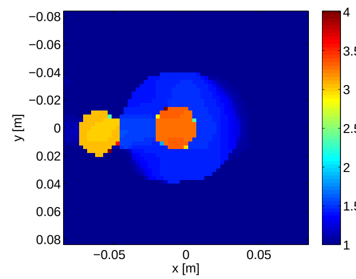

(d) $Re(\epsilon_r^{\text{recons}})\ 5\ GHz$

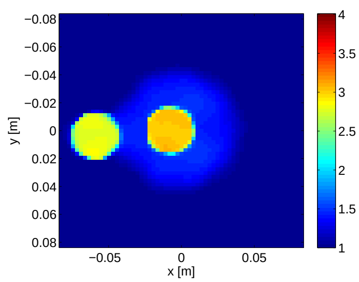

(e) $Re(\epsilon_r^{\text{recons}})\ 6\ GHz$

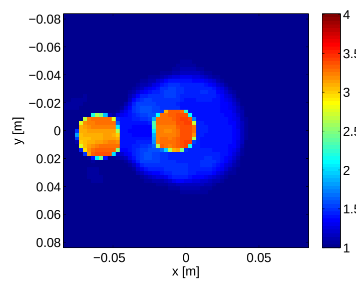

(f) $Re(\epsilon_r^{\text{recons}})\ 7\ GHz$

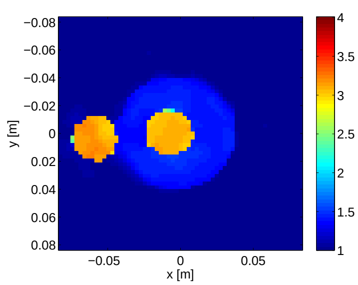

(g) $Re(\epsilon_r^{\text{recons}})\ 8\ GHz$

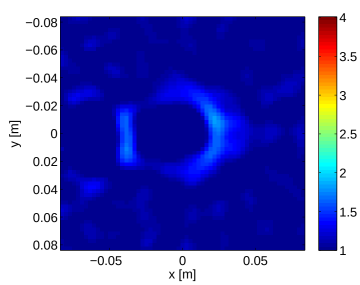

(h) $Re(\epsilon_r^{\text{recons}})\ 9\ GHz$

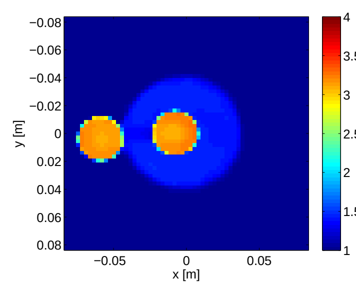

(i) $Re(\epsilon_r^{\text{recons}})$ Multiple frequency

Fig. 4.27: The reconstructed real-part of the permittivity, $Re(\epsilon_r^{\text{recons}})$, of the *FoamTwinDielTM* target 8 different single frequency inversion cases, and the multiple-frequency inversion scenario.

5

Focused Incident Field Implementation

In this Chapter, we first review three different approaches that might be employed to create a focused near-field distribution. We then go over the first approach. The second approach will be the topic of Chapter 6.[1]. The third approach will not be considered in this thesis.

5.1 Available options

We have so far numerically demonstrated that the use of appropriate incident fields, often having a focused distribution, can enhance the achievable accuracy and resolution. To practically achieve this, three different strategies might be employed

1. Use of appropriate synthesized incident fields,

[1] This chapter is based on the following publication: N. Bayat, P. Mojabi, and J. LoVetri, "Use of Synthesized Fields in Microwave Tomography Inversion," *International Symposium on Antenna Technology and Applied Electromagnetics*, Victoria, British Columbia, Canada, July 2014.

2. Use of appropriate antennas, and

3. Use of a combination of the above two methods.

Before starting our discussion on the first strategy, let's consider the second strategy. Within the second strategy, promising methods such as near-field plates [50] can be utilized to achieve high levels of near-field focusing. The main difficulty with using such methods is that the utilized antenna should also satisfy some other criteria; *e.g.*, being reasonably small to allow sufficient sampling resolution, having sufficient bandwidth to allow multiple-frequency data collection. However, such near-field plates are often single-frequency components and they are usually electrically large. As an alternative, some existing antennas can be modified so as to increase their near-field focusing abilities [51, 52]. Based on this alternative method, we have modified an antenna element that will be presented in Chapter 6. Another possible method based on the second strategy relies on using antenna array techniques. This can be practical as MWT setups usually utilize co-resident antenna elements ranging from 16 to 64 antennas [4, 11, 23, 39, 53] placed in an imaging chamber. Currently, these antennas are being used individually for illuminating the OI. Therefore, there is an opportunity to collectively use all these antenna elements to create sufficient number of appropriate incident field distributions. This can be pursued by proper simultaneous excitation of these co-resident antenna elements using antenna array techniques.

The first strategy, on the other hand, does not attempt to design new antennas or modify the existing ones. It simply casts the actual MWT problem into a new problem by synthetically creating focused incident fields from the actual ones. The possibility of using this strategy is the focus of this chapter of this thesis.

5.2 Synthesized Fields

Consider T antennas that are placed outside the imaging domain $\mathcal{D}$ in a two-dimensional transverse magnetic time-harmonic MWT system. The (calibrated) incident fields of these antennas are assumed to have an omnidirectional distribution.

Discretizing $\mathcal{D}$ into N cells, the discrete form of the tth incident field distribution inside $\mathcal{D}$ will be a complex vector of length N; say, $E_t^{\text{inc}} \in \mathbb{C}^N$. Denoting the number of receiving cites per transmitter by M, the scattered data due to this incident field will then be stored in $E_t^{\text{scat}} \in \mathbb{C}^M$. We have already shown that the use of "sufficiently" focused incident field can enhance imaging results [18]. Now, let's assume that such desired focused incident field is represented by [18]

$$E_{t,m}^{\text{inc,des}} = E_t^{\text{inc}} \odot [\cos^m \psi] \tag{5.1}$$

where t is the index of the transmitter, ψ is the angle between the tth antenna's boresight axis and the line connecting each cell within $\mathcal{D}$ to the antenna. The parameter $m \in \mathbb{R}^+$ controls the focusing level; the larger m, the larger focusing level. Also, $[\cos^m \psi] \in \mathbb{R}^N$, and $\odot$ denotes the Hadamard product (element by element product) of the two vectors. The question that needs to be answered here is whether or not we can create a synthesized incident field, say $\mathcal{E}_{t,m}^{\text{inc}}$, from E_i^{inc} $(\forall i)$ that is sufficiently close to $E_{t,m}^{\text{inc,des}}$. To this end, a linear combination of E_i^{inc} $(\forall i)$ can be utilized as

$$\mathcal{E}_{t,m}^{\text{inc}} = \boldsymbol{\mathcal{L}}(E_i^{\text{inc}}|\alpha_{t,i}^m) \triangleq \sum_{i=1}^{T} \alpha_{t,i}^m \, E_i^{\text{inc}}. \tag{5.2}$$

The complex weighting coefficients $\alpha_{t,i}^m$ are to be found by minimizing the following L_2-norm

$$\alpha_{t,i}^m = \arg\min_{\alpha_{t,i}^m} \left|\left| E_{t,m}^{\text{inc,des}} - \sum_{i=1}^{T} \alpha_{t,i}^m \, E_i^{\text{inc}} \right|\right|_2^2. \tag{5.3}$$

Once $\alpha_{t,i}^{m}$ are found for each transmitter, we can construct T different synthesized incident fields based on (5.2), and also calculate their corresponding synthesized scattered fields as $\mathcal{E}_{t,m}^{\text{scat}} = \boldsymbol{\mathcal{L}}(E_i^{\text{scat}}|\alpha_{t,i}^{m})$.

The original MWT problem, which was to reconstruct the OI's dielectric profile based on the knowledge of the actual incident and scattered fields, can now be casted as a synthesized problem that aims to find the same unknown but using the synthesized incident and scattered fields. Based on the above discussion it can be concluded that if the synthesized incident field is "sufficiently" focused, the inversion of its corresponding synthesized scattering data set outperform the inversion of the original data set.

Now, let's consider an example that shows the use of such synthesized focused incident fields. Consider the OI shown in Figure 5.1(a), which consists of three circles. The separation between the top circles is 0.12λ where $\lambda = 0.1$ m is the wavelength of operation. The shortest distance between the top and bottom circles is 0.08λ. The OI is successively irradiated by 24 antennas, equally distributed on a circle of radius 0.1 m. The resulting scattered fields are collected by all the antennas; thus, having 24^2 data points. (3% noise is added to the data.) We now consider reconstructing this target by the multiplicative regularized Gauss-Newton inversion [43] of three different data sets. First, let's consider the data set that has been collected by the use of omnidirectional incident fields E_i^{inc} $(\forall i)$. The distribution of this incident field in $\mathcal{D}$ (discretized into 100×100 cells) corresponding to the 1st transmitter is shown in Figure 5.2(a). Inversion of this data set, shown in Figure 5.1(b), cannot resolve the bottom circle, and also underestimates the permittivity values of the top circles. Now, let's assume that we have access to a desired focused incident field, say $E_{t,70}^{\text{inc,des}}$, whose distribution is shown in Figure 5.2(b). The inversion of the data set collected by this incident field is shown in Figure 5.1(c): the three circles are now resolved with more accurate quantitative accuracy. However, the size of the circles are now underestimated. This might be due to the fact that the reconstructed permittivities are overestimated for top circles; thus, compensating for smaller reconstructed shapes. The same numerical experiment is also performed with $E^{\text{inc,des}}_{t,300}$. As can be seen, this incident field can almost completely resolve these three circles.

Now, we consider inverting synthesized data sets, $\mathcal{E}^{\text{scat}}_{t,m} = \boldsymbol{\mathcal{L}}(E^{\text{scat}}_{i}|\alpha^{m}_{t,i})$ for two m values: 70 and 300. Based on our discussion in Section 5.2, if we can synthesize an $\mathcal{E}^{\text{inc}}_{t,m}$ which is “sufficiently” close to $E^{\text{inc,des}}_{t,m}$ for $m = \{70, 300\}$, we can expect that the inversion of these two synthesized data sets become similar to those shown in Figure 5.1(c) and (d). Minimization of (5.3) for $m = \{70, 300\}$ results in synthesized incident fields that are shown in Figure 5.2(d) and (e). As can be seen, these two synthesized incident fields are not sufficiently close to the desired focused incident fields shown in Figure 5.2(b) and (d). Therefore, the reconstruction results corresponding to these two synthesized incident fields, shown in Figure 5.1(e) and (f), are not as good as those obtained by the focused incident fields.

We now explain why we were not able to create a synthesized incident field that is sufficiently close to the desired focused one. The number of equations that needs to be satisfied to match the synthesized and focused incident fields is equal to the number of cells within $\mathcal{D}$. On the other hand, the number of weighting coefficients to be determined is the same as the number of antennas. That is, for this example, the number of equations is 10^4, and the number of unknowns is 24. We are, in fact, dealing with an over-determined system of equations; thus, it cannot be guaranteed that an $\mathcal{E}^{\text{inc}}_{t,m}$ that is sufficiently close to $E^{\text{inc,des}}_{t,m}$ can be obtained. Due to this, if we push to create a synthesized incident field with even more focusing, say $\mathcal{E}^{\text{inc}}_{1,500}$, its resulting distribution does not change that much as shown in Figure 5.2(f). One question that may now arise is that whether increasing the number of antennas can alleviate this imbalance. We tried increasing the number of antennas; but, we could not obtain better synthesized incident fields. In fact, after increasing the number of

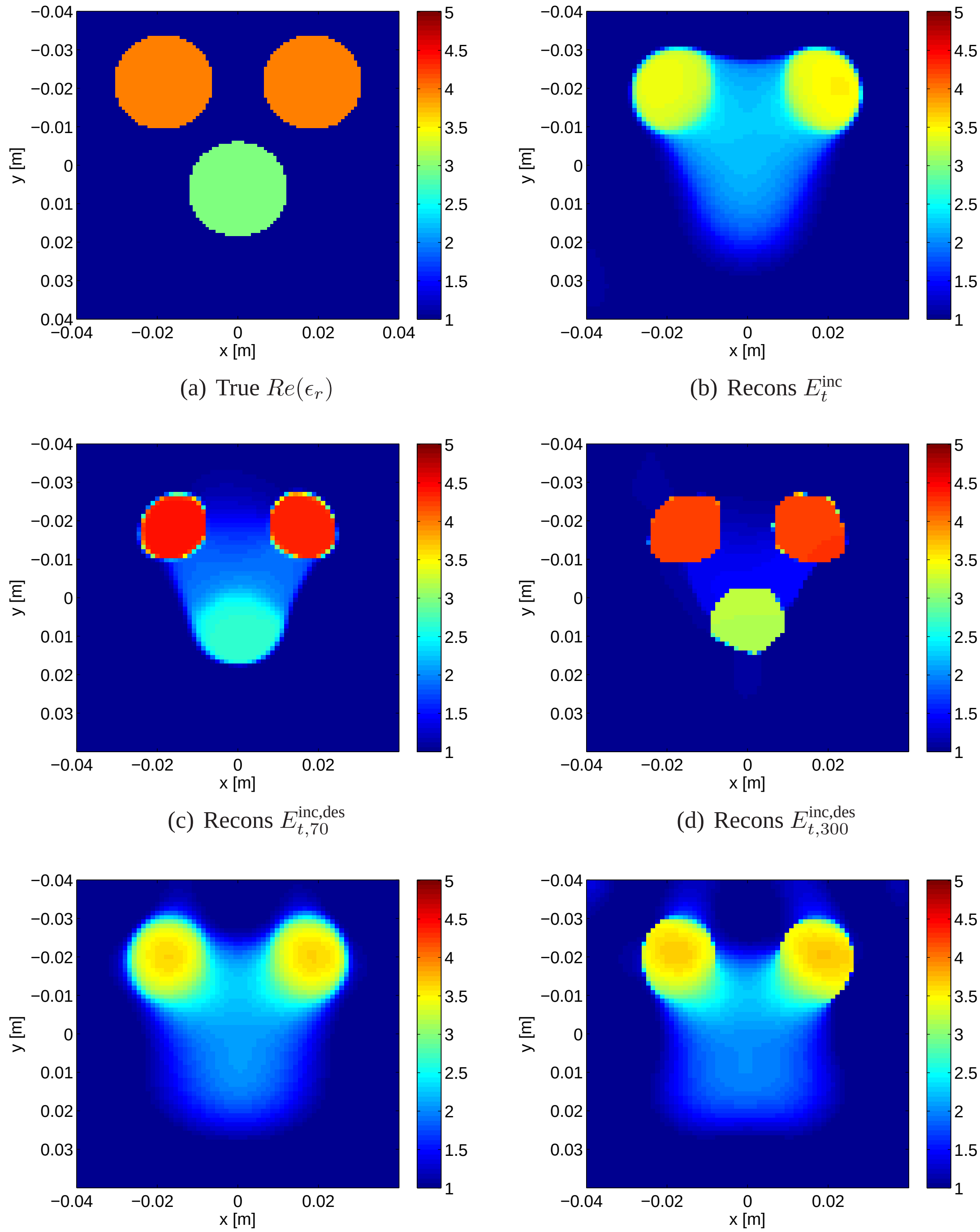

(a) True $Re(\epsilon_r)$

(b) Recons E_t^{inc}

(c) Recons $E_{t,70}^{\text{inc,des}}$

(d) Recons $E_{t,300}^{\text{inc,des}}$

(e) Recons $\mathcal{E}_{t,70}^{\text{inc}}$

(f) Recons $\mathcal{E}_{t,300}^{\text{inc}}$

Fig. 5.1: True OI and its reconstruction by the use of different incident fields. © IEEE 2014 [1]

antennas beyond a certain level, the least squares minimization (5.3) became rank deficient. This is due to the fact that the incident field distributions of two successive antennas in a dense antenna array will become very similar. This manifests itself as two similar rows in the matrix associated with the least squares minimization. In other words, adding too many antennas, in fact, adds dependent information to the system of equations; thus, it will not be able to solve the imbalance issue. The other question that may arise is: why does inverting these synthesized and actual data sets result in different reconstructions noting the fact that the synthesized data sets are created solely based on the information within the actual data set? This can be explained by noting that a change in the utilized incident field distribution affects the singular values and singular vectors of the associated ill-posed problem. Therefore, although the amount of information does not change, the unknown dielectric profile will be effectively expanded in different vector spaces.

In summary, this chapter discussed that the use of synthesized fields, as presented herein, did not result in enhanced reconstruction. It should be noted that synthesizing other incident field distributions and their synthesis using a different approach are yet to be investigated for MWT.

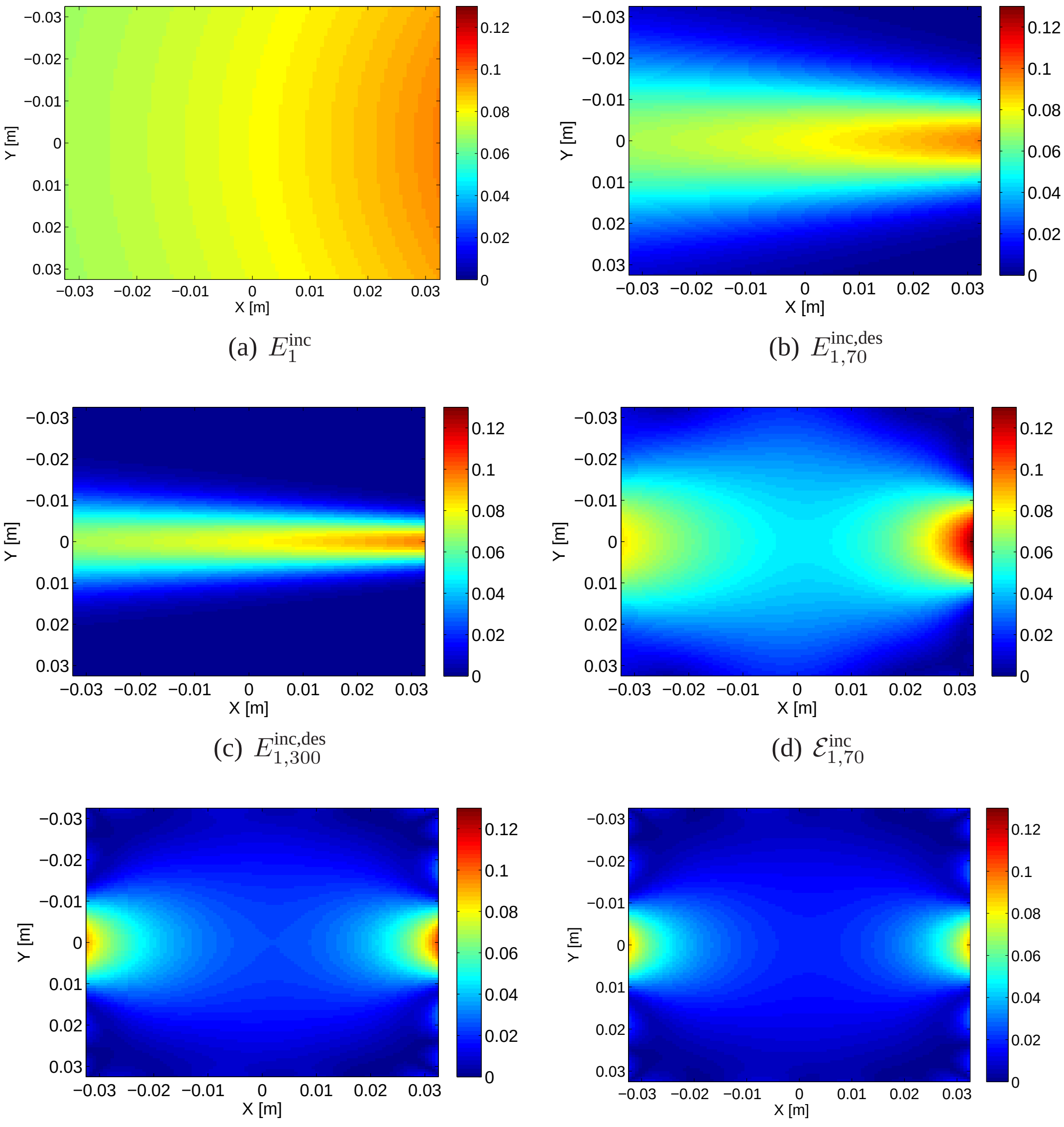

(a) E_1^{inc} (b) $E_{1,70}^{\text{inc,des}}$

(c) $E_{1,300}^{\text{inc,des}}$ (d) $\mathcal{E}_{1,70}^{\text{inc}}$

(e) $\mathcal{E}_{1,300}^{\text{inc}}$ (f) $\mathcal{E}_{1,500}^{\text{inc}}$

Fig. 5.2: Different incident field distributions within the imaging domain. © IEEE 2014 [1]

6

Antenna Design and Measurements

Based on our discussion in Chapters 3 and 4, we are looking for a near-field focused incident field distribution that can be created by a small and multi-band antenna element. We also discuss the implementation of such near-field focused incident field distributions by the use of synthesized fields in Chapter 5. However, our proposed method to provide such synthesized beams failed. Therefore, in this chapter, we consider the second approach as mentioned in Section 5.1, and will consider an existing small ultrawideband antenna element, and then attempt to increase its near-field focusing level.[1] To this end, we will go over the background of this existing antenna element, and then explain the modifications that have been done on this antenna so as to improve its near-field focusing level. At the end, the simulation and measurement results will be presented.

[1] This is based on the following publication: N. Bayat and P. Mojabi, "Small Wide-band Antenna with more Focused Incident Field for increasing the Accuracy and Resolution of Microwave Tomography," *IEEE International Symposium on Antennas and Propagation and USNC-URSI Radio Science Meeting*, Memphis, Tennessee, USA, July 2014.

6.1 Literature review

Before starting our discussion regarding the antenna design, let's have a review on different antenna elements used for microwave imaging applications. Although the focus of this thesis is on MWT, the following literature review presents some antenna elements used for MWT as well as microwave radar-based imaging applications. The reason that we are including antenna elements for radar-based microwave imaging applications here is due to the fact that these antennas can also be used (or, have been used) in MWT as well.

The following literature review shows the following points:

- Most reported antenna designs for microwave imaging applications revolve around achieving two main goals: size reduction and increased bandwidth. More accurately, as will be seen in the rest of this section, the main trend in the antenna design for microwave imaging applications has been focused on achieving an appropriate trade-off between these two design goals.
- Although in most microwave imaging systems, antenna elements work in their near-field zones, the majority of the published works in this area are concerned with far-field properties of the antenna, which are not relevant for near-field imaging applications.
- To the best of the author's knowledge, the possibility of using appropriate near-field incident field distributions to enhance the achievable resolution and accuracy achievable from MWT has not been explored. (We have suggested the use of focused near-field distribution in MWT in [18, 54].)[2]
- In those antennas which have been used in 2D TM MWT systems, it has been implicitly assumed that the antenna is linearly polarized with the electric field component

[2] In radar-based microwave imaging, it has been recently suggested that the use of a focused near-field incident field distribution can enhance imaging results [51, 55].

perpendicular to the imaging domain. However, polarization is a far-field quantity, and is not appropriate to be used with the near-field concept.

Now, let's review some of the antenna elements that have been proposed for microwave imaging applications. To this end, let's start with printed antennas. These antennas are of particular interest to be used in microwave imaging systems due to being low cost, low profile, and light weight. Also, the fabrication of these antennas has a high level of precision and is quick. However, they often suffer from having a narrow impedance bandwidth. Therefore, they can usually support single-frequency inversion, thus, the resolution and accuracy of the resulting image may suffer. In [56], two type of printed antennas have been used in MWT. The first one which operates in 900 MHz is the folded patch antenna. The folding technique miniaturizes the structure so as to help the designer to reduce the overall size of the antenna. The other antenna element is a bowtie patch antenna that operate at 2.7 GHz. To address the narrow impedance bandwidth, some research groups have tried to either increase the bandwidth of these antennas or making them multi-band. For example, in [57], a miniaturized dual-band patch antenna, which operates in safflower oil, has been designed for breast cancer imaging. In [58], a compact wideband microstrip antenna for utilizing in microwave radar-based imaging has been presented. Also, an stack-patch antenna element for increasing the bandwidth, while keeping the antenna size reasonably small, is proposed in [59].

Printed microstrip slot antennas have also been investigated for microwave imaging systems due to their attractive features such as low profile, light weight, ease of fabrication, and low cost. Several modifications have been reported for this antenna type so as to make it more appropriate for microwave imaging systems. These modifications mainly revolve around increasing the bandwidth and reducing the pulse distortions in time-domain systems. These modifications, for example, attempt to change the shape of the slots or modifying the feeding structure in order to increase the impedance bandwidth of the antenna or improving the stability of its radiation patterns over the frequency range of interest. For example, in [60], a P-shape slot antenna has been excited by a $50\ \Omega$ microstrip transmission line in order to achieve a wide band antenna with relatively stable radiation patterns over the frequency bandwidth. As another example, in [61], the modification has been done on the feed of the slot so as to achieve more impedance bandwidth when the antenna is in contact with the matching fluid.

Vivaldi antennas, as a type of tapered slot antennas (TSA), have also drawn much attention for microwave imaging applications due to their wide bandwidth characteristics as well as stable radiation characteristics over a large range of frequencies. For example, in [62], two type of Vivaldi antenna elements for microwave imaging applications have been proposed. In [55], a balanced antipodal Vivaldi antenna that incorporates a piece of higher dielectric constant material called “director” is proposed. To the best of the author’s knowledge, this paper is the first paper that proposed the use of focused near-field incident field distributions for radar-based microwave imaging applications. In [63], the Vivaldi antenna has also been used for microwave imaging applications with a so-called hybrid acquisition approach.[3] In [64], an antipodal Vivaldi antenna was modified so as to be used in a microwave imaging system. The modification of the antipodal Vivaldi antenna has been done by making its arms round and creating a smooth transition from the feed toward the aperture. This antenna provides an impedance bandwidth of about $3-20$ GHz. In [65], an antipodal type of TSA has been used for microwave imaging purposes. Also, in [66], a compact directional corrugated tapered slot antenna has been used in the mixture of water, glycerin, and corn syrup for radar-based microwave breast imaging applications. In [67], an ultrawideband tapered slot antenna [68] has been investigated in three different system configurations; namely,

[3] The hybrid acquisition approach consists of two measurements (one planar and one sagittal plane) at two different planes in order to find the location of the tumor inside the breast.

cylindrical, hemispherical and planar placement. In [69], a tapered microstrip slot antenna was introduced to be used in radar-based microwave imaging. The feed of this antenna has a fork-shaped configuration in order to improve its bandwidth. The improvement of TSAs' performance for microwave imaging applications has been another topic of research. For example, in [70], two methods have been introduced for the size reduction of the TSAs while keeping the impedance bandwidth and the directional properties of this antenna almost the same. The first method is based on the use of some slots and corrugations, while the other is based on making some elliptical cuts in the conducting planes of the TSAs.

Another antenna type which has been used in MWT is the coaxial monopole antenna [71]. These antennas can (*i*) be easily modeled, (*ii*) be positioned close to the OI, and (*iii*) provide dense sampling resolution for 2D TM MWT. On the other hand, they suffer from having narrow bandwidth, thus, often merely supporting single-frequency inversion. In the Dartmouth College MWT system, these monopole antennas are placed along the vertical direction [71]. On the other hand, in [72], a 3D MWT system is proposed that consists of 32 horizontally oriented coaxial monopole antennas. In this work, the authors used horizontally oriented monopole antennas as opposed to vertical ones so as to increase the number of antenna rings surrounding the OI. In [73], a diamond planar ultrawideband monopole antenna has been introduced for microwave imaging applications. The reason behind the use of a diamond-shape monopole antenna rather than some other shapes lies in its more stable radiation characteristics over the bandwidth of operation. However, this antenna suffer from having relatively a large physical size.

In [74], open-ended waveguide antennas have been used in an experimental MWT system. The main advantage of this antenna is that it can be easily incorporated into an MWT system having a metallic chamber. On the other hand, the disadvantage of this type of antennas is its relatively large dimensions which will not support having a dense array. Although this type of antennas is not narrowband, its minimum and maximum frequencies of operation are close to each other. In [75], a modified pyramidal horn antenna loaded with two resistors has been proposed to be used for radar-based microwave breast imaging. This antenna type has the same disadvantage as the open-ended waveguide antenna.

Finally, it should be noted that there have been some attempts to design antenna elements that are in direct contact with the OI. For example, in [76], a wideband antenna with a focused beam for radar-based microwave breast imaging has been proposed and simulated. In such designs, the fact that the antenna element is in direct contact with the OI makes the antenna element's properties extremely dependent on the OI. Since the OI is the actual unknown of the problem, this design for practical applications can be very challenging.

6.2 Background

As noted in the beginning of this chapter, we start our design from an existing antenna element. This antenna element is considered as a monopole-like slot antenna. We have chosen to utilize this antenna type due to its potential for having wide, or ultrawide, impedance bandwidth as well as being reasonably small. Moreover, as noted in [3], this antenna element is easy to be fabricated, has low fabrication cost, is lightweight, and is easy to be integrated with other RF components. (As will be seen by the end of this chapter, some modifications will be performed on this antenna type so as to enhance its near-field focusing abilities.)

In this section, a review on this type of antenna will be presented. This review follows the structure of another review that has been presented in [2]. To start this review, let's first consider conventional printed microstrip narrow-slot antennas. These antenna elements show narrow impedance characteristics. However, increasing the width of the slot and uti-

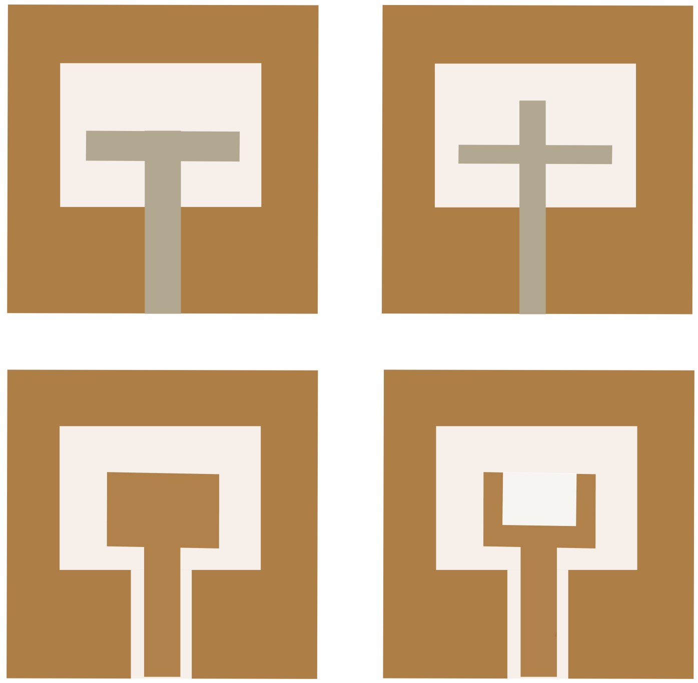

Fig. 6.1: Some typical types of wide slot antennas with microstrip line feeding structures or co-planar waveguide feeding structures. (This Figure has been re-drawn based on a Figure in [2])

lizing an open-ended feed line coupled with the slot can result in significant enhancement of the antenna's impedance bandwidth [77]. Different configurations of wide-slot antennas have been reported so far [78–80]. Figure 6.1, illustrates some of the slot antenna configurations [2]. The top row of Figure 6.1 shows two wide-slot antennas that have been fed by open-ended microstrip line, while the two others, shown in the bottom of the same figure, use the co-planar waveguide technique for feeding purposes. Although Figure 6.1 only demonstrates rectangular wide-slot antennas, the wide slot can be of various shapes such as, rectangular, square, triangular, circular, and elliptical, etc. In addition, the feeding structure of the wide-slot antenna can also be in the shape of a fork, cross, triangle, square, circle, arc, etc [2].

Monopole-like slot antennas evolve from wide-slot antennas by making the slot open. At this point, it might be worthwhile to mention that wide-slot antennas are the complementary structure of dipole antennas. On the other hand, monopole-like slot antennas will be the complementary structure of monopole antennas; thus, this type of slot antennas inherits the name of monopoles. Wide impedance bandwidth has also been reported for monopole-like slot antennas [3, 81–83]. As noted above, a monopole-like slot antenna consists of an open (wide) slot, generally etched on the ground plane of a printed circuit board (PCB) and a feeding structure. Having an open ground plane surrounding the slot offers more freedom in the design procedure. This increased degree of freedom may then be utilized to reduce the size of the antenna further and/or increase its impedance bandwidth. This antenna, similar to a wide-slot antenna, can be fed by a microstrip line or a coplanar waveguide (CPW) structure having a T-shaped or fork-shaped configuration.

The bandwidth of monopole-like antennas is dependent on the geometrical parameters of the slot and the utilized feeding configuration. For example, let's now consider the monopole-like slot antenna that will be used and modified in this chapter. For this antenna, which is fed by a fork-shaped feeding structure, it has been found that different parameters, e.g., the width of slot, length of the feeding structure's vertical stubs, and the separation between the vertical stubs, play important roles in the impedance bandwidth [3]. Through proper selection of these parameters the coupling between the feed and this monopole-like slot antennas can be controlled more effectively, thus, achieving significant bandwidth enhancement [2]. (The $|S_{11}|$ response of such antennas exhibits several deep nulls that indicates that the antenna operates at different dominant resonances due to the appropriately-shaped slot and the fork-shaped feed as well as the proper coupling between them [3].) In particular, this monopole-like slot antenna has been optimized so as to achieve an ultrawideband (UWB) impedance bandwidth [3].

Appendix D provides more detailed discussion on the radiation mechanism of the monopole-like slot antenna with the modifications that are yet to be explained. As will be seen in Section 6.3, some of the geometrical parameters of this antenna will be modified as compared to the antenna reported in [3]. The plots presented in Appendix D are based on these modified parameters.

6.3 Design procedure

In this section, the design procedure of a monopole-like slot antenna with improved near-field focusing will be presented. The antenna design procedure often starts with considering an "initial" antenna element. Several modifications will then be performed on this initial antenna so as to meet the new requirements. As noted several times in this thesis, we are interested in achieving a focused near-field distribution with a relatively small antenna that can launch electromagnetic waves at multiple frequencies. Our method to enhance the near-field focusing of our antenna is inspired by a recent work on a Vivaldi antenna for radar-based microwave imaging applications [55]. (This will be explained in more details below.) We knew that with the use of this method, it is very likely that the impedance bandwidth of the antenna suffers. Therefore, it seemed reasonable for the initial antenna to be a small UWB antenna. Our guess was that the UWB antenna can then afford to trade some of its bandwidth toward having more near-field focusing. Noting that we consider frequency-domain MWT systems, and not the time-domain MWT systems, we can afford to not have a UWB antenna; however, we still like to have multiple frequencies of operation so as to be able to perform multiple-frequency inversion. This thought procedure justified the use of the monopole-like slot antenna as presented in [3] as our initial antenna element. This antenna is small, about 26×29 mm^2, and is also UWB.

In our next step, we consider the fact that the final antenna eventually needs to be used in an actual MWT system. Of course, the OI will be located in front of the antenna, and will

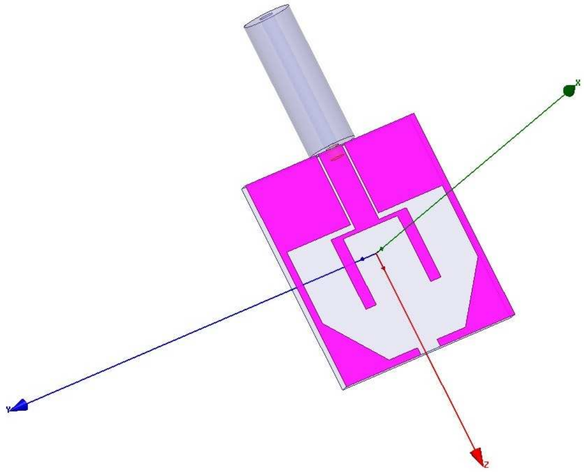

(a) Monopole-like slot antenna

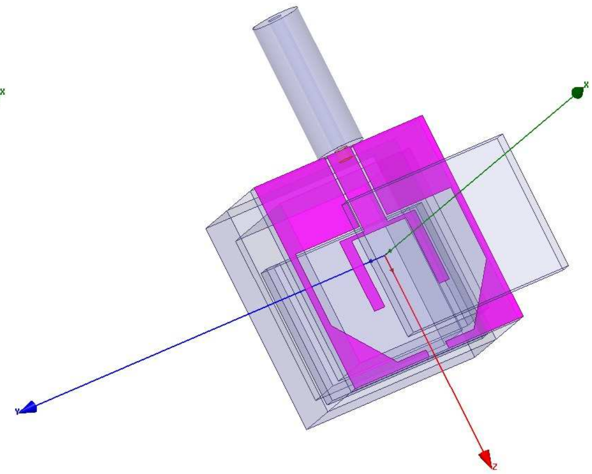

(b) Covered monopole-like slot antenna

Fig. 6.2: (a) Monopole-like slot antenna, and (b) Covered monopole-like slot antenna. The covered monopole-like slot antenna uses a metallic cavity and a superstrate as well as a dielectric material between the slot and the cavity.

be irradiated by the forward radiation[4] of the antenna. Now, if this antenna has a backward radiation, which is comparable to its forward radiation (e.g., consider a dipole antenna), it will not only illuminate the OI, but will also illuminate the feeding cables and the walls of the MWT chamber. The non-desired reflections from the cables and the walls will then contribute toward the overall noise of the MWT system as they are very difficult to be modeled by the inversion algorithm. (See Section 2.7.3 for more details regarding the overall noise.) Therefore, it is desirable for us to suppress the back radiation from this antenna so as to make it more suitable for MWT. To this end, we noticed that the authors of [83] have used a metallic cavity with radio frequency absorbers to suppress the back radiation from this antenna for portable UWB applications. Therefore, the idea used in [83] seemed to be appropriate for our application, and was used with some modifications, to be explained below.

[4] Note that the use of "radiation" in this sentence may not be very precise since the antenna element in the near-field MWT system does not operate in its far-field zone. Therefore, the use of "radiation" may not be appropriate. But, due to the fact that most of the antenna elements in a near-field MWT system operate in their radiating near-field zone, and not the reactive near-field zone, we choose to use the term "radiation".

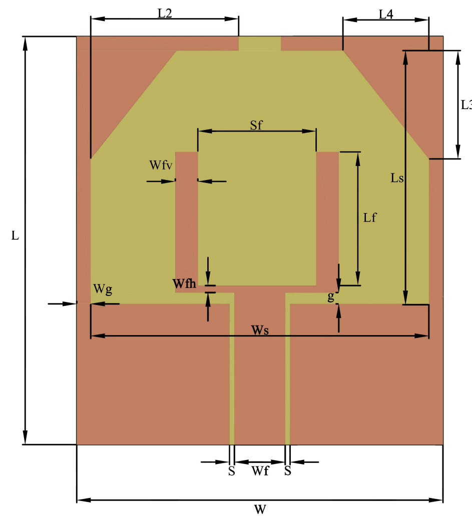

Fig. 6.3: Initial antenna element structure. (Note that after applying some modifications to this antenna, some of the geometrical parameters shown above are different than the original antenna as presented in [3].)

Now that we have described the beginning of our design and thought procedure, let's explain how the rest of the design is performed. The initial antenna (see [3]) was modeled in the ANSYS HFSS software. This software solves the Maxwell's equations using the finite element method. Figure 6.2(a) shows the initial antenna element as modeled in this software. (Note that this figure shows the initial antenna after performing some geometrical optimizations; thus, some of its dimensions differ from that reported in [3].) As can be seen in this Figure, we have chosen a Cartesian coordinate system in such a way that the top surface of the antenna lies within the $y-z$ plane. As can be seen in Figure 6.2(a), this antenna is fed by a fork-shaped CPW structure, which is itself fed by a $50\ \Omega$ coaxial cable. This fork-shaped tuning stub is composed of a horizontal section that meets with two vertical sections having an equal length. As noted in [3], proper tuning of the dimensions of these feeding configuration will result in a good impedance bandwidth specifically at higher frequency ranges. On the other hand, in order to enhance the impedance bandwidth of the antenna especially at lower frequencies, the tapers have been added to the top corners of the ground strips [3]. The overall size of the antenna and its substrate material is identical to the initial antenna

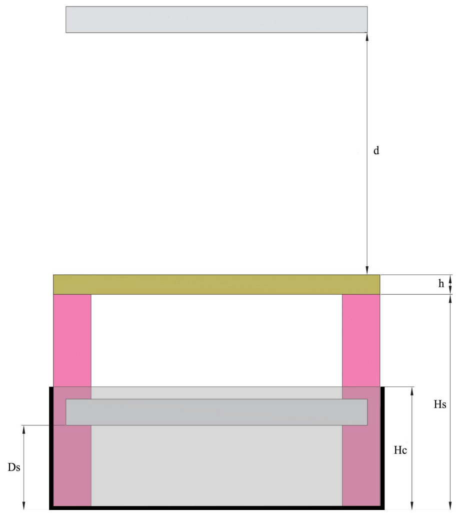

Fig. 6.4: Side view of the modified antenna element. The brown horizontal rectangle represents the monopole-like slot antenna, the two gray horizontal rectangles represent RT/duroid 6010 dielectric material, the two vertical purple rectangles represent Styrofoam used for holding the cavity and the monopole-like slot antenna together, and the black line represents the metallic cavity.

element [3]. Specifically, the slot and the feeding structure of this antenna has been printed on the same side of the FR4 PCB with a thickness of $h = 1.55$ mm, relative permittivity of $\epsilon = 4.4$, and a loss tangent of $\tan\delta = 0.018$. The designed antenna was etched onto FR4 PCB having the size of 26 mm $\times$ 29 mm $\times$ 1.55 mm. As can be seen in Figure 6.2(a), the slot has the shape of complementary planar monopole antenna surrounded by the ground plane. It should be noted that the antenna is positioned symmetrically with respect to the z axis.

Before continuing with the rest of the design procedure, let's note that the above antenna element is a linearly polarized antenna.[5] Specifically, its far-field electric field will be in the z direction. Although we are not concerned with the far-field zone of the antenna, we thought that starting with a linearly polarized antenna in the z direction may correspond to a more dominant z component in the near-field zone, thus, making the final antenna element more

[5] Note that the polarization is a far-field quantity.

suitable for 2D TM$_z$ MWT.[6] We do not know if such correspondence exists, but, this was a speculation that seemed to be reasonable. (We will return to this topic in Section 6.4.4.) Also, noting that we are interested in 2D TM$_z$ MWT, if this antenna is to be used in an MWT system, the antenna needs to be positioned in the imaging chamber in such a way that the coaxial cable is perpendicular to the imaging plane so as to have E_z perpendicular to the imaging plane.

Now, we revisit the idea of using a metallic cavity that was presented in [83] and described above. We used this metallic cavity in conjunction with the antenna element of [3]. This metallic cavity, which is located as an open box below the monopole-like slot antenna, can be best seen in Figure 6.5(a). Having seen the actual fabrication of this metallic cavity, Figure 6.2(b), which also shows this metallic cavity in the HFSS software, can now be better understood. However, as opposed to [83], we do not use a radio frequency absorber to fill the space between the metallic cavity and the monopole-like slot antenna. Initially, we chose to not include the absorber so as to increase the efficiency of the final antenna element. However, we later speculated that we might be able to use the reflection off the metallic cavity to strengthen the near-field focusing in the forward direction of the antenna. Therefore, we chose to not include any absorbers between the metallic cavity and the slot antenna. This resulted in two different issues. First, the resulting antenna lost its UWB properties. At this point, we tried to optimize the resulting antenna using the HFSS software so as to improve its bandwidth. The parameters over which the bandwidth of the antenna was optimized were: the height of the metallic cavity's walls, separation between two vertical stubs of the fork-shaped feed, length of the vertical stubs, the length of the folded ground strips, and the separation between the monopole-like slot antenna and the cavity. Based on this optimization, the resulting bandwidth was improved. Of course, this improved bandwidth did not make the resulting antenna UWB; but it was sufficient to operate the antenna in multiple fre-

[6] TM$_z$ indicates that the only component of the electric field is in the z direction; i.e., $\boldsymbol{E} = E_z\hat{z}$.

quencies of operation where the lowest frequency and the highest frequency are reasonably apart. To be more accurate, with this modification, we have lost some midband frequencies of the UWB range. The second issue with not including absorbers between the cavity and the monopole-like slot antenna was how to hold these two different items together. To this end, we used Styrofoam to hold the cavity and the monopole-like slot antenna together. This can be best seen by looking at the space below the fabricated antenna in 6.5(a). We note that Styrofoam has a relative permittivity of almost $\epsilon = 1$ and it therefore almost acts like air in the interaction with electromagnetic waves.[7]

At this point, we decided to add a dielectric superstrate to the antenna so as to make its near-field distribution more focused. (As noted earlier, the idea of using a dielectric superstrate to enhance the near-field focusing abilities was inspired by the work reported in [55].) To do this, we first had to answer two questions: (1) what kind of dielectric material should be used? and (2) where should we place this dielectric material? Regarding the first question, we speculated that a dielectric material which has a larger permittivity as compared to FR4, which was used in the antenna, will be more appropriate as a larger permittivity material tends to keep the electric fields around itself, thus, somehow helping toward focusing. Also, it is desirable for this dielectric material to be low loss so as to not reduce the overall efficiency. We, therefore, decided to choose a pieces of RT/duroid 6010 that has a relative permittivity of $\epsilon = 10.2$, and a loss tangent of $\tan\delta = 0.0023$. (The standard thickness of this dielectric material is 1.9 mm. This thickness is, thus, chosen in this work.) Now, to answer the second question, it is obvious that this dielectric material needs to be located above the antenna; i.e., in the positive x direction. But we should now answer at what distance this dielectric superstrate needs to be placed, and also what the dimensions of its surface area need to be. Regarding the surface area of this superstrate, we decided to choose its surface

[7] We have measured the permittivity of the utilized Styrofoam by the Agilent permittivity measurement kit to confirm that its permittivity is close to one. The maximum frequency of operation for the utilized kit was 6 GHz; therefore, we were able to confirm this up to 6 GHz.

area to be a rectangle covers the slot of the antenna, as shown in Figure 6.2(b). We know need to address the separation between this superstrate and the monopole-like slot antenna. To this end, the bandwidth of the antenna was optimized over the following parameters: separation between the superstrate and the monopole-like slot antenna, separation between the vertical stubs of the fork-shaped feed, length of the vertical stubs, the separation between the metallic cavity and the monopole-like slot antenna, the height of the cavity's walls, and the tapering of the ground strips. Therefore, as can be seen, to find an appropriate separation between the superstrate and the antenna, several other parameters, which have been optimized in the previous step, need to be optimized once more. It should be noted that we were not able to have this superstrate in direct contact with the monopole-like slot antenna due to significant degradation in the bandwidth of the resulting antenna. Therefore, an optimized distance was found for this superstrate.

At this point, we noticed that the near-field distribution of the antenna in the positive x direction becomes more focused due to the presence of this superstrate. Based on this observation, the following idea came to mind. Let's also try to focus the near-field distribution of the monopole-like slot antenna in the negative x direction using the same technique with the hope that this focused near-field distribution will be reflected back by the metallic cavity toward the forward direction of the antenna, thus, hoping to strengthen the effect of the focused near-field distribution in the positive x direction. To try this idea, we placed the same RT/duroid 6010 dielectric material between the monopole-like slot antenna and the cavity. (See Figures 6.2(b) and 6.4.) This dielectric was placed directly beneath the superstrate. Now the question to be answered is at what separation from the monopole-like slot antenna this dielectric needs to be placed. To answer this question, the bandwidth of the resulting antenna was optimized over the following parameters: separation of this dielectric material, which is located beneath the slot, from the slot, separation of the superstrate from the slot, and the height of the cavity's wall. As can be seen again, some of the parameters that have

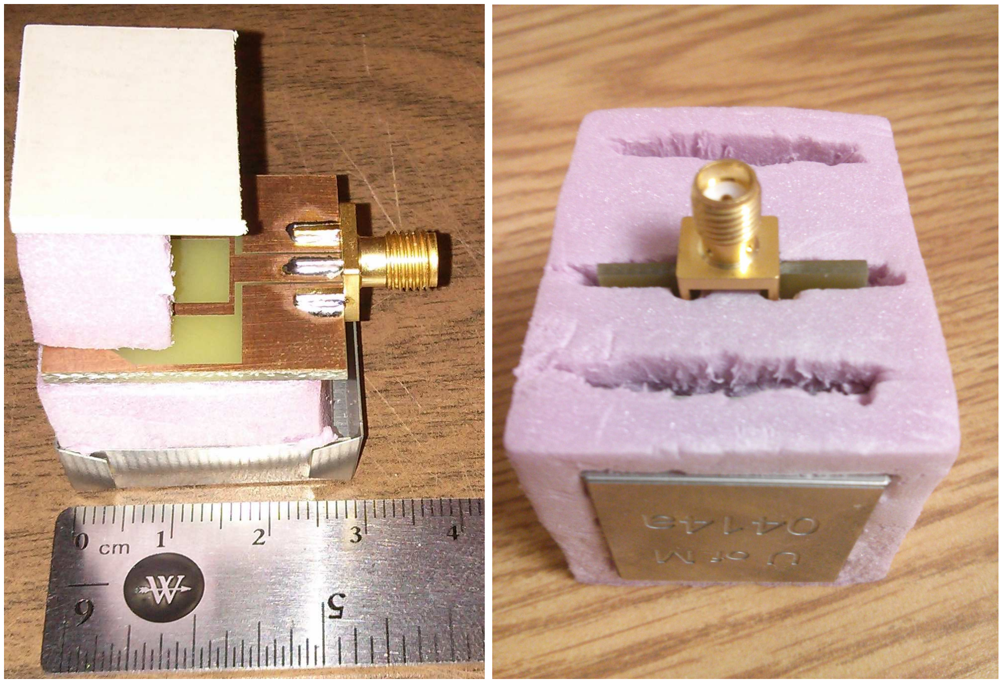

(a) Demonstration model (b) Final fabricated antenna

Fig. 6.5: (a) The demonstration of the final antenna. This demonstration shows the superstrate on top of the monopole-like slot antenna held with another piece of Styrofoam, and the open metallic cavity beneath the monopole-like slot antenna which is attached to the antenna with a piece of Styrofoam. Note that the dielectric material between the metallic cavity and the monopole-like slot antenna is not visible in this figure. (b) The final fabricated antenna that has been measured. The whole antenna is covered with the Styrofoam box to enclose the followings: (the order of listing starts from the bottom of the figure toward its top) metallic cavity, an opening to place the dielectric material between the cavity and the monopole-like slot antenna, an opening to place the monopole-like slot antenna, and the final opening to place the superstrate.

been already optimized were optimized again.

This concludes our design procedure. The final antenna is shown in Figure 6.5(b). As can be seen, the whole antenna is covered in a Styrofoam box with three openings, the middle one to fit the monopole-like slot antenna, and the other two to fit the RT/duroid 6010 dielectric material. We now list the final dimensions of the antenna in Table 6.1. The variables in this Table refer to the notation used in Figures 6.3 and 6.4.

Tab. 6.1: The dimensions of the final antenna element.

Parameter	**Value [mm]**
Ws	24
Ls	18
$L2$	10.5
$L3$	7.7
$L4$	6.1
Wg	1
Lf	9.5
Sf	8.4
Wfh	0.5
Wfv	1.6
Wf	3.6
g	0.8
S	0.35
Ds	6.5
Hc	7.9
Hs	16.5
d	18.5
h	1.55
Thickness of RT/duroid 6010	1.90
Width of RT/duroid 6010	24
Length of RT/duroid 6010	19

6.4 Simulation and Measurement Results

Before starting this section, let's present two different terms which will be used in the rest of this chapter. We will refer to the monopole-like slot antenna with the metallic cavity and the two pieces of RT/duroid 6010 dielectric material as the "covered monopole-like slot antenna". We then refer to the monopole-like slot antenna without the metallic cavity and without the two RT/duroid 6010 dielectric materials simply as the "monopole-like slot antenna". In both of these two antennas, the geometrical parameters of the slot and the fork-shaped feed are the same, and correspond to the modifications described in Section 6.3, which has been listed in Table 6.1. In this section, the simulation and measurement results of these two antennas will be presented. (All of the antenna simulations were carried out by using the ANSYS HFSS software.)

The near-field of these two antennas were measured with a planar near-field range (PFNR). This PNFR, which is shown in Figure 6.6(a), was manufactured by the Nearfield Systems Inc. (NSI). In this PNFR, the antenna under test (AUT) is stationary, and the measurement probe, which resides in the near-field zone of the AUT, moves in front of the AUT to collect its near fields. (The AUT and the probe are both connected to a vector network analyzer.) The measurement probe, which can be seen in Figure 6.6(b), is a WR90 open-ended waveguide probe with tapered ends.[8] Although the vector network analyzer (VNA) of this PNFR can operate up to 40 GHz, we only had access to X-band (8.2 GHz- 12.4 GHz) probes.[9]. In the University of Manitoba's PNFR, the probe is capable of sweeping a scan area with the size of 0.9×0.9 m^2.[10] The NSI 2000 software is utilized in conjunction with this system to command the movement of the probe and store the data on the computer. In addition,

[8] Tapered ends are applied to the probe so as to reduce the multiple reflections between the probe and the antenna under test.

[9] It should be noted that at low frequency ranges, the mechanical stability of the system to handle the weight of the probe can be a limiting factor.

[10] The data collection on this scan area is performed on a rectilinear grid.

this software also performs probe correction.[11] Finally, we note that the S_{11} measurements of these two antennas were performed by using Anritsu ME7808A VNA, as shown in Figure 6.6(c).

6.4.1 $|S_{11}|$ measurements

In this section, the simulated and measured $|S_{11}|$ of the monopole-like slot antenna and the covered monopole-like slot antenna will be presented. Figure 6.7(a) shows the simulated and measured $|S_{11}|$ of the monopole-like slot antenna, while Figure 6.7(b) represents the simulated and measured $|S_{11}|$ of the covered monopole-like slot antenna. Before showing the results, we note that the frequencies that correspond to $|S_{11}| \leq -10$ dB are often assumed as the impedance bandwidth of the antenna; thus, they can be used for inversion. However, it should be noted that this requirement might be too strict for imaging applications.

Comparing Figures 6.7(a) and 6.7(b) shows that some of the impedance bandwidth of the monopole-like slot antenna has been sacrificed toward its evolution into the covered antenna. In particular, the frequency band between 4.9 GHz to 8.1 GHz has been lost in the covered monopole-like slot antenna. Now, let's focus on Figure 6.7(a). As can be seen, the simulated $|S_{11}|$ does not have an impedance bandwidth from 3.45 GHz to 4.42 GHz. We note that this is not in contradict with the result presented in [3]. This is due to the fact that some of the geometrical parameters of this antenna has been modified as noted in Section 6.3. On the other hand, the measured $|S_{11}|$ between 3.45 GHz to 4.42 GHz almost exhibits an impedance bandwidth based on $|S_{11}| \leq -10$ dB criterion. This discrepancy between the measured data and the simulated data might be explained as follows. The monopole-like slot antenna has, to some extent, omnidirectional properties specially in this frequency range.

[11] Probe correction is necessary to be applied to the measured near-field data since the receiving properties of the probe with respect to the AUT will change as the probe moves on the scan plane.

(a) Planar near-field range

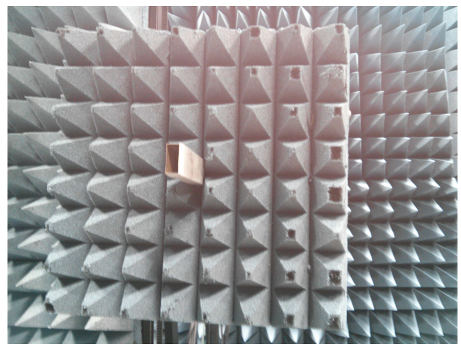

(b) Open-ended waveguide probe with tapered ends

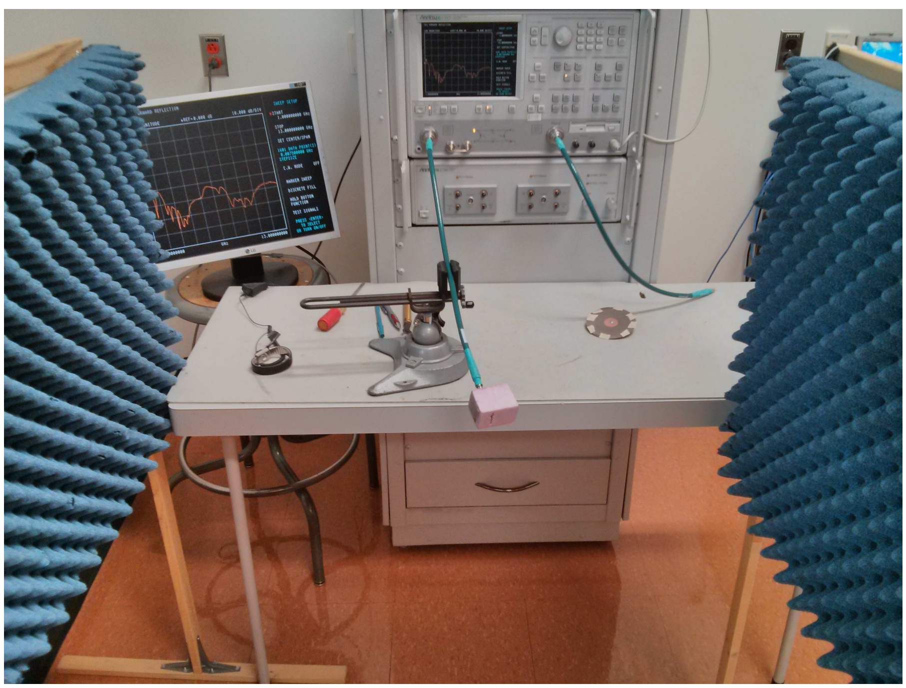

(c) VNA setup for S_{11} measurements

Fig. 6.6: (a) Planar near-field range: The antenna backed with pyramidal absorbers is the measurement probe. The other antenna (in this case, the covered monopole-like slot antenna) is the antenna under test. Absorbers have been taped on the tower that holds the antenna under test (b) Closer view of the measurement probe, and (c) the VNA setup for performing S_{11} measurements.

Therefore, our measurement setup, which is shown in Figure 6.6(c), might not be appropriate for performing $|S_{11}|$ measurements. This is due to the fact that the antenna under test can "see" the presence of its surroundings due to its omnidirectional properties in this frequency range. Noting that our measurement setup to perform this measurement is not located in an anechoic chamber, this can potentially result in the measurement error. Now, let's also take a look at Figure 6.7(b). As can be seen the simulation and measurement results match somehow better in this case.[12] This could be due to the fact that the covered monopole-like slot antenna is more focused in the forward direction, thus, the presence of scatterers in the room (e.g., the VNA itself) will be seen by this antenna to a less extent compared to the other antenna.

Finally, by looking at the measured results of the covered monopole-like slot antenna, and by relaxing the definition of the impedance bandwidth to $|S_{11}| \leq -8$ dB, the covered monopole-like slot antenna has the following impedance bandwidth of operation: 2.34 GHz to 5.04 GHz and 8.06 GHz to 13 GHz. Therefore, this covered monopole-like slot antenna, if used in an MWT system, can support multiple-frequency inversion. It is also worthy to note that these frequencies of operation span a very wide range (compare 2.34 GHz with 13 GHz). Therefore, we speculate that it is more likely for this antenna to provide more independent information regarding the OI compared to another antenna that provides multiple frequencies of operation but within a less wider range.

6.4.2 Parametric studies

In this section, we study the effect of some important parameters on the impedance bandwidth of the covered monopole-like slot antennas. Due to the fact that it is difficult to fab-

[12] Note that the simulated and measured values in the high frequency range of the covered antenna are already almost less than -10 dB; thus, their discrepancy is not as important as the one in the low frequency range of the other antenna.

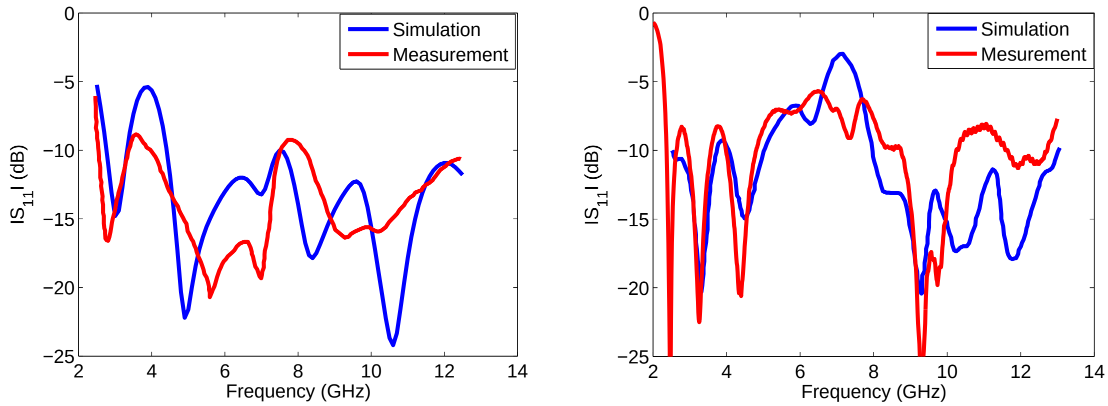

(a) Monopole-like slot antenna (b) Covered monopole-like slot antenna

Fig. 6.7: Simulated and measured $|S_{11}|$ for the (a) monopole-like slot antenna, and (b) covered monopole-like slot antenna. The measurement setup is shown in Figure 6.6(c).

ricate the antenna for every parameter change, we only show the simulation results in these parametric studies. The five parameters to be studied herein are: the separation between the slot and the superstrate (d), the height of the metallic cavity's walls (Hc), the length of the fork-shaped feed's vertical stubs (Lfv), the separation between the fork-shaped feed's vertical stubs (Sf), and the horizontal length of the folded ground strip ($L2$). It should be noted that during the optimization of the covered monopole-like slot antenna, several other parameters have also been taken into account in the optimization. However, herein, we focus on these five parameters due to their importance.

Before continuing our discussion regarding these parametric studies, we note that there are two issues with the present study. First, if one wants to optimize the impedance bandwidth of the antenna over these five parameters, the correct approach would be to optimize the impedance bandwidth simultaneously over these five parameters. However, currently, due to the computational complexity of this problem, this approach will suffer significantly from computer run time. (Note that this optimization needs to be done over a wide frequency range.) Therefore, at each time, we choose to vary one parameter while keeping the rest fixed. (The fixed values are those reported in Table 6.1.) Therefore, the final design that we have will be a reasonable design, but may not be the best possible. The second issue is that we would ideally like to optimize this antenna for having a focused near-field distribution in addition to having a reasonable impedance bandwidth over these parameters. This approach could also be extremely computationally expensive. Due to this, we assumed that the presence of the superstrate will help the near-field focusing abilities, and then we tried to optimize the impedance bandwidth, which is the necessary condition for the operation of the antenna. (As will be shown later, the presence of the superstrate, in fact, helps the focusing ability of this antenna.)

We now show the results of our parametric studies in Figure 6.8 for the covered monopole-like slot antenna. The effect of the separation between the slot and the superstrate (d) on the impedance bandwidth has been illustrated in Figure 6.8(a). As can be seen in this figure, this separation influences the higher range of the frequency spectrum more than the lower range. It is, of course, expected since in the higher frequency range, this change of separation translates itself into more significant change in the electrical separation. Figure 6.8(b) shows the effect of the height of the metallic cavity's walls (Hc) on the impedance matching of the antenna. The effects of the length of the vertical stubs (Lfv) and the the separation between them (Sf) have been shown in Figure 6.8(c) and (d) respectively. As can be seen, these parameters have effects on lower and higher bands. Finally, the effect of the horizontal folded ground strips length ($L2$) has been shown in Figure 6.8(e).

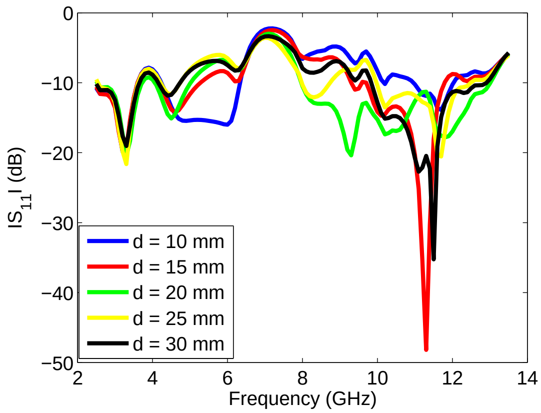

(a) antenna and superstrate separation

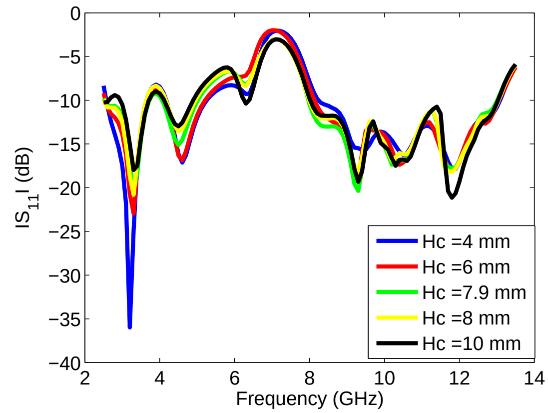

(b) Cavity height

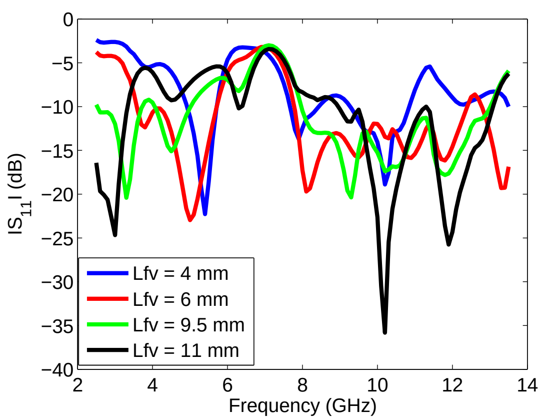

(c) Fork-shaped feed vertical length stubs

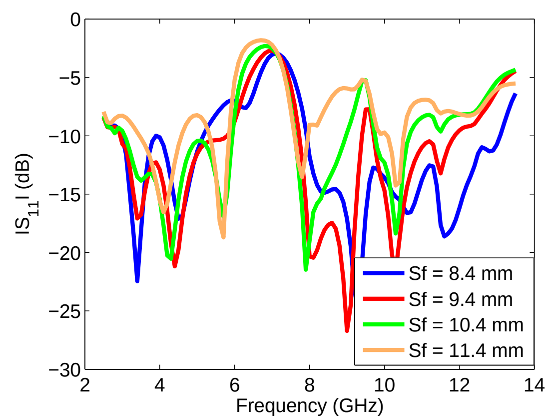

(d) Fork-shaped feed vertical stubs separation

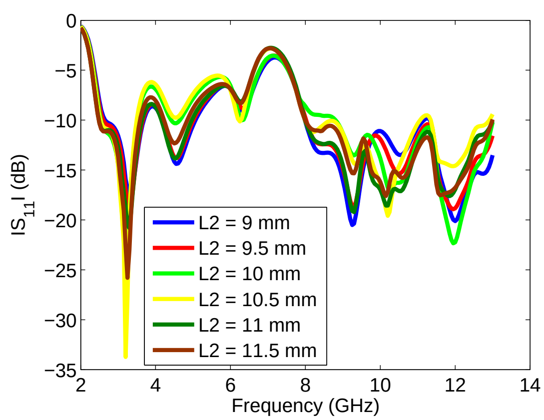

(e) Folded ground strip horizontal length

Fig. 6.8: Parametric studies of the covered monopole-like slot antenna (a) separation between the slot and the superstrate, (b) cavity height (c) length of the vertical stubs, (d) separation between the vertical stubs, and (e) horizontal length of the folded ground strip.

6.4.3 Near-field distribution

In this section, we first start with presenting the near-field measurements from the monopole-like slot antenna and the covered monopole-like slot antenna. As noted earlier, these near-field measurements are performed with a PNFR; thus, the measurement probe collects the near-field of the antenna under test on a plane in the near-field zone of the antenna. Based on the coordinate system shown in Figure 6.2, the measurement plane will be in the $y-z$ plane. Herein, for each of these two antennas we only show five sets of measurements, each of which corresponds to a specific distance[13] from the slot to the measurement plane. These distances are 5 cm, 7 cm, 10 cm, 12 cm, and 14 cm. The size of the measurement plane for each of these distances are chosen in such a way that all these measurement planes will be within the same solid angle from the center of the antenna. (This solid angle represents a cone with the apex angle of $60°$.) Therefore, the farther the measurement plane is from the antenna, the large the measurement plane will be. For each of these measurement planes, we show the near-field data at four different frequencies within the X-band; namely, 8.6 GHz, 9 GHz, 9.6 GHz and 10 GHz.[14]

For each set of measurements, the PNFR collects two components of the electric field at each point on the rectilinear grid of the measurement plane. Based on the coordinate system shown in Figure 6.2, these two components of the electric fields are E_z and E_y, which are, of course, the tangential components of the electric fields on the measurement plane.[15] Since

[13] Based on the coordinate system shown in Figure 6.2, these distances are in the positive x direction from the antenna under test.

[14] As noted in Section 6.4.1, the measured impedance bandwidth of the covered monopole-like slot antenna has two bands: 2.34 GHz to 5.04 GHz and 8.06 GHz to 13 GHz. Due to not having access to the probes at the lower frequency range, we were not able to measure the near-field distribution at the lower frequency range. Also, the utilized PNFR system might have mechanical stability issues with the lower range; compare the weight of WR90 probe (8.2 GHz to 12.4 GHz) which is about 0.5 Kg with WR340 probe (2.2 GHz to 3.3 GHz) which is about 4.5 Kg. (The weights have been taken from Nearfield Systems Inc.'s website.)

[15] The PNFR is capable of performing these two electric field measurements due to its ability to rotate the probe $90°$.

the scope of this thesis is 2D TM_z MWT, we only show the E_z measurements here.[16] Also, to be able to compare different near-field measurement plots better, all the plots are normalized and the lower magnitude has been truncated to -10 dB.

As can be seen in Figure 6.9 to Figure 6.13, the covered monopole-like slot antenna creates a more focused beam in the measurement plane as compared to the monopole-like slot antenna. Also, a general trend that can be seen for both of these antennas is that the illumination area will become larger and larger as the distance of the probe from the antenna increases. The other item that should be noted here is the fact that the sampling resolution in the measurement planes corresponding to different distances are different. This is due to the fact that the size of the measurement planes are different. (For a given measurement plane size and also the solid angle of interest, the NSI 2000 software chooses an appropriate sampling resolution.)

Based on Figure 6.9 to Figure 6.13, we have shown that the covered monopole-like slot antenna has a more focused near-field distribution in the $y - z$ plane as compared to the monopole-like slot antenna. As noted in Section 2.7.3, it is important for the antenna to be used in a 2D MWT system to mostly see the 2D imaging plane (in our case, $x - y$ plane), and not the 3D effects of the OI and the imaging chamber. This is due to the fact that 3D effects when incorporated into 2D MWT will contribute toward the overall noise of the data, thus, degrading the achievable resolution based on the discussion presented in Section 3.4. Now what remains is the measurement of the near-field of these two antennas in the imaging plane; i.e., $x - y$ plane. However, this is not directly possible with the PNFR as the PNFR is capable of performing measurements only in the $y - z$ plane.

Now, let's address how we obtained the near-field data of these two antennas in the $x - y$

[16] Note that the E_z component is perpendicular to the imaging domain which is assumed to be in the $x - y$ plane.

plane. To this end, we have measured the near-field data of each antenna at 23 different distances; namely, starting from 5 cm away from the antenna to 16 cm with the step of 5 mm within the solid angle which has an apex of $60°$. Of course, these 23 sets of near-field measured data are performed on planes parallel to the $y-z$ plane.[17] Having these 23 different sets of measurements, we can then extract the measurements that correspond to the points located on the $x-y$ plane. However, as noted above the sampling resolutions in different measurement planes are not identical. Therefore, we used *interpn* MATLAB function to interpolate these measurements into identical sampling grid. Based on this approach, we were able to find the near-field data in the $x-y$ plane. This measured near-field data at 9 GHz has shown in Figure 6.14. The domain over which this near-field data has been obtained is $x \in [5\ 16]$ cm and $y \in [-5.5\ 5.5]$ cm. As can be seen, the covered monopole-like slot antenna seems to have slightly more focused near-field beam in the $x-y$ plane as compared to the monopole-like slot antenna. We note that the enhanced focusing is more clear in the measurement planes parallel to the $y-z$ plane as compared to the plot in the $x-y$ plane. This might be due to the fact that the chosen $x-y$ plane has a smaller width (11 cm). This is in contrast to the $y-z$ measurement planes whose width varies from about 11 cm to 20 cm. Note that to obtain the near-field data over the $x-y$ plane, we had to combine all these $y-z$ near-field data. Therefore, the width of the resulting $x-y$ near-field data will be the same as the smallest width in the $y-z$ measurement planes. Also, it should be noted that the interpolation used to obtain the near-field data over the $x-y$ plane might have some smoothing effects on the data, thus, not showing the focusing of the antenna sufficiently well.

Due to the fact that the size of the $x-y$ plane over which the measured data is reported cannot be very large, and also due to the fact that the interpolation is used to report the near-field data over the $x-y$ plane, we decided to also investigate the near-field data over a larger

[17] These 23 measurement planes will be $x = 5$ cm, $x = 5.5$ cm, $x = 6$ cm, $\cdots$, $x = 16$ cm.

$x - y$ plane using the ANSYS HFSS simulation. The $x - y$ domain over which we chose to show this simulation is $x \in [0\ 20]$ cm and $y \in [-10\ 10]$ cm. Figures 6.15 and 6.16 show this simulation for two different frequencies: 4 GHz and 9 GHz. As expected, the covered monopole-like slot antenna creates a more focused near-field distribution in this domain.

6.4.4 Electric field's vector components

The above results considered that component of the electric field that will be used for 2D TM$_z$ MWT; namely E_z component. To make the 2D TM$_z$ approximation as accurate as possible, we'd like to have E_x and E_y components of the vector electric field as small as possible in the imaging chamber.[18] This will result in less modeling error, and therefore improve the overall signal-to-noise ratio of the MWT data. Herein, we show the three components of the vector electric field on a semi-circle in front of the antenna in the $x - y$ plane. This will be shown for two different radii, namely 7 cm and 10 cm, at two different frequencies, namely 9 GHz and 10 GHz. As can be seen in Figures 6.17 and 6.18, the covered monopole-like slot antenna did not increase the magnitudes of E_x and E_y with respect to the desired component E_z as compared to the monopole-like slot antenna (maybe, except Figure 6.18(b)). In fact, as can be seen in these two figures, the covered antenna somehow improved the relative magnitude of E_z with respect to E_x and E_y.

This concludes the presentation of the covered monopole-like slot antenna and its comparison with the monopole-like slot antenna.

[18] It should be noted that we do not use co-pol and x-pol components in this framework as these are far-field terms, and are, therefore, not applicable to this study.

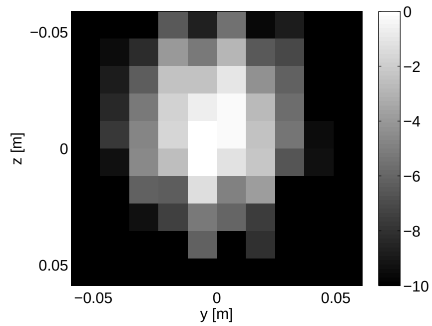

(a) 8.6 GHz

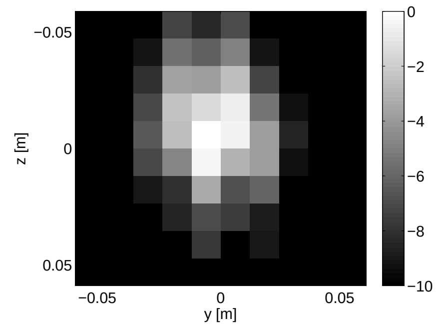

(b) 8.6 GHz

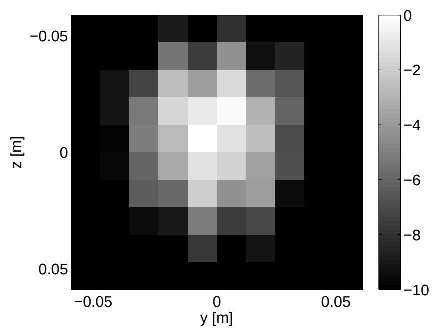

(c) 9 GHz

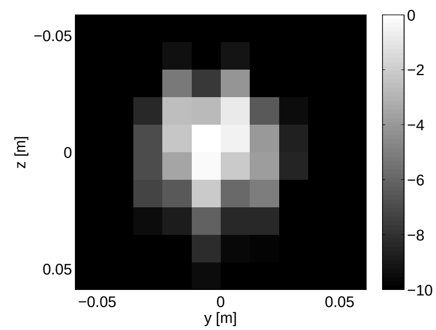

(d) 9 GHz

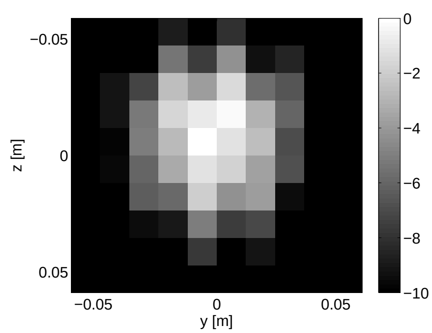

(e) 9.6 GHz

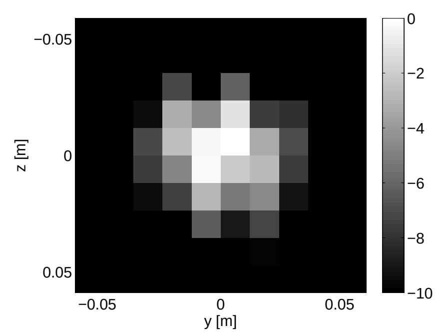

(f) 9.6 GHz

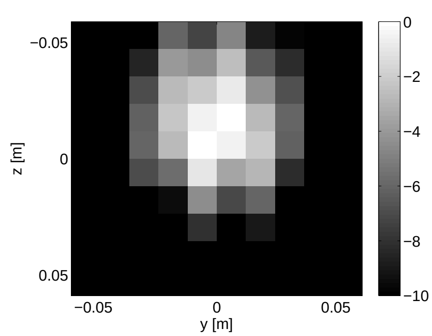

(g) 10 GHz

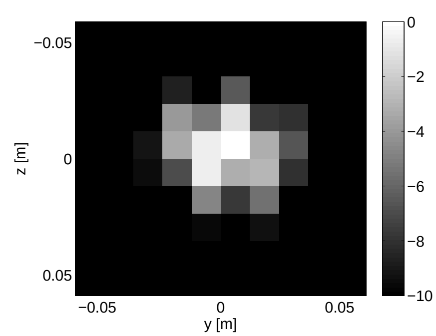

(h) 10 GHz

Fig. 6.9: [Left] monopole-like slot antenna and [Right] covered monopole-like slot antenna. The measured near-field distribution of the antenna when the measurement plane is 5 cm away from the antenna at four different frequencies. (The measured component is E_z.)

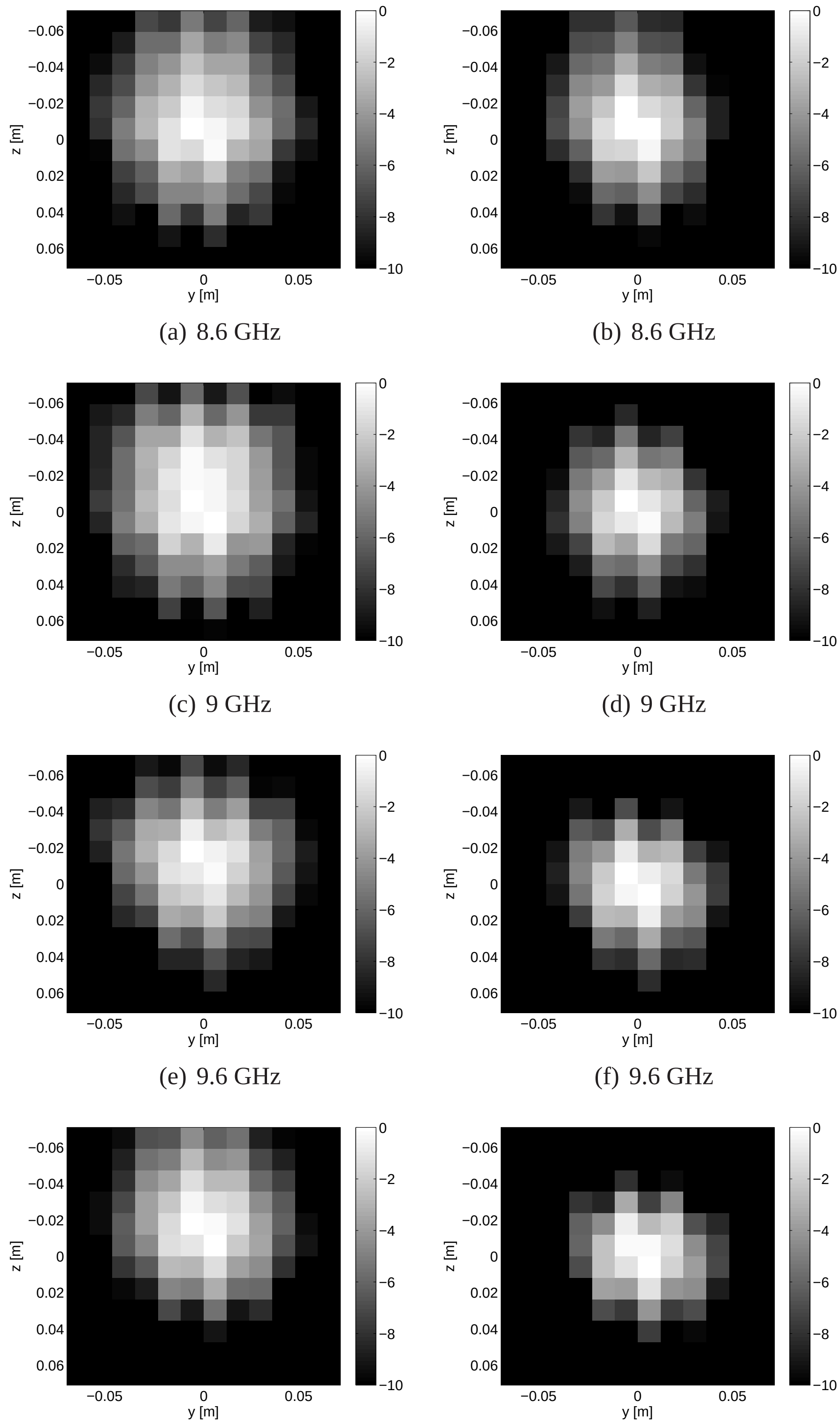

(a) 8.6 GHz (b) 8.6 GHz

(c) 9 GHz (d) 9 GHz

(e) 9.6 GHz (f) 9.6 GHz

(g) 10 GHz (h) 10 GHz

Fig. 6.10: [Left] monopole-like slot antenna and [Right] covered monopole-like slot antenna. The measured near-field distribution of the antenna when the measurement plane is 7 cm away from the antenna at four different frequencies. (The measured component is E_z.)

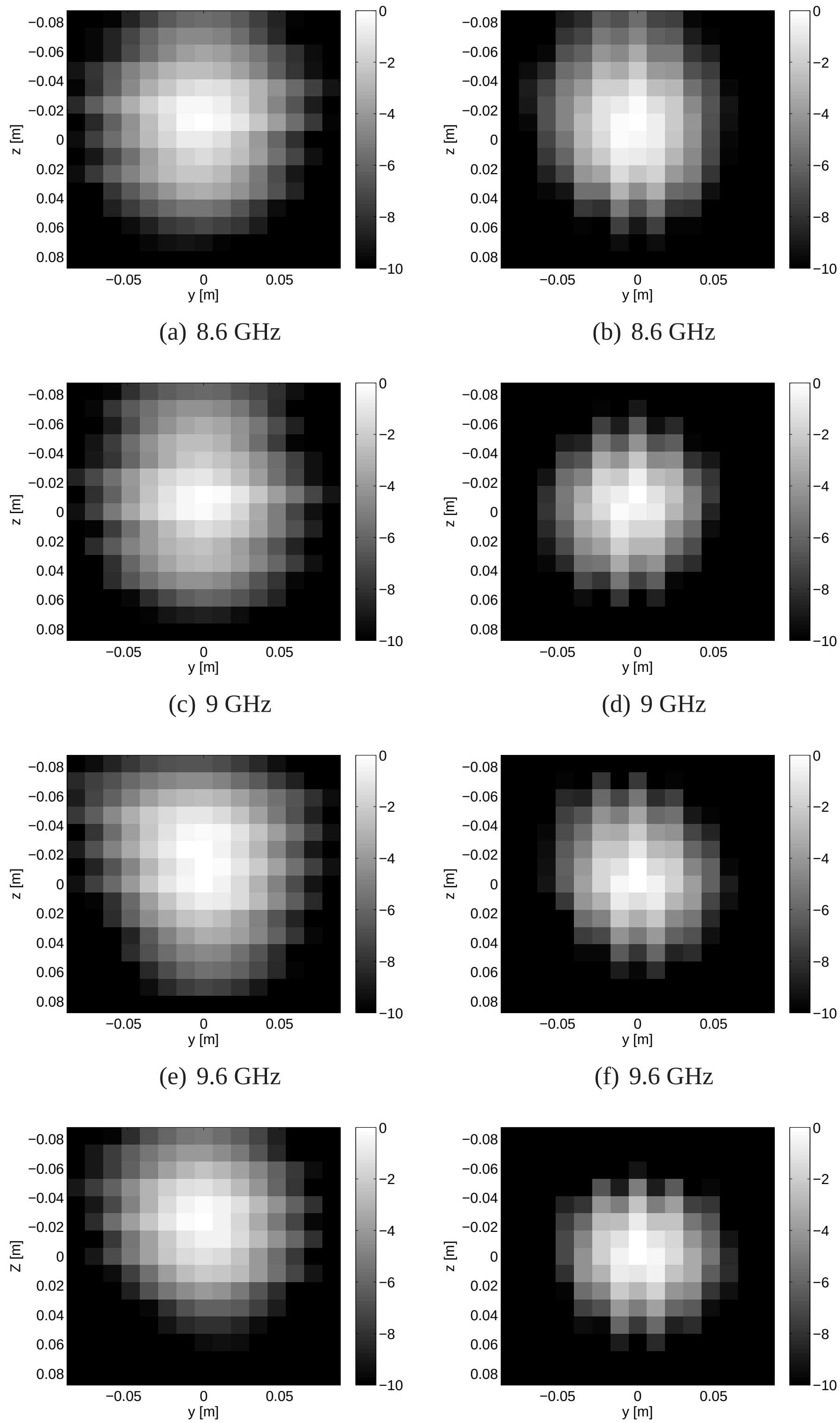

(a) 8.6 GHz (b) 8.6 GHz

(c) 9 GHz (d) 9 GHz

(e) 9.6 GHz (f) 9.6 GHz

(g) 10 GHz (h) 10 GHz

Fig. 6.11: [Left] monopole-like slot antenna and [Right] covered monopole-like slot antenna. The measured near-field distribution of the antenna when the measurement plane is 10 cm away from the antenna at four different frequencies. (The measured component is E_z.)

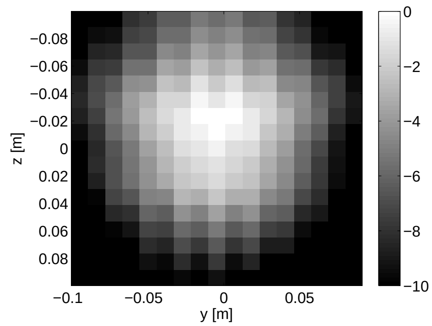

(a) 8.6 GHz

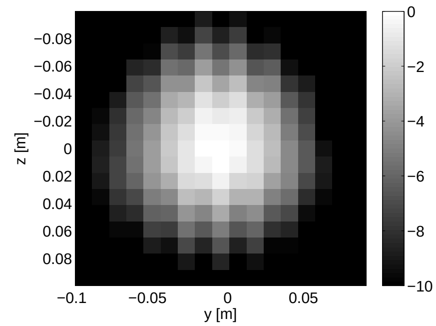

(b) 8.6 GHz

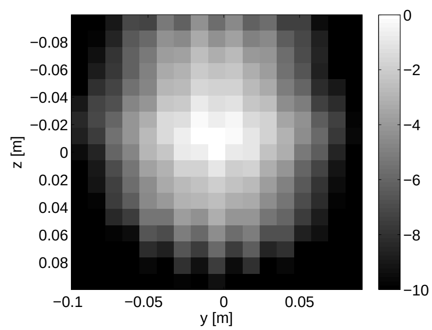

(c) 9 GHz

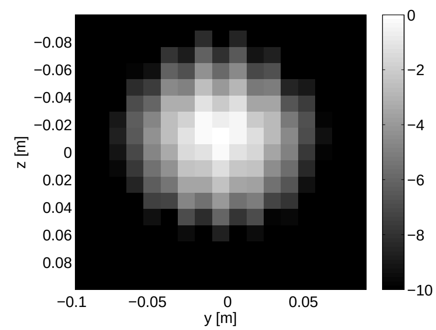

(d) 9 GHz

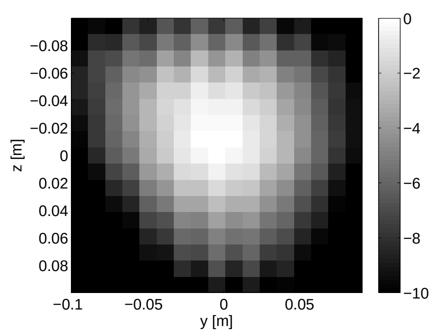

(e) 9.6 GHz

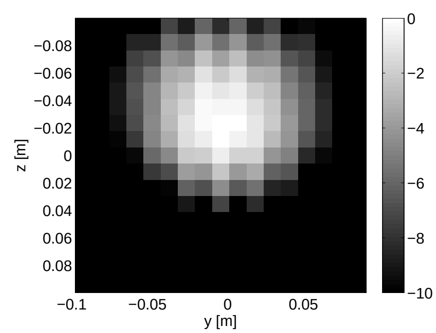

(f) 9.6 GHz

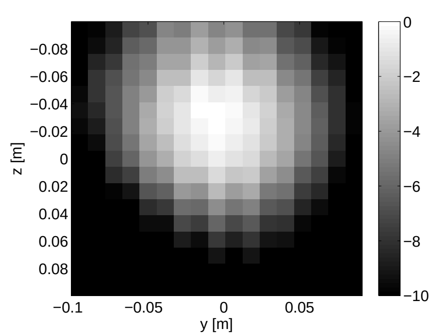

(g) 10 GHz

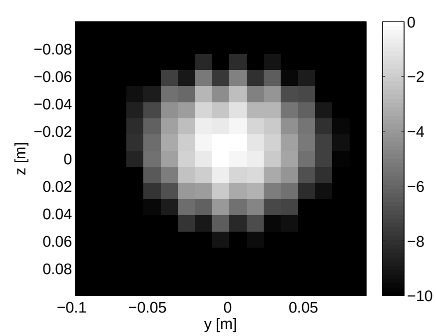

(h) 10 GHz

Fig. 6.12: [Left] monopole-like slot antenna and [Right] covered monopole-like slot antenna. The measured near-field distribution of the antenna when the measurement plane is 12 cm away from the antenna at four different frequencies. (The measured component is E_z.)

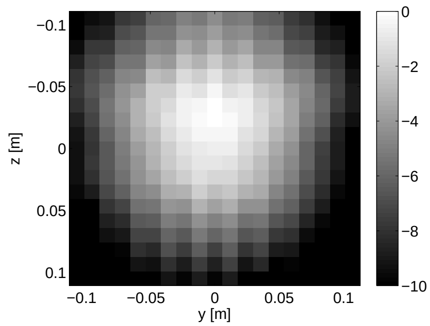

(a) 8.6 GHz

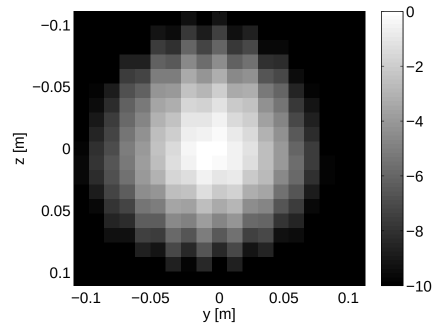

(b) 8.6 GHz

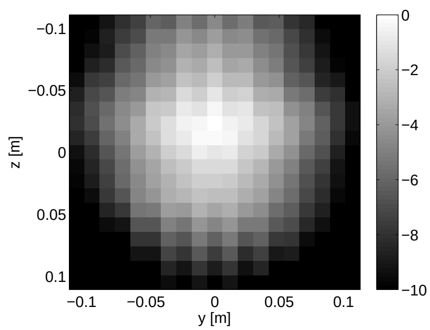

(c) 9 GHz

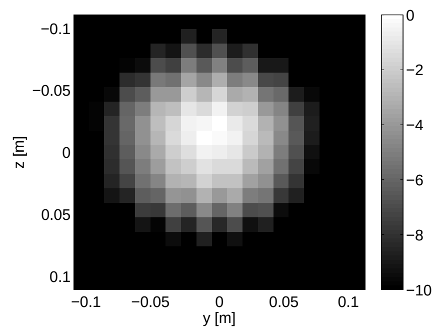

(d) 9 GHz

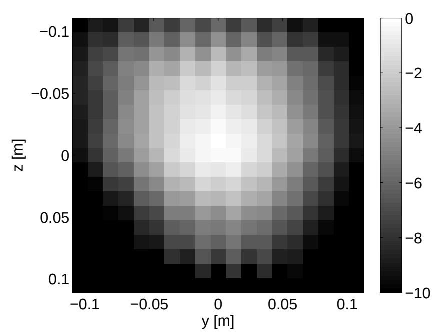

(e) 9.6 GHz

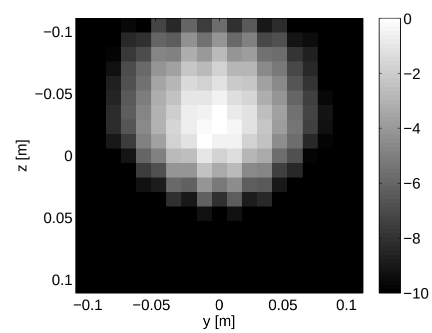

(f) 9.6 GHz

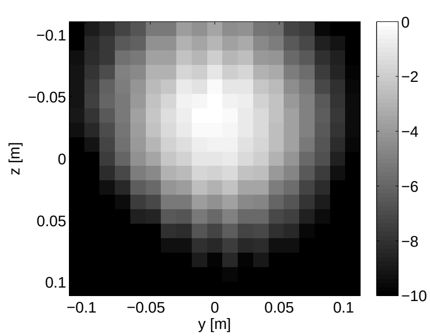

(g) 10 GHz

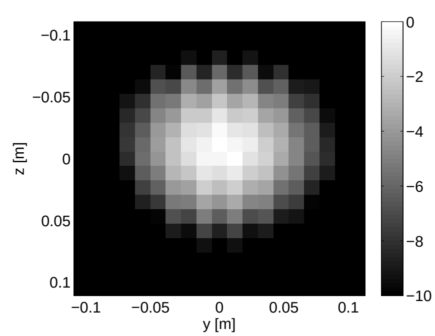

(h) 10 GHz

Fig. 6.13: [Left] monopole-like slot antenna and [Right] covered monopole-like slot antenna. The measured near-field distribution of the antenna when the measurement plane is 14 cm away from the antenna at four different frequencies. (The measured component is E_z.)

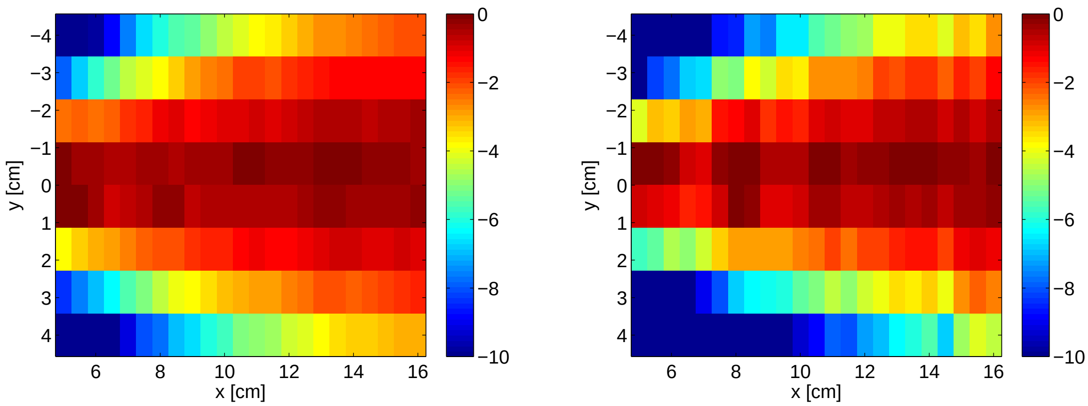

(a) Monopole-like slot antenna (b) Covered monopole-like slot antenna

Fig. 6.14: Extracted measured near-field data over the $x - y$ plane at 9 GHz for the two antennas.

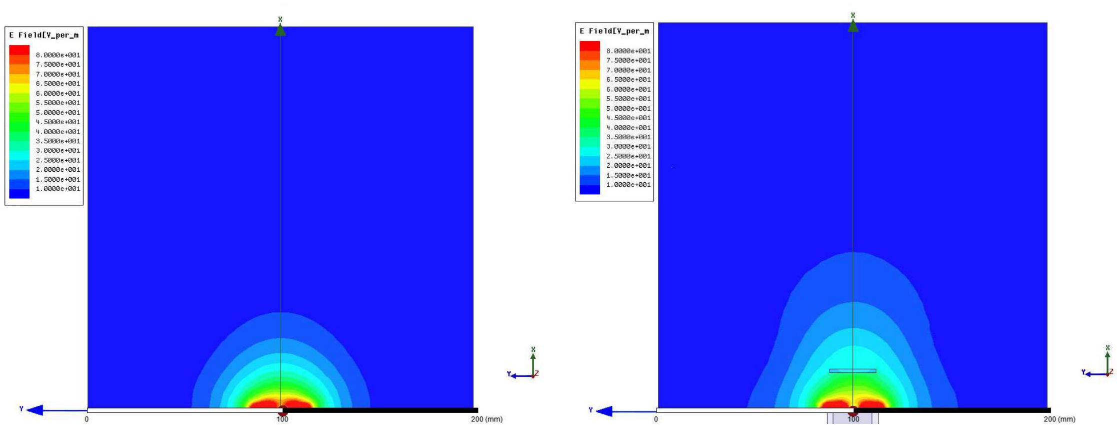

(a) Monopole-like slot antenna (b) Covered monopole-like slot antenna

Fig. 6.15: Simulated near-field data over the $x - y$ plane at 4 GHz for the two antennas.

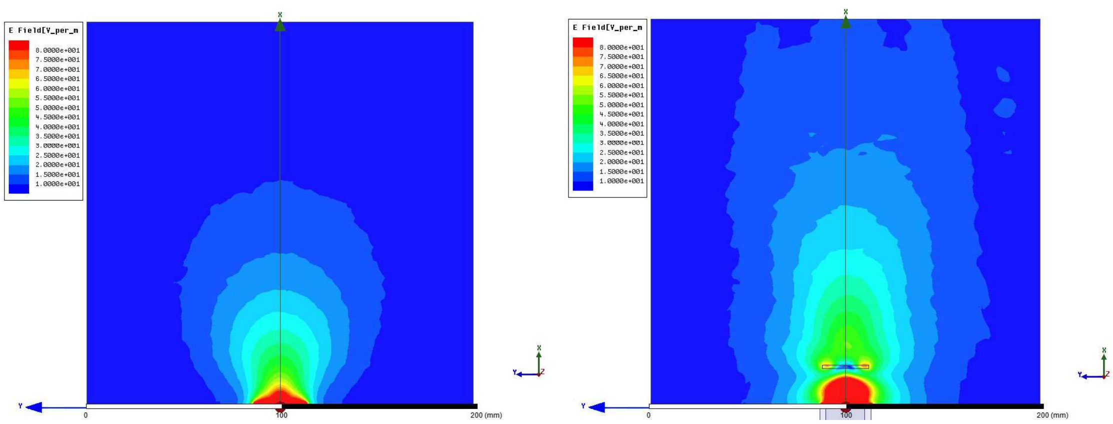

(a) Monopole-like slot antenna (b) Covered monopole-like slot antenna

Fig. 6.16: Simulated near-field data over the $x - y$ plane at 9 GHz for the two antennas.

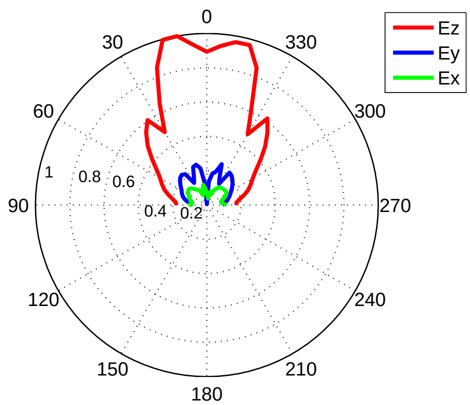

(a) Monopole-like slot antenna

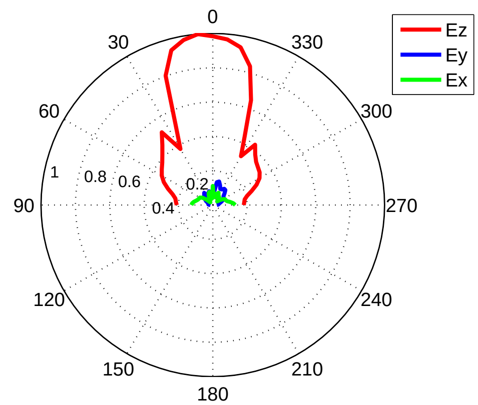

(b) Covered monopole-like slot antenna

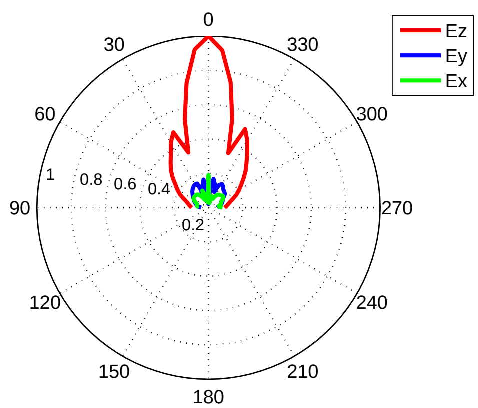

(c) Monopole-like slot antenna

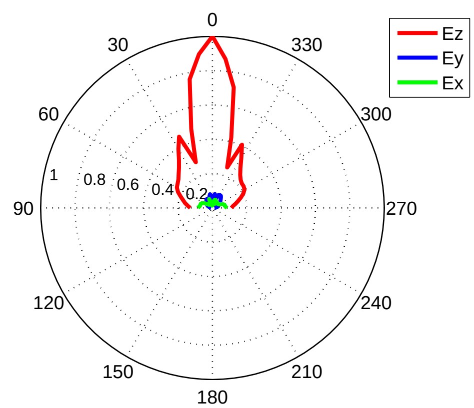

(d) Covered monopole-like slot antenna

Fig. 6.17: Simulation of the normalized magnitudes of the vector electric field components in the $x - y$ plane at 9 GHz (a)-(b) on a semi-circle of radius 7 cm, and (c)-(d) on a semi-circle of radius 10 cm.

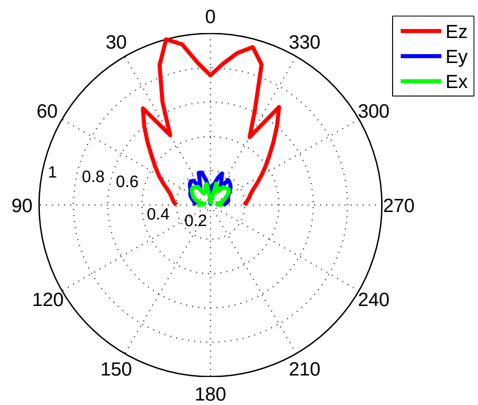

(a) Monopole-like slot antenna

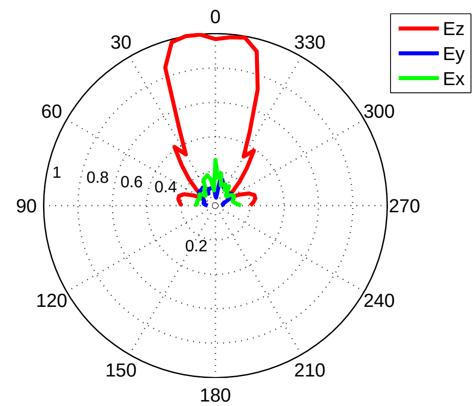

(b) Covered monopole-like slot antenna

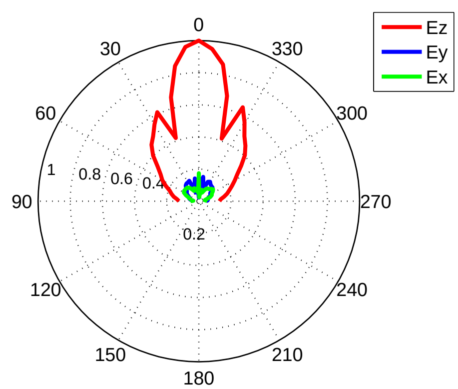

(c) Monopole-like slot antenna

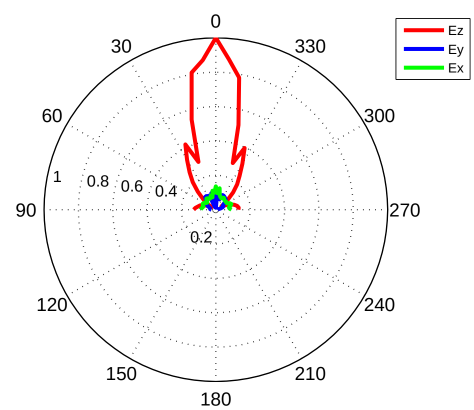

(d) Covered monopole-like slot antenna

Fig. 6.18: Simulation of the normalized magnitudes of the vector electric field components in the $x - y$ plane at 10 GHz (a)-(b) on a semi-circle of radius 7 cm, and (c)-(d) on a semi-circle of radius 10 cm.

7

Conclusions and Future Works

To conclude this thesis, let's revisit two main questions in the MWT research area: (1) what are the achievable resolution and accuracy limits?, and (2) how to enhance the achievable resolution and accuracy? Both of these two questions have been addressed in this thesis.

One of the main difficulties with answering the first question is due to the lack of a proper mathematical framework to analyze and predict the achievable resolution and accuracy from MWT. In this thesis, a mathematical framework, which does not rely on simplified scattering approximations, was presented. Based on this framework, the achievable resolution from MWT systems can be better understood. Using this framework, we investigated how several antenna-related parameters such as the frequency of operation, multiple frequencies of operation, number of transceivers, and the antennas' near-field distribution can affect the achievable resolution. This framework has the potential to help us design MWT systems in a systematic way so as to achieve the required level of resolution.

Several methods have been already suggested to address the second question. In this thesis, a novel method was presented as a new method to enhance the achievable resolution. Specifically, it was shown that the use a focused near-field distribution to irradiate the OI can enhance the achievable resolution. This observation was supported by the proposed mathematical framework, and several numerical test cases. Based on this novel method to enhance the resolution, two different approaches were investigated to implement this idea. The first, which was based on the idea of synthesized fields failed to provide the desired incident field. The second idea, which was based on designing an antenna element with focused near-field distribution, was then investigated. To this end, an existing antenna was modified and fabricated so as to make its near-field distribution more focused. The planar near-field measurement results showed that the applied modifications resulted in enhanced near-field focusing.

Therefore, this thesis contributes to the better understanding of the achievable resolution and accuracy from near-field MWT. Specifically, it shows the role that the utilized antenna elements in MWT systems can play to enhance the reconstructed image.

There are several avenues that can be considered for further investigation and future works. The short-term future work could be testing the proposed antenna in an actual MWT system. If such experimental imaging experiment is to be performed, it will also be useful to incorporate the measured near-field data of this antenna into the inversion algorithm so as to reduce the modeling error. The more important future work is to study antenna elements or radiating structures that can create more focused incident field while being able to support sufficient sampling resolution and frequencies of operation in MWT systems. From a theoretical point of view, there are still several unanswered, or not properly answered questions regarding the achievable resolution that can be investigated; e.g., the relation between the frequency of operation and resolution.

APPENDIX

A

2D TM MWT versus 3D vectorial MWT

In this Appendix, let's elaborate more on our choice of 2D TM MWT as opposed to 3D vectorial MWT. Herein, we try to justify our choice by considering the balance between the number of known and unknown quantities. To this end, let's consider an OI with the size of about $2\lambda \times 2\lambda$ where λ is the wavelength of operation. If this problem was 3D, the size of the OI would be probably $2\lambda \times 2\lambda \times 2\lambda$. Assuming 10 cells per wavelength discretization, which is a typical discretization in the computational electromagnetics, we will have 8000 voxels. (In practice, we need much finer discretization than this to capture smaller details). Now, in a 3D configuration, at each voxel, we have 4 unknowns: relative complex permittivity, and three different components of the electric field; namely, E_x, E_y, and E_z. Therefore, the total number of unknowns will be $4 \times 8000 = 32000$. Now, in an MWT system, the antennas often placed close to the OI. Therefore, in this case, it can be assumed that the antennas need to be distributed around a box of size $2\lambda \times 2\lambda \times 2\lambda$. Now, the question is how many antennas can be placed over such a small area so as to reconstruct 32000 unknowns? On the other hand, let's consider the 2D TM case. For the same example in the 2D TM configuration and again using 10 cells per wavelength discretization, we will have $20 \times 20 = 400$ cells. Now, in a 2D TM MWT system, at each pulse, we will have two unknowns: relative complex permittivity and the perpendicular component of the electric field to the imaging domain, say E_z. Therefore, the total number of unknowns to be reconstructed will be $400 \times 2 = 800$. Now, the antennas need to be distributed close to the circumference of a $2\lambda \times 2\lambda$ square so as to collect scattering data to reconstruct 800 unknowns. As can be seen, it is more feasible to have a “reasonable” balance between the number of unknowns and the number of data points in a 2D TM system as compared to a vectorial 3D system. Now, on the other hand, the disadvantage of a 2D TM system is on the assumption of the 2D wave propagation. This will exhibit itself as modeling error, and will be part of the manifest noise. Part of this error can be compensated by using calibration techniques or the use of lossy matching fluid [11, 84]. We would also like to note that even with the development of more sophisticated vectorial 3D MWT systems, 2D TM MWT systems can be still useful depending on the application. (For example, compare this with the current commercial near-field antenna measurement systems that are available in three different forms: planar, cylindrical and spherical, with the spherical range being the most accurate one.)

B

Data Misfit Cost Functional

In this Appendix, we take a look at how an MWT nonlinear inversion algorithm works. A nonlinear inversion algorithm attempts to minimize an appropriate cost functional. This appropriate cost functional is often a regularized form of the discrepancy between the measured data and the simulated data due to a predicted contrast profile. This discrepancy is often referred to as the data misfit cost functional. This data misfit cost functional may be written as

$$\mathcal{C}^{LS}(\chi) = \sum_{\gamma=1}^{nf} \xi_\gamma \frac{\sum_{\eta=1}^{nRx} \sum_{\zeta=1}^{nTx} \left|\left| E^{\text{meas}}_{\gamma,\eta,\zeta} - E^{\text{scat}}_{\gamma,\eta,\zeta}(\chi) \right|\right|^2_{\mathcal{S}}}{\sum_{\eta=1}^{nRx} \sum_{\zeta=1}^{nTx} \left|\left| E^{\text{meas}}_{\gamma,\eta,\zeta} \right|\right|^2_{\mathcal{S}}}. \tag{B.1}$$

where $E^{\text{scat}}_{\gamma,\eta,\zeta}(\chi)$ is the simulated scattered field due to the predicted contrast χ, when the ζth transmitter is active and the data collection is performed at the ηth receiver at the γth frequency of operation. Also, $E^{\text{meas}}_{\gamma,\eta,\zeta}$ denotes the measured data collected under the same condition. Also, nTx denotes the number of transmitters using which the OI is irradiated, nRx is the number of receivers used to collect the scattering data when a transmitter is active, and nf denotes the number of frequencies used to irradiate the OI. The frequency weighting ξ_γ, which has shown promises to provide equal weight for different frequencies of operation, is given by [42]

$$\xi_\gamma = \frac{f_\gamma^{-2}}{\sum\limits_{\varsigma=1}^{nf} f_\varsigma^{-2}}. \tag{B.2}$$

C

Multiplicative Regularized Gauss-Newton Inversion

In this appendix, the multiplicative regularized Gauss-Newton inversion (MR-GNI) algorithm [42, 43] is briefly explained. The whole idea behind the MR-GNI algorithm revolves around the minimization of the data misfit cost functional shown in (B.1). The MR-GNI algorithm attempts to minimize this cost functional by applying Gauss-Newton minimization to this cost functional. This minimization is an iterative procedure. For example, at the nth iteration of the MR-GNI algorithm, the contrast χ is updated as $\chi_{n+1} = \chi_n + \beta_n \Delta\chi_n$ where χ_n is the reconstructed contrast at the previous iteration, $\Delta\chi_n$ is the correction that needs to be applied to χ_n to form the new predicted contrast χ_{n+1}. The parameter β_n is called the step length, and is effectively controls the weight of the correction $\Delta\chi_n$.

We now need to address the term "multiplicative regularized". It is well-known that the data misfit cost fucntional (B.1) is ill-posed. Therefore, if the Gauss-Newton minimization is directly applied to this cost functional, the minimization process will be instable. That is, the resulting minimum will be an oscillatory contrast. To avoid this instability, appropriate regularization techniques need to be applied to this cost functional prior to minimization [85]. One form of regularization is the multiplicative regularization. In this type of regularization, an appropriate term is multiplied to the data misfit cost functional. Denoting the data misfit cost functional by $\mathcal{C}^{LS}(\chi)$ and denoting the multiplicative regularization term by $\mathcal{C}^{MR}(\chi)$, the multiplicative regularized cost functional will then be $\mathcal{C}(\chi) = \mathcal{C}^{LS}(\chi) \times \mathcal{C}^{MR}(\chi)$. This multiplicative regularized cost functional will then be minimized by the Gauss-Newton method. Therefore, the name of this inversion algorithm is the multiplicative regularized Gauss-Newton inversion algorithm.

The above implementation of the MR-GNI algorithm is *blind* inversion. That is, this implementation is not based on the use of any *a priori* information. Unless otherwise stated, all the results presented in this thesis have been generated by this blind implementation. However, in one of the examples discussed in Section 4.1.1 of this thesis, we have also considered another form of the MR-GNI algorithm, which we refer to as the binary inversion. (See Figure 4.9 which has been obtained through the use of binary MR-GNI). The binary implementation of the MR-GNI algorithm is a shape and location reconstruction algorithm. In this type of inversion algorithm, the permittivity of the object of interest will be given as *a priori* information to the inversion algorithm through the use of an appropriate regularizer. The binary inversion algorithm will then try to find the spatial variation of this permittivity [48].

D

Radiation Mechanism

In this Appendix, the radiation mechanism of the covered monopole-like slot antenna element based on its current distribution will be presented. The geometrical parameters of this antenna are listed in Table 6.1.

Before starting our discussion, let's consider Figure D.1(a) and (b) in which the current distribution of the covered antenna at 4 GHz and 9 GHz have been shown. As can be seen in Figure D.1, the current distribution is mainly concentrated on the slot edge, fork-shaped feed, and of course the CPW line. As can be seen in Figure D.1(a) and (b), both y and z components of the current distribution exist over the feed and the ground. We also note that the z-component of the current distribution on the CPW line has the same magnitude but is out of phase with respect to the adjacent ground plane. This is also the case for the y-component of the current distribution on horizontal section of fork-shaped feed, and its symmetrical counterpart. Therefore, the far-field radiation due to these current distribution components will cancel the effect of each other. On the other hand, the radiation of the proposed antenna is mainly due to the z-component of the current distribution on the fork-shaped vertical stubs feed as well as the folded ground strips as they are in phase.

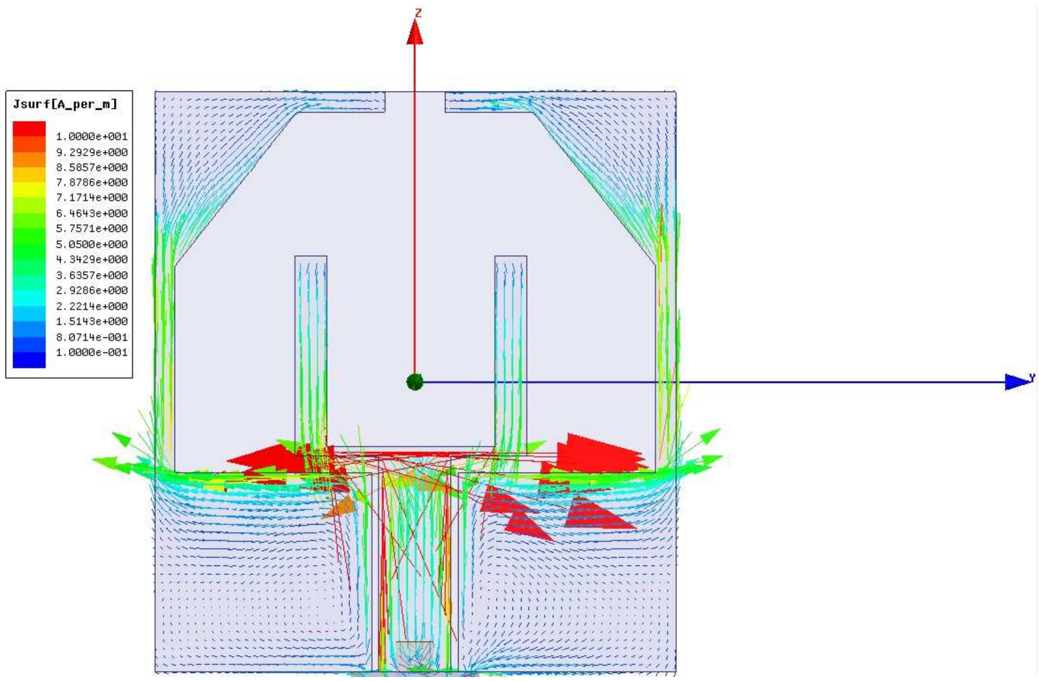

(a) 4 GHz

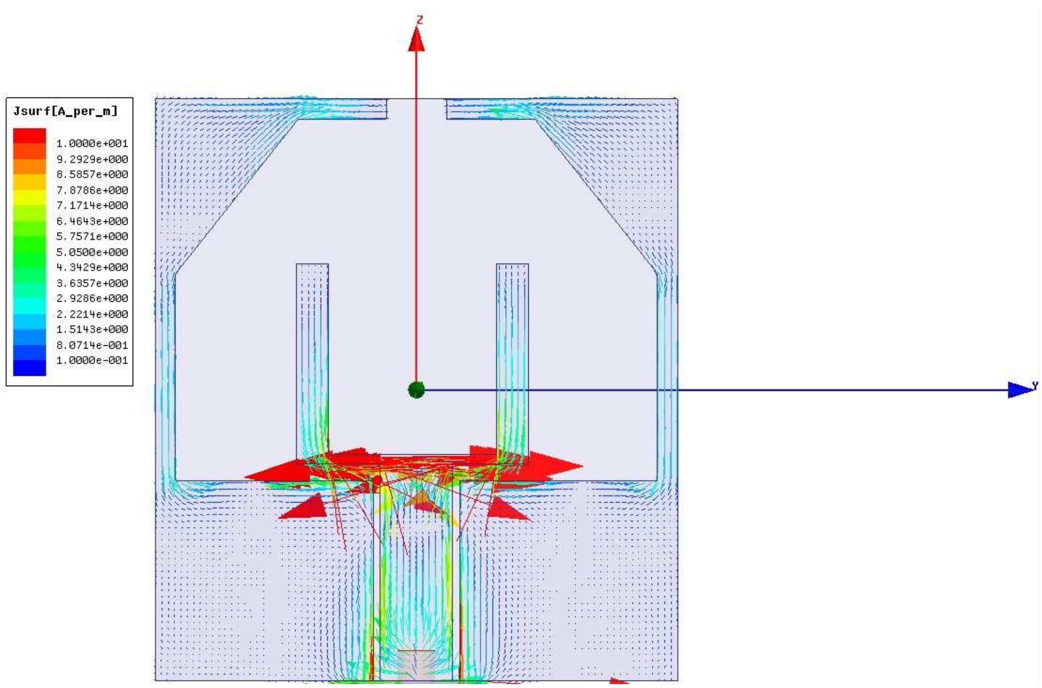

(b) 9 GHz

Fig. D.1: Current distribution of the covered monopole-like slot antenna with the dimensions listed in Table 6.1 at two different frequencies: (a) 4 GHz, and (b) 9 GHz.

Bibliography

[1] N. Bayat, P. Mojabi, and J. LoVetri, “Use of synthesized fields in microwave tomography inversion,” in *16th International Symposium on Antenna Technology and Applied Electromagnetics Conference*, July 2014, pp. 1–2.

[2] Y. M. M. Antar and D. Guha, *Microstrip and Printed Antennas: New Trends, Techniques and applications*. Hoboken, NJ, USA: John Wiley & Sons, 2010.

[3] X. Qing and Z. Chen, “Compact coplanar waveguide-fed ultra-wideband monopole-like slot antenna,” *Microwaves, Antennas Propagation, IET*, vol. 3, no. 5, pp. 889–898, 2009.

[4] A. Abubakar, P. M. van den Berg, and J. J. Mallorqui, “Imaging of biomedical data using a multiplicative regularized contrast source inversion method,” *IEEE Trans. Microwave Theory Tech.*, vol. 50, no. 7, pp. 1761–1777, July 2002.

[5] J. M. Sill and E. C. Fear, “Tissue sensing adaptive radar for breast cancer detection–experimental investigation of simple tumor models,” *IEEE Trans. Microwave Theory Tech.*, vol. 53, no. 11, pp. 3312–3319, November 2005.

[6] P. M. Meaney, M. W. Fanning, T. Raynolds, C. J. Fox., Q. Fang, C. A. Kogel, S. P. Poplack, and K. D. Paulsen, “Initial clinical experience with microwave breast imaging in women with normal mammography,” *Acad Radiol.*, March 2007.

[7] M. Pastorino, S. Caorsi, and A. Massa, “A global optimization technique for microwave nondestructive evaluation,” *IEEE. Trans. Instrum. and Meas.*, vol. 51, no. 4, pp. 666–673, Aug 2002.

[8] W. H. Weedon, W. C. Chew, and P. E. Mayes, “A step-frequency radar imaging system for microwave nondestructive evaluation,” *Progress in Electromagnetic Research*, vol. 28, pp. 121–146, 2000.

[9] L. P. Song, C. Yu, and Q. H. Liu, "Through-wall imaging (TWI) by radar: 2-D tomographic results and analyses," *IEEE Trans. Geosci. Remote Sensing*, vol. 43, no. 12, pp. 2793–2798, Dec 2005.

[10] S. Poplack, T. Tosteson, W. Wells, B. Pogue, P. Meaney, A. Hartov, C. Kogel, S. Soho, J. Gibson, and K. Paulsen, "Electromagnetic breast imaging results of a pilot study in women with abnormal mammograms," *Radiology*, vol. 243, no. 2, pp. 350–359, 2007.

[11] T. Rubæk, P. M. Meaney, P. Meincke, and K. D. Paulsen, "Nonlinear microwave imaging for breast-cancer screening using Gauss-Newton's method and the CGLS inversion algorithm," *IEEE Trans. Antennas Propag.*, vol. 55, no. 8, pp. 2320–2331, Aug 2007.

[12] E. C. Fear, X. Li, S. C. Hagness, and M. Stuchly, "Confocal microwave imaging for breast cancer detection: localization of tumors in three dimensions," *IEEE Trans. Biomed Eng.*, vol. 49, no. 8, pp. 812–822, Aug 2002.

[13] S. Y. Semenov, R. H. Svenson, V. G. Posukh, A. G. Nazarov, Y. E. Sizov, A. E. Bulyshev, A. E. Souvorov, W. Chen, J. Kasell, and G. P. Tastis, "Dielectrical spectroscopy of canine myocardium during acute ischemia and hypoxia at frequency spectrum from 100 KHz to 6 GHz," *IEEE Trans. Med. Imag*, vol. 21, no. 6, pp. 703–707, June 2002.

[14] S. Semenov, "Microwave tomography: review of the progress towards clinical applications," *Phil. Trans. R. Soc. A*, vol. 367, pp. 3021–3042, July 2009.

[15] P. M. Meaney, T. Zhou, M. W. Fanning, S. A. Geimer, and K. D. Paulsen, "Microwave imaging for bone fracture risk assessment," in *Proc. 2008 Applied Computational Electromagnetics Symp.*, Niagra Falls, Canada, March 31-April 4, pp. 462–466.

[16] S. Y. Semenov and D. R. Corfield, "Microwave tomography for brain imaging: Feasibility assessment for stroke detection," *International Journal of Antennas and Propagation*, 2008.

[17] P. Meaney, P. Kaufman, L. Muffly, M. Click, S. Poplack, W. Wells, G. Schwartz, R. M. di Florio-Alexander, T. Tosteson, Z. Li, S. Geimer, M. Fanning, T. Zhou, N. Epstein, and K. Paulsen, "Microwave imaging for neoadjuvant chemotherapy monitoring: initial clinical experience," *Breast Cancer Research*, vol. 15, no. 8, pp. 2320–2331, Aug 2013.

[18] N. Bayat and P. Mojabi, "The effect of antenna incident field distribution on microwave tomography reconstruction," *Progress In Electromagnetics Research*, vol. 145, pp. 153–161, 2014.

[19] J. D. Shea, P. Kosmas, S. C. Hagness, and B. D. V. Veen, "Three-dimensional microwave imaging of realistic numerical breast phantoms via a multiple-frequency inverse scattering technique," *Medical Physics*, vol. 37, no. 8, pp. 4210–4226, 2010.

[20] M. Ostadrahimi, P. Mojabi, S. Noghanian, J. LoVetri, and L. Shafai, “A multiprobe-per-collector modulated scatterer technique for microwave tomography,” *IEEE Antennas Wireless Propag. Lett.*, vol. 10, pp. 1445–1448, 2011.

[21] P. Mojabi and J. LoVetri, “A novel microwave tomography system using a rotatable conductive enclosure,” *IEEE Trans. Antennas Propag.*, vol. 59, no. 5, pp. 1597–1605, 2011.

[22] M. Ostadrahimi, P. Mojabi, C. Gilmore, A. Zakaria, S. Noghanian, S. Pistorius, and J. LoVetri, “Analysis of incident field modeling and incident/scattered field calibration techniques in microwave tomography,” *IEEE Antennas Wireless Propag. Lett.*, vol. 10, pp. 900–903, 2011.

[23] A. Abubakar, P. M. van den Berg, and S. Y. Semenov, “Two– and three– dimensional algorithms for microwave imaging and inverse scattering,” *J. Electrom. Waves. Applic.*, vol. 17, no. 2, pp. 209–231, 2003.

[24] T. M. Habashy and A. Abubakar, “A general framework for constraint minimization for the inversion of electromagnetic measurements,” *Progress in Electromagnetics Research*, vol. 46, pp. 265–312, 2004.

[25] P. Meaney, K. Paulsen, J. Chang, M. Fanning, and A. Hartov, “Nonactive antenna compensation for fixed-array microwave imaging. II. imaging results,” *IEEE Trans. Med. Imag.*, vol. 18, no. 6, pp. 508–518, 1999.

[26] C. Gilmore, A. Abubakar, W. Hu, T. Habashy, and P. van den Berg, “Microwave biomedical data inversion using the finite-difference contrast source inversion method,” *IEEE Trans. Antennas Propag.*, vol. 57, no. 5, pp. 1528–1538, 2009.

[27] V. Okhmatovski, J. Aronsson, and L. Shafai, “A well-conditioned non-iterative approach to solution of the inverse problem,” *IEEE Trans. Antennas Propag.*, vol. 60, no. 5, pp. 2418–2430, 2012.

[28] A. Abubakar and T. M. Habashy, “Nonlinear inversion of multi–frequency microwave Fresnel data using the multiplicative regularized contrast source inversion,” *Progress in Electromagnetics Research*, vol. 62, pp. 193–201, 2006.

[29] A. Abubakar, P. M. van den Berg, and T. M. Habashy, “Application of the multiplicative regularized contrast source inversion method on TM- and TE-polarized experimental Fresnel data,” *Inverse Probl.*, vol. 21, pp. S5–S13, 2005.

[30] A. E. Bulyshev, A. E. Souvorov, S. Y. Semenov, R. H. Svenson, A. G. Nazarov, Y. E. Sizov, and G. P. Tastis, “Three dimensional microwave tomography. theory and computer experiments in scalar approximation,” *Inverse Probl.*, vol. 16, pp. 863–875, 2000.

[31] A. E. Bulyshev, A. E. Souvorov, S. Y. Semenov, V. G. Posukh, and Y. E. Sizov, “Three dimensional vector microwave tomography: Theory and computational experiments,” *Inverse Probl.*, vol. 20, pp. 1239–1259, 2004.

[32] A. Abubakar and P. M. van den Berg, "Iterative forward and inverse algorithms based on domain integral equations for three–dimensional electric and magnetic objects," *J. Comput. Phys.*, vol. 195, pp. 236–262, 2004.

[33] P. C. Hansen, "Numerical tools for analysis and solution of Fredholm integral equations of the first kind," *Inverse Probl.*, vol. 8, pp. 849–872, 1992.

[34] T. K. Jensen, "Stabilization algorithms for large-scale problems," Ph.D. dissertation, Technical University of Denmark, Kongens Lyngby, Denmark, 2006.

[35] P. C. Hansen, *Rank-deficient and discrete ill-posed problems: Numerical aspects of linear inversion*. Philadelphia, PA: SIAM, 1998.

[36] C. Balanis, *Advanced Engineering Electromagnetics*. New York: John Wiley and Sons, 1989.

[37] T. J. Cui, W. C. Chew, X. X. Yin, and W. Hong, "Study of resolution and super resolution in electromagnetic imaging for half-space problems," *IEEE Trans. Antennas Propag.*, vol. 52, no. 6, pp. 1398–1411, June 2004.

[38] C. Gilmore, P. Mojabi, A. Zakaria, S. Pistorius, and J. LoVetri, "On super-resolution with an experimental microwave tomography system," *IEEE Antennas and Wireless Propagation Letters*, vol. 9, pp. 393–396, 2010.

[39] S. Semenov, R. Svenson, A. Bulyshev, A. Souvorov, A. Nazarov, Y. Sizov, V. Posukh, A. Pavlovsky, P. Repin, and G. Tatsis, "Spatial resolution of microwave tomography for detection of myocardial ischemia and infarction-experimental study on two-dimensional models," *IEEE Trans. Microwave Theory Tech.*, vol. 48, no. 4, pp. 538–544, Apr 2000.

[40] P. C. Hansen, M. E. Kilmer, and R. H. Kjeldsen, "Exploiting residual information in the parameter choice for discrete ill-posed problems," *BIT Numerical Mathematics*, vol. 46, pp. 41–59, 2006.

[41] A. Abubakar, P. M. van den Berg, T. M. Habashy, and H. Braunisch, "A multiplicative regularization approach for deblurring problems," *IEEE Trans. Image Processing*, vol. 13, no. 11, pp. 1524–1532, Nov 2004.

[42] A. Abubakar, T. M. Habashy, V. L. Druskin, L. Knizhnerman, and D. Alumbaugh, "2.5D forward and inverse modeling for interpreting low-frequency electromagnetic measurements," *Geophysics*, vol. 73, no. 4, pp. F165–F177, July–Aug 2008.

[43] P. Mojabi and J. LoVetri, "Microwave biomedical imaging using the multiplicative regularized Gauss–Newton inversion," *IEEE Antennas Wireless Propag. Lett.*, vol. 8, pp. 645–648, 2009.

[44] ——, “Enhancement of the Krylov subspace regularization for microwave biomedical imaging,” *IEEE Transactions on Medical Imaging*, vol. 28, no. 12, pp. 2015–2019, Dec 2009.

[45] P. C. Hansen, “The discrete Picard condition for discrete ill-posed problems,” *BIT*, vol. 30, pp. 658–672, 1990.

[46] A. Abubakar, P. M. van den Berg, and S. Y. Semenov, “A robust iterative method for Born inversion,” *IEEE Trans. Geosci. Remote Sensing*, vol. 42, no. 2, pp. 342–354, Feb 2004.

[47] F. Caramanica and G. Oliveri, “An innovative multi-source strategy for enhancing the reconstruction capabilities of inverse scattering techniques,” *Progress in Electromagnetics Research*, vol. 101, pp. 349–374, 2010.

[48] P. Mojabi, J. LoVetri, and L. Shafai, “A multiplicative regularized Gauss–Newton inversion for shape and location reconstruction,” *IEEE Transactions on Antennas and Propagation*, vol. 59, no. 12, pp. 4790–4802, 2011.

[49] J.-M. Geffrin, P. Sabouroux, and C. Eyraud, “Free space experimental scattering database continuation: experimental set-up and measurement precision,” *Inverse Probl.*, vol. 21, pp. S117–S130, 2005.

[50] A. Grbic, L. Jiang, and R. Merlin, “Near-field plates: subdiffraction focusing with patterned surfaces,” *Science*, vol. 320, pp. 511–513, April 2008.

[51] J. Bourqui, M. Campbell, T. Williams, and E. Fear, “Antenna evaluation for ultra-wideband microwave imaging,” *International Journal of Antennas and Propagation*, 2010.

[52] N. Bayat and P. Mojabi, “An antenna element with improved near-field focusing for multiple-frequency microwave tomography applications,” in *IEEE International Symposium on Antennas and Propagation*, Memphis, Tennessee, USA, July 2014.

[53] C. Gilmore, P. Mojabi, A. Zakaria, M. Ostadrahimi, C. Kaye, S. Noghanian, L. Shafai, S. Pistorius, and J. LoVetri, “A wideband microwave tomography system with a novel frequency selection procedure,” *IEEE Transactions on Biomedical Engineering*, vol. 57, no. 4, pp. 894–904, April 2010.

[54] N. Bayat and P. Mojabi, “On the effect of antenna illumination patterns on the accuracy and resolution of microwave tomography,” in *IEEE International Symposium on Antennas and Propagation*, July 2013.

[55] J. Bourqui, M. Okoniewski, and E. Fear, “Balanced antipodal vivaldi antenna with dielectric director for near-field microwave imaging,” *IEEE Transactions on Antennas and Propagation*, vol. 58, no. 7, pp. 2318–2326, July 2010.

[56] J. P. Stang, “A 3D active microwave imaging system for breast cancer screening,” Ph.D. dissertation, Duke University, Durham, United States, 2008.

[57] M. Al-Joumayly, S. Aguilar, N. Behdad, and S. Hagness, “Dual-band miniaturized patch antennas for microwave breast imaging,” *IEEE Antennas and Wireless Propagation Letters,*, vol. 9, pp. 268–271, 2010.

[58] S. Adnan, R. Abd-Alhameed, H. Hraga, I. T. E. Elfergani, and M. Child, “Compact microstrip antenna design for microwave imaging,” in *Loughborough Antennas and Propagation Conference*, Nov 2010, pp. 389–392.

[59] R. Nilavalan, I. Craddock, A. Preece, J. Leendertz, and R. Benjamin, “Wideband microstrip patch antenna design for breast cancer tumour detection,” *Microwaves, Antennas Propagation, IET*, vol. 1, no. 2, pp. 277–281, April 2007.

[60] S. S. Tiang, M. Ain, and M. Abdullah, “Compact and wideband wide-slot antenna for microwave imaging system,” in *IEEE International RF and Microwave Conference (RFM)*, Dec 2011, pp. 63–66.

[61] D. Gibbins, M. Klemm, I. Craddock, J. Leendertz, A. Preece, and R. Benjamin, “A comparison of a wide-slot and a stacked patch antenna for the purpose of breast cancer detection,” *IEEE Transactions on Antennas and Propagation*, vol. 58, no. 3, pp. 665–674, March 2010.

[62] M. Ostadrahimi, S. Noghanian, L. Shafai, and A. Foroozesh, “Comparing performance of double layer stripline fed and single layer y2y fed vivaldi antennas,” in *14th International Symposium onAntenna Technology and Applied Electromagnetics and the American Electromagnetics Conference (ANTEM-AMEREM)*, July 2010, pp. 1–4.

[63] S. Salvador and G. Vecchi, “On some experiments with UWB microwave imaging for breast cancer detection,” in *IEEE International Symposium Antennas and Propagation Society*, June 2007, pp. 253–256.

[64] X. Chen, J. Liang, S. Wang, Z. Wang, and C. Parini, “Small ultra wideband antennas for medical imaging,” in *Loughborough Antennas and Propagation Conference*, March 2008, pp. 28–31.

[65] W. C. Khor, M. E. Bialkowski, A. Abbosh, N. Seman, and S. Crozier, “An ultra wideband microwave imaging system for breast cancer detection,” *IEICE Trans. Commun*, vol. E90-B, no. 9, pp. 2376–2381, 2007.

[66] B. Mohammed, A. Abbosh, and M. Bialkowski, “Design of tapered slot antenna operating in coupling liquid for ultrawideband microwave imaging systems,” in *IEEE International Symposium on Antennas and Propagation*, July 2011, pp. 145–148.

[67] M. Bialkowski, A. Abbosh, Y. Wang, D. Ireland, A. Bakar, and B. J. Mohammed, “Microwave imaging systems employing cylindrical, hemispherical and planar arrays

of ultrawideband antennas," in *Asia-Pacific Microwave Conference Proceedings*, Dec 2011, pp. 191–194.

[68] A. Abbosh, "Compact antenna for microwave imaging systems," in *Cairo International Biomedical Engineering Conference*, Dec 2008, pp. 1–4.

[69] Y. Wang, A. Fathy, and M. Mahfouz, "Novel compact tapered microstrip slot antenna for microwave breast imaging," in *IEEE International Symposium on Antennas and Propagation*, July 2011, pp. 2119–2122.

[70] Y. Wang, A. Bakar, and M. Bialkowski, "Compact tapered slot antennas for UWB microwave imaging applications," in *18th International Conference on Microwave Radar and Wireless Communications*, June 2010, pp. 1–4.

[71] C. J. Fox, P. M. Meaney, F. Shubitidze, L. Potwin, and K. D. Paulsen, "Characterization of an implicitly resistively-loaded monopole antenna in lossy liquidmedia," *International Journal of Antennas and Propagation*, pp. 1–9, 2008.

[72] T. Rubæk and V. Zhurbenko, "Prototype of microwave imaging system for breast-cancer screening," in *Proc. 13th International Symposium on Antenna Technology and Applied Electromagnetics and the Canadian Radio Science Meeting (ANTEM/URSI)*, Banff, Canada, Feb. 2009.

[73] I. Hossain, S. Noghanian, and S. Pistorius, "A diamond shaped small planar ultra wide band (UWB) antenna for microwave imaging purpose," in *IEEE International Symposium Antennas and Propagation Society*, June 2007, pp. 5713–5716.

[74] S. Semenov, A. Bulyshev, A. Abubakar, V. Posukh, Y. Sizov, A. Souvorov, P. van den Berg, and T. Williams, "Microwave-tomographic imaging of the high dielectric-contrast objects using different image-reconstruction approaches," *IEEE Transactions on Microwave Theory and Techniques*, vol. 53, no. 7, pp. 2284–2294, July 2005.

[75] X. Li, S. Hagness, M. Choi, and D. van der Weide, "Numerical and experimental investigation of an ultrawideband ridged pyramidal horn antenna with curved launching plane for pulse radiation," *IEEE Antennas and Wireless Propagation Letters*, vol. 2, no. 1, pp. 259–262, 2003.

[76] D. Hailu and S. Safavi-Naeini, "Narrow focus ultra-wideband antenna for breast cancer detection," in *IEEE Radio and Wireless Symposium*, Jan 2009, pp. 437–440.

[77] S. M. Shum, K. F. Tong, X. Zhang, and K. M. Luk, "FDTD modeling of microstrip-line-fed wide-slot antenna," *Microwave and Optical technology letters*, vol. 10, pp. 118–120, October 1995.

[78] M. K. Kim, K. Kim, Y. H. Suh, and I. Park, "A T-shaped microstrip-line-fed wide slot antenna," in *IEEE Antennas and Propagation Society International Symposium*, vol. 3, July 2000, pp. 1500–1503 vol.3.

[79] W. H. Lijing, Z. Shengwei, L. Heguang, and J. Jingshan, "Broadband double cross-shaped microstrip-fed slot antenna," in *IEEE International Symposium on Microwave, Antenna, Propagation and EMC Technologies for Wireless Communications*, vol. 1, Aug 2005, pp. 119–122 Vol. 1.

[80] J.-Y. Sze and K.-L. Wong, "Bandwidth enhancement of a microstrip-line-fed printed wide-slot antenna," *IEEE Transactions on Antennas and Propagation*, vol. 49, no. 7, pp. 1020–1024, 2001.

[81] S. Sharma, L. Shafai, and N. Jacob, "Investigation of wide-band microstrip slot antenna," *IEEE Transactions on Antennas and Propagation*, vol. 52, no. 3, pp. 865–872, 2004.

[82] S. Latif, L. Shafai, and S. Sharma, "Bandwidth enhancement and size reduction of microstrip slot antennas," *IEEE Transactions on Antennas and Propagation*, vol. 53, no. 3, pp. 994–1003, March 2005.

[83] X. Qing and Z. N. Chen, "A miniaturized directional UWB antenna," in *IEEE International Symposium on Antennas and Propagation*, 2011, pp. 1470–1473.

[84] S. Semenov, J. Kellam, T. Williams, M. Quinn, and B. Nair, "2D microwave tomographic system for extremities imaging: Initial performance assessment in animal trial," in *Proceedings of the Fourth European Conference on Antennas and Propagation*, 2010, pp. 1–2.

[85] P. Mojabi and J. LoVetri, "Overview and classification of some regularization techniques for the Gauss-Newton inversion method applied to inverse scattering problems," *IEEE Transactions on Antennas and Propagation*, vol. 57, no. 9, pp. 2658–2665, Sept 2009.